Electric and magnetic characteristics of equatorial plasma depletions

An observational assessment using the *Swarm* mission

Juan Rodríguez Zuluaga

Mathematisch-Naturwissenschaftlichen Fakultät
Institut für Geowissenschaften
der Universität Potsdam

Publikationsbasierte Dissertation
zur Erlangung des akademischen Grades
"doctor rerum naturalium"
(Dr. rer. nat.)
in der Wissenschaftsdisziplin
"Geophysik"

11. Februar 2020

Betreuer:
Prof. Dr. Claudia Stolle
Prof. Dr. Jorge L. Chau

Gutachter:
Dr. Astrid Maute
Dr. Robert Pfaff
Prof. Dr. Jens Tronicke
Prof. Dr. Philipp Richter
Prof. Dr. Carsten Denker
Prof. Dr. Frank Kruger
Prof. Dr. Gert Zoller

Published online at the
Institutional Repository of the University of Potsdam:
https://doi.org/10.25932/publishup-44587
https://nbn-resolving.org/urn:nbn:de:kobv:517-opus4-445873

Declaration

I hereby declare that except where specific reference is made to the work of others, the contents of this dissertation are original and have not been submitted in whole or in part for consideration for any other degree or qualification in this, or any other university. This dissertation is my own work and contains nothing which is the outcome of work done in collaboration with others, except as specified in the text.

Juan Rodríguez Zuluaga
11. Februar 2020

Acknowledgements

The desire to comprehend how things work is a need for many, a lifestyle. Understanding the nature, either by guessing and imagining what is going on and validating it with observations or by measuring and then analyzing, is supported by people sometimes with contrasting lifestyles. Good scientific policies, funding programs, supportive governments, and institutions are the result of opened and selfless minds that work together to make science possible. That said, I want to start by thanking everyone at the *Deutsche Forschungsgemeinschaft* for funding this investigation through the Special priority program *DynamicEarth*. I also want to thank the *European Space Agency* and all the minds behind the *Swarm* mission for making possible one of the most exceptional satellite missions by the date of this dissertation. Their effort is reflected in the outstanding scientific achievements that have allowed a better understanding of the Earth's magnetic field and its near space.

Now I can say that, indeed, the time as a doctoral student has been the most amusing period throughout my academic life; I felt free. During this time, I realized how relevant it is to structure our thoughts to share them with others and advance knowledge. I also realized that supportiveness is the most valuable skill of a supervisor. For that, I will always be overly grateful to Prof. Claudia Stolle. She allowed me and my stubbornness to be side by side along this period, still heading me towards a more structural way to address research. I am also deeply indebted to Prof. Hermann Lühr. He showed me that passion and love for science is an everlasting fuel for life. I also want to thank Dr. Yosuke Yamazaki for encouraging and valuable discussions. Much gratitude is owed to Prof. Jorge Chau, Dr. Jaeheung Park, and Prof. Ludger Scherliess for the constructive conversations, exchange of ideas, and for helping me indirectly to keep everything in perspective.

This dissertation is somehow the result of almost ten years of understanding myself in science, luckily, along with fascinating people. I am profoundly grateful to Dr. Héctor Mora-Páez for sharing his view of science back in Colombia when I was in the GeoRED project at the *Colombian Geological Survey* (INGEOMINAS at that time). His support for almost five years, starting in 2009 helped me to understand that passion and discipline is the

best combination ever. I am also very much grateful to Prof. Sandro Radicella and Dr. Bruno Nava at the ICTP in Italy for being my first mentors in the ionospheric research. The support and freedom they gave me to explore topics of my interest have been immensely valuable. I also thank Prof. Christine Amory-Mazaudier, Prof. Luigi Ciraolo, and Prof. Fred Kucharski for their backing during my research stage at ICTP.

As mentioned above, the last ten years have been full of different experiences in different places. So I have been extremely fortunate to have come across lovely people with whom I have unforgettable moments, so important that they became my friends. I want to start by thanking Foteini for being there at the right time. I also want to thank Katy, Izarra, Anton, Maria Isabel, Robin, and Angelica, for sharing more than a beer. The much-needed leisure has also been shared with Sergio, Tarique, Leoni, Achim, Irina, Nikita, and Yenca. I want to thank all my colleagues in section 2.3 at the GFZ for their help during these years. Also, all the GeoRED group in Colombia who have been witnesses of my process and with whom I shared the first five years of this adventure. Lastly, I would like to deeply thank Alejo for proofreading and helping me to structure this dissertation and Vanessa for designing the fantastic cover.

Abstract

Near-Earth space represents a significant scientific and technological challenge. Particularly at magnetic low-latitudes, the horizontal magnetic field geometry at the dip equator and its closed field-lines support the existence of a distinct electric current system, abrupt electric field variations and the development of plasma irregularities. Of particular interest are small-scale irregularities associated with *equatorial plasma depletions* (EPDs). They are responsible for the disruption of trans-ionospheric radio waves used for navigation, communication, and Earth observation. The fast increase of satellite missions makes it imperative to study the near-Earth space, especially the phenomena known to harm space technology or disrupt their signals. EPDs correspond to the large-scale structure (i.e., tens to hundreds of kilometers) of topside *F* region irregularities commonly known as Spread *F*. They are observed as depleted-plasma density channels aligned with the ambient magnetic field in the post-sunset low-latitude ionosphere. Although the climatological variability of their occurrence in terms of season, longitude, local time and solar flux is well-known, their day to day variability is not. The sparse observations from ground-based instruments like radars and the few simultaneous measurements of ionospheric parameters by space-based instruments have left gaps in the knowledge of EPDs essential to comprehend their variability.

In this dissertation, I profited from the unique observations of the ESA's Swarm constellation mission launched in November 2013 to tackle three issues that revealed novel and significant results on the current knowledge of EPDs. I used Swarm's measurements of the electron density, magnetic, and electric fields to answer, (1.) what is the direction of propagation of the electromagnetic energy associated with EPDs?, (2.) what are the spatial and temporal characteristics of the electric currents (field-aligned and diamagnetic currents) related to EPDs, i.e., seasonal/geographical, and local time dependencies?, and (3.) under what conditions does the balance between magnetic and plasma pressure across EPDs occur?

The results indicate that: (1.) The electromagnetic energy associated with EPDs presents a preference for interhemispheric flows; that is, the related Poynting flux directs from one magnetic hemisphere to the other and varies with longitude and season. (2.) The

field-aligned currents at the edges of EPDs are interhemispheric. They generally close in the hemisphere with the highest Pedersen conductance. Such hemispherical preference presents a seasonal/longitudinal dependence. The diamagnetic currents increase or decrease the magnetic pressure inside EPDs. These two effects rely on variations of the plasma temperature inside the EPDs that depend on longitude and local time. (3.) EPDs present lower or higher plasma pressure than the ambient. For low-pressure EPDs the plasma pressure gradients are mostly dominated by variations of the plasma density so that variations of the temperature are negligible. High-pressure EPDs suggest significant temperature variations with magnitudes of approximately twice the ambient. Since their occurrence is more frequent in the vicinity of the South Atlantic magnetic anomaly, such high temperatures are suggested to be due to particle precipitation.

In a broader context, this dissertation shows how dedicated satellite missions with high-resolution capabilities improve the specification of the low-latitude ionospheric electrodynamics and expand knowledge on EPDs which is valuable for current and future communication, navigation, and Earth-observing missions. The contributions of this investigation represent several 'firsts' in the study of EPDs: (1.) The first observational evidence of interhemispheric electromagnetic energy flux and field-aligned currents. (2.) The first spatial and temporal characterization of EPDs based on their associated field-aligned and diamagnetic currents. (3.) The first evidence of high plasma pressure in regions of depleted plasma density in the ionosphere. These findings provide new insights that promise to advance our current knowledge of not only EPDs but the low-latitude post-sunset ionosphere environment.

Zusammenfassung

Der erdnahe Weltraum stellt eine bedeutende wissenschaftliche und technologische Herausforderung dar. Insbesondere in niedrigeren magnetischen Breitengraden unterstützen die horizontale Geometrie des Magnetfelds und seine geschlossenen Feldlinien das Vorhandensein eines speziellen elektrischen Stromsystems, abrupte Änderungen der elektrischen Felder und das Auftreten von Plasmairregularitäten. Von besonderem Interesse sind regionale Unregelmäßigkeiten im Zusammenhang mit *äquatorialen Plasma-Verarmungen* (EPDs, Abkürzung aus dem Englischen für „*equatorial plasma depletions*"). Sie stören trans-ionosphärischer Funkwellen, welche zur Positionierung, Kommunikation und Erdbeobachtung eingesetzt werden. Die schnelle Entwicklung von Satellitenmissionen macht das Verständnis der erdnahen Weltraumphänomene zu einer Priorität, insbesondere derjenigen, welche die Weltraumtechnologie schädigen oder ihre Signale stören können. Die EPDs und die damit verbundenen Plasmairregularitäten sind seit Beginn des Weltraumzeitalters eines der am häufigsten untersuchten Phänomene. EPDs sind großflächigen Strukturen (d. h. zehn bis hundert Kilometer), die auf Spread *F* Ereignisse zurückgeführt werden können. Sie äußern sich als mit dem Hintergrund-Magnetfeld ausgerichtete Kanäle verarmter Plasmadichte, welche in niedrigen Breiten in der Ionophäre nach Sonnenuntergang auftreten. Obwohl die klimatologische Variabilität des Auftretens von EPDs bezüglich der Jahreszeit, geografischen Länge, Ortszeit und des Sonnenzyklus wohl bekannt sind, trifft dies nicht für ihre Tag-zu-Tag-Variabilität zu. Die spärlichen Beobachtungen von bodengestützten Instrumenten, wie Radargeräten, und die wenigen gleichzeitigen Messungen ionosphärischer Parameter von weltraumgestützten Instrumenten auf erdnahen Umlaufbahnen haben Wissenslücken hinterlassen, die für das Verständnis der Variabilität von EPDs essentiell sind.

In dieser Dissertation habe ich von einzigartigen Beobachtungen der im November 2013 gestarteten ESA Satellitenkonstellationsmission „Swarm" profitiert, um drei Probleme zu bearbeiten, die neue und signifikante Ergebnisse zum aktuellen Wissen über EPDs enthüllten. Ich habe Swarms Messungen der Elektronendichte, des magnetischen und des elektrischen Feldes verwendet, um Folgendes zu beantworten: (1.) In welche Richtung breitet sich die mit den EPDs verbundene elektromagnetische Energie aus? (2.) Was sind die räumlichen und

zeitlichen Eigenschaften der elektrischen Ströme (feldgerichtete und diamagnetische Ströme) in Bezug auf EPDs, d. h. wie hängen sie von der geografischen Länge, Jahreszeit und Lokalzeit ab? (3.) Unter welchen Bedingungen findet der mit EPDs verbundene Ausgleich zwischen magnetischem Druck und Plasmadruck statt?

Die Ergebnisse zeigen, dass: (1.) Die mit EPDs verbundene elektromagnetische Energie bevorzugt interhemisphärische Strömungen, das heißt, der zugehörige Poynting-Fluss strömt von einer magnetischen Hemisphäre zur anderen und die Strömungsrichtung variiert mit geografischer Länge und Jahreszeit. (2.) Die feldgerichteten Ströme an den Rändern von EPDs sind interhemisphärisch. Im Allgemeinen schließen sie sich in der Hemisphäre mit der höchsten Pedersen-Leitfähigkeit. Die derartige hemisphärische Präferenz zeigt eine Abhängigkeit bezüglich der Jahreszeit/geografischen Länge. Die diamagnetischen Ströme erhöhen oder verringern den magnetischen Druck innerhalb der EPDs. Diese beiden Effekte beruhen auf Variationen der Plasmatemperatur innerhalb der EPDs, die von der geografischen Länge und der Lokalzeit abhängt. (3.) EPDs weisen einen höheren oder niedrigeren Plasmadruck als ihre Umgebung auf. In Niederdruck-EPDs werden die Plasmadruckgradienten meist durch Variationen der Plasmadichte hervorgerufen, sodass Temperaturschwankungen vernachlässigbar sind. Hochdruck-EPDs deuten auf hohe innere Temperaturen hin, etwa das Zweifache der Umgebungstemperatur. Aufgrund ihres häufigeren Auftretens in der Nähe der Südatlantischen Magnetfeldanomalie wird vermutet, dass solche hohen Temperaturen auf den Einfall hochenergetischer Teilchen zurückzuführen sind.

In einem breiteren Kontext zeigt diese Dissertation auf, wie spezielle Satellitenmissionen mit hohem Auflösungsvermögen die Spezifikation der ionoshärischen Elektrodynamik in niedrigen Breiten und das Verständnis von EPDs verbessern, was wertvoll für aktuelle und zukünfte Kommunikatoins-, Positionierungs- sowie Erdbeobachtungsmissionen ist. Die Beiträge dieser Arbeit stellen gleich mehrere "Premieren" in der EPD-Forschung dar: (1.) Der erste empirische Nachweis interhemisphärischer elektromagnetischer Energieflüsse und feldgerichteter Ströme. (2.) Die erste raum-zeitliche Beschreibung von EPDs auf der Grundlage ihrer assoziierten feldgerichteten und diamagnetischen Ströme. (3.) Der erste Nachweis hohen Plasmadrucks in Regionen verminderter Plasmadichte in der Ionosphäre. Diese Forschungsergebnisse liefern neue Erkenntnisse, die nicht nur unser derzeitiges Wissen über EPDs, sondern auch jenes über die ionosphärische Domaine in niedrigen Breiten nach Sonnenuntergang fördert.

Table of contents

List of figures

Chapter 1

Introduction

1.1 Motivation

In the mid-1920s, experiments using vertical radio sounding confirmed the existence of an ionized layer in the atmosphere (Appleton, 1932), later named "ionosphere." By varying the frequency of the emitted radio waves two regions were detected at different altitudes, termed as *E* and *F* region. In the latter, which presents the highest altitude, Booker and Wells (1938) found a scattering of radio waves observed as diffuse echoes recorded by an ionosonde in Huancayo, Peru. The observations revealed a spread over a range of altitudes interpreted as due to scattering by fluctuations in electron density. Since then, this phenomenon has been called equatorial Spread *F* (ESF) and is known to cover a wide range of plasma irregularities typical of the post-sunset low-latitude ionosphere. Despite its discovery in the late 1930s, it was not until the beginning of the space race in 1957 that the study of ESF started to strengthen. In preparation for putting satellites in orbit by the International Geophysical Year (1957-1958), one question arose; how to track them optically? Answering this question was necessary also to obtain data from the Earth's upper atmosphere and gravitational field key to improve the accuracy of long-range missiles (Neufeld, 2018). As a result, the first U.S. satellite tracking network *Minitrack* became operational in October 1957, simultaneous to the launch of *Sputnik 1* by the Soviet Union. *Minitrack* consisted of a network of satellite tracking and receiving stations built along the 75° W meridian. Among the stations, the one located in Ancon near Lima, Peru presented its East-West Fine channel entirely noisy, particularly during nighttime (Woodman, 2009). By comparing these noisy signals with observations of ESF at Huancayo (about 200 km south-east of Ancon), Woodman (1960) showed a direct relationship between these two, and with it, the first use of satellite scintillation to study ESF. In subsequent years, different techniques and instruments were used to study this

phenomenon, like scattering of VHF signals (e.g., Cohen and Bowles, 1963), top sounding satellites (e.g., Calvert and Schmid, 1964), in situ satellite measurements (e.g., Hanson and Sanatani, 1971), transequatorial HF propagation (e.g., Röttger, 1973), rockets and VHF radars (e.g., Morse et al., 1977; Rastogi, 1978), among others. The increase of techniques and studies coincided with the rise in the number of satellites intended for communication and navigation purposes. Since ESF represents a problem for any trans-ionospheric radio wave propagation, understanding its nature to mitigate its effect on satellite signals has become ever more important to the date of this dissertation, eighty years after its discovery by Booker and Wells (1938).

The idea behind this dissertation is part of a plan that stands on a significant effort to measure the electric current system of the ionosphere, especially the one at nighttime low-latitudes. The story begins with the launch of the German *Challenging Minisatellite Payload* (CHAMP) on July 15, 2000. The *Deutsches Zentrum für Luft- und Raumfahrt* (DLR) and the *Deutsches GeoForschungsZentrum* (GFZ) initiated the satellite mission back in 1994 (Reigber et al., 1999) to study the Earth's gravitational and magnetic potential. Although spacecraft magnetometers date from 1958, Lühr et al. (2002) reported the first observational evidence of magnetic fluctuations related to electric currents in the nighttime *F* region using CHAMP data. Among their results, the authors found that some of the magnetic fluctuations were associated with the large-scale structure of ESF, generally referred to as *equatorial plasma depletions* (EPD). Satellite missions like *Dynamics Explorer* have also detected magnetic field fluctuations associated with EPDs (Aggson et al., 1992a). However, systematic studies of electric currents and electromagnetic characteristics of EPDs like the ones reported by Stolle et al. (2006), Park et al. (2009) and Lühr et al. (2014) were only possible due to the continuous long-term magnetic measurements of CHAMP. Even so, the lack of simultaneous high-resolution measurements of different ionospheric parameters such as electric fields and plasma density by a single spacecraft has left essential questions unsolved related to the electromagnetic energy flux, electric current system and pressure balance associated with EPDs. These aspects are of vital importance to comprehend the ionospheric environment where EPDs are embedded and the evolution of the EPDs themselves.

Successfully, on November 22, 2013, the *European Space Agency* (ESA) launched the *Swarm* constellation mission to measure the Earth's magnetic field with the highest precision ever. So far, the mission has unveiled different processes within the Earth's core responsible for the magnetic field's generation (e.g., Aubert and Finlay, 2019; Livermore et al., 2017). It has also helped to understand better the oceanic magnetic signals (e.g., Sabaka

et al., 2016; Saynisch et al., 2016) and those of lithospheric origin (e.g., Thébault et al., 2016). In addition to magnetic measurements, the three *Swarm* spacecraft carry payloads to simultaneously measure electron density, plasma temperature, and ion drift velocities. The use of these parameters has allowed advancing the knowledge of electric currents at high-latitudes (e.g., Laundal et al., 2016; Lühr et al., 2015b; McGranaghan et al., 2017), and mid- and low-latitudes (e.g., Alken et al., 2017; Iyemori et al., 2015; Lühr et al., 2015a; Yamazaki et al., 2018), polar patches (e.g., Chartier et al., 2018; Goodwin et al., 2015), medium-scale traveling ionospheric disturbances (e.g., Kil and Paxton, 2017; Park et al., 2016), Alfvén and ion cyclotron waves (e.g., Kim et al., 2018; Pakhotin et al., 2018), among other ionospheric phenomena. Regarding EPDs, *Swarm* has contributed in the study of their occurrence rate and morphology (e.g., Wan et al., 2018; Xiong et al., 2018), as well as their relation with the loss of GPS signals at LEO altitudes (e.g., Buchert et al., 2015; Xiong et al., 2016a). Systematic investigations on the electrodynamics of EPDs by using different simultaneous measurements had not been carried out until this dissertation.

1.2 Aims and objectives

It is evident from this brief historical view, that the number of studies involving electric and magnetic characteristics of EPDs is scarce, especially the ones related to their electric current system which can only be studied using spacecraft magnetometers at low-Earth orbits (LEO). In this regard, and owing to the adverse effect that EPDs generate on navigation, communication, and Earth-observing satellite missions, it is of great importance to advance in the understanding of EPDs by providing observational evidence of physical processes relevant for their modeling and subsequent forecasting.

This dissertation aims to increase knowledge of the electrodynamics of EPDs by focusing on three specific aspects: the electric current system, the electromagnetic energy flux, and the balance of pressures. All three represent relevant issues to address, which to date are mostly studied by numerical simulations and have not been assessed systematically by observations. In this work, I exploited the simultaneous high-resolution measurements of the magnetic field, electron density, and electric field gathered by the ESA's *Swarm* constellation mission to address the following questions:

1. What is the direction of propagation of the electromagnetic energy associated with EPDs? (Chapter 4)

2. What are the variations in space and time of the electric currents related to EPDs, i.e., geographical, seasonal, and local time dependencies? (Chapters 4, 5 and 6)

3. Under what conditions does the balance between magnetic and plasma pressure across EPDs occur? (Chapter 6)

1.3 Scientific contribution

In this dissertation, I use in situ measurements from LEO satellites to advance the current understanding of the near-Earth space. In a broader context, I show how dedicated satellite missions with high-resolution capabilities improve the specification of the low-latitude ionospheric electrodynamics and expand knowledge on specific phenomena important for future communication, navigation, and Earth-observing missions.

The primary contributions of this study correspond to a set of several 'firsts' in the study of EPDs, which are the consequence of the unique measurements of the *Swarm* mission:

1. The first observational evidence of interhemispheric electromagnetic energy flux and field-aligned currents (Rodríguez-Zuluaga et al., 2017).

2. The first spatial and temporal characterization of EPDs based on their associated field-aligned currents and diamagnetic currents (Rodríguez-Zuluaga and Stolle, 2019; Rodríguez-Zuluaga et al., 2019).

3. The first evidence of high plasma pressure in regions of depleted plasma density in the ionosphere (Rodríguez-Zuluaga et al., 2019).

These contributions are essential to understand the low-latitude ionospheric environment and the evolution of EPDs. The Poynting flux gives information about the location of the primary perturbation and the region where energy dissipates. It also tells us about the distribution of the plasma density and conductivity in the ambient plasma where the EPDs are embedded. The analysis of interhemispheric field-aligned currents at EPDs is valuable for modeling improvement; current models mostly use an equipotential field line approach. The characteristics of the EPDs-related currents are essential to understanding the spatial and temporal dependences of parameters relevant to the evolution of EPDs, such as conductivity,

plasma density, neutral winds, and ambient magnetic field. The pressure balance across EPDs gives us the macroscopic dynamics of the phenomenon by shedding light on how its evolution gets affected by factors such as the geometry of the ambient magnetic field, heating mechanisms, and density inhomogeneities.

In general, these contributions represent essential information for numerical simulations which lead to better forecasting of the phenomenon and future mitigation of the EPDs effects on radio wave propagation.

1.4 Organization

In Chapter 2, I introduce EPDs by briefly describing the low-latitude ionosphere, the plasma instabilities associated with their formation and the theoretical and observational evidence of their related electric currents and electromagnetic energy. It is worth to mention that since this dissertation is based on peer-reviewed papers (i.e., Chapters 4,5 and 6 are exact reproductions of published papers), Chapter 2 serves as a prelude to the individual introductions of the corresponding chapters. Chapter 3 presents a compressed description of the *Swarm* constellation mission focusing on the evolution of the orbits since its launch (i.e., altitude and local time) and the measurements used in this dissertation (i.e., magnetic field, electron density, and ion drifts). Chapter 4 provides the findings regarding the orientation of the electromagnetic energy flux associated with EPDs by computing the Poynting flux parallel to the ambient magnetic field from measurements of the magnetic and electric fields. Chapter 5 presents the spatial and temporal characteristics of field-aligned currents at the edges of EPDs (i.e., seasonal, longitudinal, and magnetic local time dependence). Chapter 6 presents the evaluation of the balance between magnetic and plasma pressure using magnetic fluctuations related to diamagnetic currents at the edges of EPDs. The results conclude whether the assumption of an isothermal process in the balance of pressure is valid. Finally, Chapter 7 summarizes the critical findings of this work and makes recommendations for future studies.

Chapter 2

The low-latitude ionosphere

In this chapter, I intend to offer a brief overview of the *equatorial plasma depletions* by describing the atmospheric region where they develop, their formation mechanisms and electrostatic characteristics. The aim is not to comprise every element of the theory and experiments, but to provide the necessary background to comprehend the results of this dissertation. Thorough reviews of the phenomenon can be found in the literature, e.g., Fejer and Kelley (1980); Hysell (2000); Kelley and Hysell (1991); Kelley et al. (2011); Ossakow (1981); Woodman (2009).

2.1 Primary characteristics

The ionosphere is the part of the Earth's upper atmosphere constituted by partially ionized plasma. It is to first-order horizontally stratified and extends from about 60 km to 1500 km altitude. Within that range, the plasma corresponds to approximately 0.00001% of the total atmosphere. It is created by photoionization of the neutral atmosphere via impinging *extreme ultraviolet* (EUV) solar radiation, and by impact ionization of the neutral atmosphere via energetic particle precipitation. The former mechanism of ionization is responsible for the creation of the primary part of the ionosphere, particularly at mid and low latitudes. Figures 2.1 and 2.2 show typical altitudinal profiles of the electron density and major ionospheric species for daytime and nighttime, respectively, as obtained from the *International Reference Ionosphere* (IRI) model (Bilitza et al., 2017). The altitude range above 150 km is termed the F region, sometimes subdivided into two layers during the daytime, F_1 and F_2. The main source of ionization at this altitude is the interaction of EUV radiation (10-100 nm) with atomic oxygen (O) and molecular nitrogen (N_2). The maximum plasma density in the ionosphere, usually referred to as the F peak, consists mostly of atomic oxygen ions

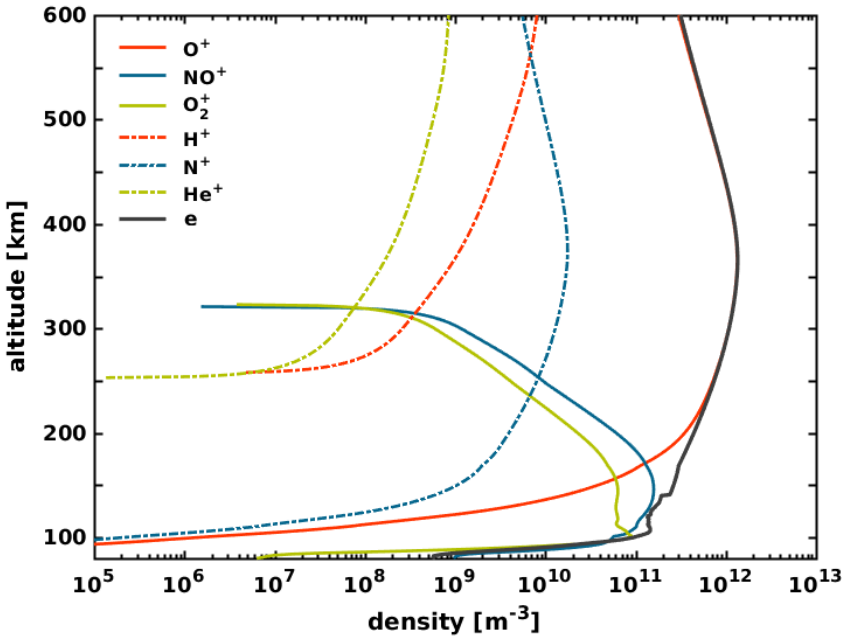

Fig. 2.1 Altitudinal profiles of densities of major species during daytime (12 LT) on March equinox at the dip equator and solar index F10.7=82 sfu. The horizontal axis is in logarithmic scale for visualization.

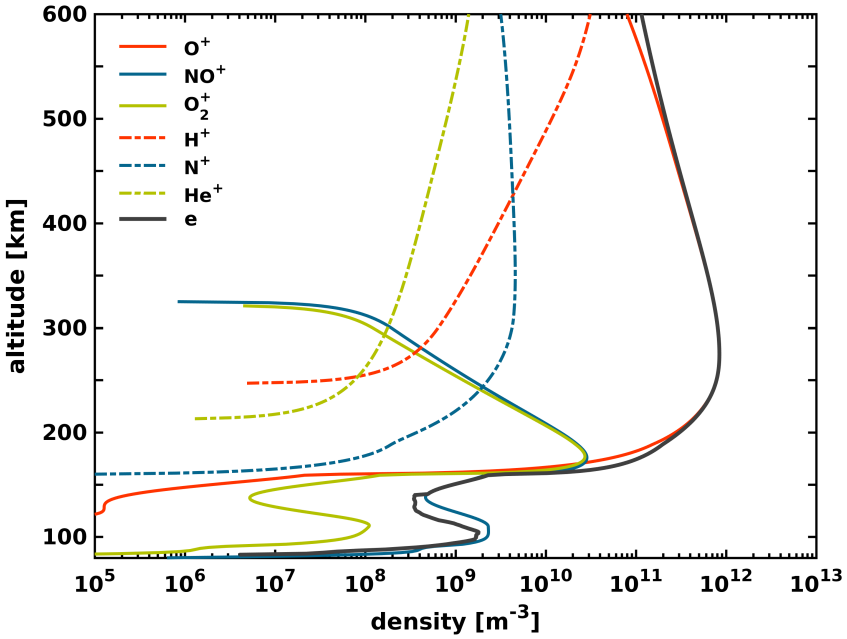

Fig. 2.2 Altitudinal profiles of densities of major species during nighttime (24 LT) on March equinox at the dip equator and solar index F10.7=82 sfu. The horizontal axis is in logarithmic scale for visualization.

(O^+). Above it, the electron density decreases, and hydrogen (H^+) and helium (He^+) ions become relevant. Below 150 km until about 90 km, the E region takes place. The dominant ions are molecular (NO^+, O_2^+, N_2^+). This region varies importantly from day to night due to the higher recombination rate of molecular ions with electrons. During the nighttime, the F_1 layer decays, and a distinct *E-F valley* region separates the E and F_2 layers. Below about 90 km the D region is located. The dominant source of ionization is photoionization of NO by atomic hydrogen Lyman α. High energy cosmic rays also contribute to the ionization of O_2 and N_2 at these altitudes (e.g., Kelley, 2009; Pfaff, 2012; Schunk and Nagy, 2009).

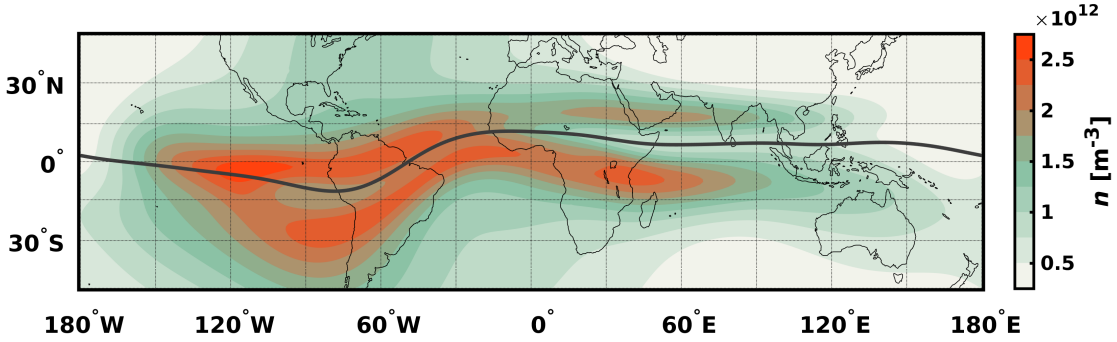

Fig. 2.3 Global map of electron density (n) at 350 km of altitude and 19 UTC. It describes the double plasma density peak typical of the EIA at low latitudes. The gray solid line depicts the dip equator.

A special plasma dynamics characterize the low-latitude ionosphere. Figure 2.3 shows a global map of the electron density at 350 km taken from IRI. The unique plasma structure of two maxima of electron density north and south of the dip equator is commonly known as the *equatorial ionization anomaly* (EIA). Although the EIA is a typical daytime feature, its structure can last until late night time. The anomaly is the result of both the lift of plasma at the dip equator by the eastward electric field in the daytime (Appleton, 1946) and its downward movement along magnetic field lines by diffusion and gravity. Another characteristic of the low-latitude ionosphere is an enhanced vertical drift ($\mathbf{E} \times \mathbf{B}$) in the F region after sunset, commonly referred to as *pre-reversal enhancement* (PRE). This phenomenon causes a brief and intense uplift of the electric field, therefore of the vertical drift near sunset, which results in a height increase in the equatorial ionosphere (e.g., Kelley et al., 2009, and references therein). Based mostly on incoherent scatter radar measurements at Jicamarca, it has been shown that the intensity of the PRE exhibits seasonal, longitudinal, and solar cycle dependencies (Scherliess and Fejer, 1999). Figure 2.4 reproduces from Farley et al. (1986) the altitudinal average of F region vertical drift from incoherent scatter

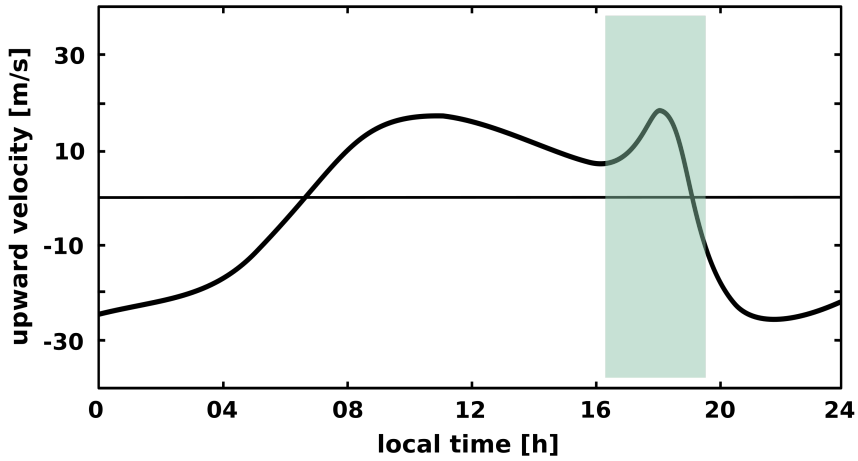

Fig. 2.4 Averaged *F* region vertical plasma drift velocity data from Jicamarca (76.87°W, 11.95°S geographic) during the equinoxes of the maxima of solar cycles 20 and 21. The green-shade highlights the *pre-reversal enhancement* (PRE) period. *Adapted from* Farley et al. (1986).

observations at the *Jicamarca Radio Observatory* during the equinoxes of the maxima of solar cycles 20 and 21. The figure highlights in green the sudden increase in the vertical drift typical of the PRE. In general, this phenomenon has been attributed to processes related to eastward neutral winds and differences in the conductivity between the *E* and *F* regions near the sunset terminator, resulting in polarization electric fields (Eccles, 1998; Farley et al., 1986; Rishbeth, 1971). By using the thermosphere-ionosphere-electrodynamics general circulation model (TIEGCM) coupled with the global ionosphere-plasmasphere (GIP) model, Richmond et al. (2015) show that ionospheric eastward convection increases into the evening and connects to upward/poleward convection that constitutes the PRE. Additionally, the authors find that the winds driving the PRE lie mainly on magnetic field lines with apexes above the peak of the equatorial *F* region (above 400 km). These field lines extend in magnetic latitude out to nearly 30°, which encloses the entire evening EIA region.

2.2 Electric current system

Vertical drifts and neutral winds are essential in the dynamics of the ionosphere. The distribution of electric fields and currents depends on the characteristics of global winds above 90 km, a region called the thermosphere. The leading effect driving thermospheric neutral winds is the diurnal variation in the absorption of solar ultraviolet radiation, which heats and expands the dayside thermosphere, generating day-to-night horizontal pressure

gradients (Richmond, 1995). The response of ions and electrons to neutral winds is different. In both *E* and *F* regions, the electrons are essentially unaffected by neutral gas motions. On the contrary, the ions move in the direction of the wind at low altitudes (below about 120 km), and perpendicular to the wind and the ambient magnetic field at higher altitudes. On the other side, electric fields move the electrons in the $\mathbf{E} \times \mathbf{B}$ direction at all altitudes above about 100 km. Differently, the ions move very slow in the direction of the electric field at low altitudes and almost in the direction of $\mathbf{E} \times \mathbf{B}$ at the higher altitudes (Heelis, 2004).

The ionosphere can be described by the continuity equation for ions and electrons (i, e),

$$\frac{\partial n_{i,e}}{\partial t} + \nabla \cdot (n_{i,e}\mathbf{v}_{i,e}) = P_{i,e} - L_{i,e}, \tag{2.1}$$

and the charge conservation equation,

$$\nabla \cdot \mathbf{j} \equiv e\nabla \cdot [n(\mathbf{v}_i - \mathbf{v}_e)] = 0, \tag{2.2}$$

where $\mathbf{v}_{i,e}$ is the ion or electron velocity; n is the plasma number density; $n_{i,e}$ is the number density of ions or electrons; $P_{i,e}$ and $L_{i,e}$ are the production and loss rates of ions or electrons; j is the current density and the quasi-neutrality condition (i.e., $n_e = n_i = n$) is assumed. In a state of equilibrium the flow velocities $\mathbf{v}_i$ and $\mathbf{v}_e$ are determined from the momentum balance equations,

$$0 = -\nabla p_i + ne(\mathbf{E} + \mathbf{v}_i \times \mathbf{B}) - nm_i\nu_i(\mathbf{v}_i - \mathbf{U}) + nm_e\nu_{ei}(\mathbf{v}_e - \mathbf{v}_i) + nm_i\mathbf{g}, \tag{2.3}$$

$$0 = -\nabla p_e - ne(\mathbf{E} + \mathbf{v}_e \times \mathbf{B}) - nm_e\nu_e(\mathbf{v}_e - \mathbf{U}) - nm_e\nu_{ei}(\mathbf{v}_e - \mathbf{v}_i) + nm_e\mathbf{g}, \tag{2.4}$$

where $p_{i,e}$ is the ion or electron pressure; e is the charge; $\mathbf{E}$ is the electric field; $\mathbf{B}$ is the magnetic field; $m_{i,e}$ is the ion or electron mass; $\nu_{i,e}$ is the ion or electron collision frequency with neutrals; $\mathbf{U}$ is the neutral wind velocity; ν_{ei} is the electron-ion collision frequency, and $\mathbf{g}$ is the gravitational acceleration.

The *ionospheric wind dynamo* describes electric fields and currents that result from the motion of the neutral atmospheric gas and its collision with charged particles. The wind motion driven by tidal oscillations works as an electrical generator (i.e., *dynamo*), converting

mechanical to electrical energy. At low-latitudes, tidal oscillations driven by absorption of solar radiation in the thermosphere, stratosphere, and troposphere dominate the neutral wind motion in the *E* region. Absorption of EUV solar radiation in the upper atmosphere generates *in situ* neutral winds in the *F* region (Heelis, 2004). Therefore, owing to the dependence of the *dynamo* currents to solar radiation, their highest magnitudes occur during daytime.

For a given neutral wind system, the ionospheric current density $\mathbf{j}$ and electric field $\mathbf{E}$ can be expressed in a steady state as,

$$\mathbf{j} = \sigma_o \mathbf{E}_{\parallel} + \sigma_P(\mathbf{E}_{\perp} + \mathbf{U} \times \mathbf{B}) + \sigma_H \hat{\mathbf{b}} \times (\mathbf{E} + \mathbf{U} \times \mathbf{B}), \tag{2.5}$$

$$\mathbf{E} = -\nabla\Phi, \tag{2.6}$$

where $\mathbf{E}_{\parallel}$ and $\mathbf{E}_{\perp}$ are the components of $\mathbf{E}$ parallel and perpendicular to the Earth's magnetic field $\mathbf{B}$; $\hat{\mathbf{b}}$ is a unit vector in the direction of $\mathbf{B}$ and Φ is the electrostatic potential. The coefficients σ_o, σ_P and σ_H are the parallel (to $\mathbf{B}$), Pedersen and Hall conductivities, respectively, as given by

$$\sigma_o = ne^2\left(\frac{1}{m_e \nu_e} + \frac{1}{m_i \nu_i}\right), \tag{2.7}$$

$$\sigma_P = ne^2\left[\frac{\nu_e}{m_e(\omega_e^2 + \nu_e^2)} + \frac{\nu_i}{m_i(\omega_i^2 + \nu_i^2)}\right], \tag{2.8}$$

$$\sigma_H = ne^2\left[\frac{\omega_e}{m_e(\omega_e^2 + \nu_e^2)} - \frac{\omega_i}{m_i(\omega_i^2 + \nu_i^2)}\right], \tag{2.9}$$

where $\omega_{e,i}$ is the electron or ion gyrofrequency (i.e., $\omega_{e,i} = e|\mathbf{B}|/m_{e,i}$).

Figure 2.5 exhibits altitude profiles of ionospheric conductivities during daytime and nighttime. For their computation, the density of electrons and the three most abundant ion species, i.e., atomic oxygen (O^+), nitric oxide ions (NO^+), and molecular oxygen ions (O_2^+) are from the *International Reference Ionosphere* (IRI) model (Bilitza et al., 2017). The plasma mobilities were calculated using temperatures and composition of neutrals from the *Mass Spectrometer and Incoherent Scatter* (NRL-MSISE00) model (Picone et al., 2002). Ion-neutral and electron-neutral collision frequencies are taken from Schunk and Nagy (2009). In the ionosphere, the parallel conductivity is much larger than the Pedersen and Hall

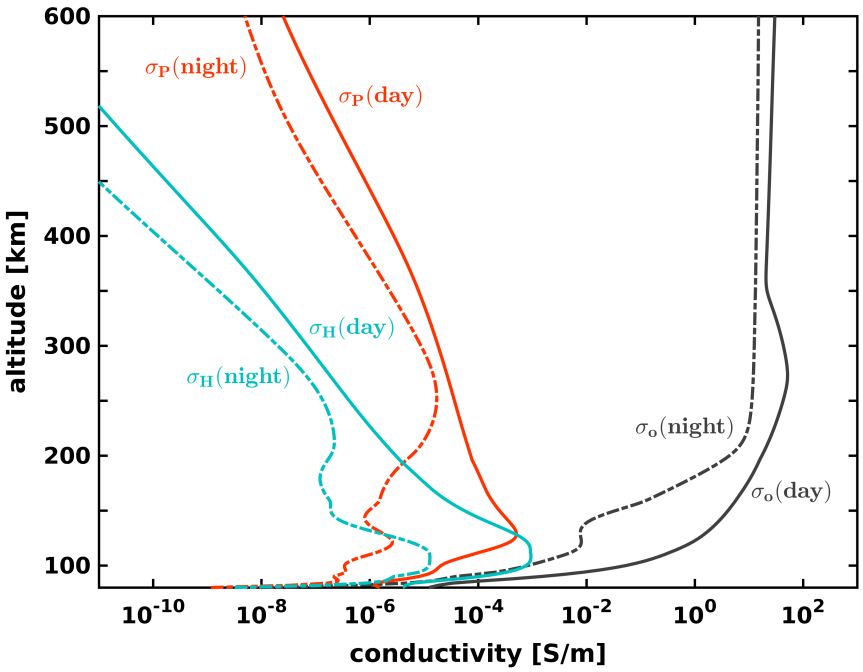

Fig. 2.5 Altitude profiles of ionospheric conductivities during daytime (12 LT, solid-lines) and nighttime (24 LT, dashed-lines) on March equinox at the dip equator and solar index F10.7=82 sfu: parallel (σ_o) in black, Pedersen (σ_P) in red, and Hall (σ_H) in blue. The horizontal axis is in logarithmic scale for visualization.

conductivities either during daytime or nighttime. The Pedersen conductivity presents its highest magnitude during daytime at the E region. The highest magnitude during nighttime occurs at the F region with values comparable to those of the day — the Hall conductivity peaks at the E region during daytime and nighttime. Due to the large magnitude of the parallel conductivity, it is commonly assumed to be effectively infinite ($\sigma_o = \infty$), so that the parallel electric field must be zero and the electric potential constant along magnetic field lines.

The Pedersen conductivity is essential for the circulation of horizontal currents in the ionosphere. The so-called solar quiet (S_q) dynamo is a daytime-current system of global scale which forms current loops center at mid-latitudes flowing anti-clockwise and clockwise at the northern and southern hemispheres, respectively. Both the Hall and Pedersen conductivities enable the existence of the most substantial *dynamo* current referred to as the *equatorial electrojet*. It is a daytime eastward current flowing at the E region that results from the significant effective zonal conductivity along the dip equator, known as the *Cowling effect* (e.g., Yamazaki and Maute, 2017, and references therein). It has also been shown that the

Hall conductivity affects the PRE, but negatively rather than positively. If Hall conductivity is eliminated, the PRE strengthens (Richmond and Fang, 2015). On the other hand, despite the assumption of $\sigma_o = \infty$, the hemispherical asymmetry in both neutral winds and ionospheric conductivities allows the existence of interhemispheric field-aligned currents and vertical currents above the magnetic equator. These currents have been successfully confirmed using magnetic field measurements from different satellite missions (e.g., Lühr et al., 2015a; Olsen, 1997; Park et al., 2011).

Different to the *dynamo* currents, there is a group of currents that do not depend on the ionospheric conductivity but the interaction of the plasma with gravitational and magnetic fields. Following the earlier assumption of a steady-state ionosphere with time-invariant global electric field, Eq.(2.6), and divergence-free current density, Eq.(2.2), two additional electric currents referred to as gravity-driven ($\mathbf{j_g}$) and plasma pressure-driven ($\mathbf{j_d}$) currents are defined as

$$\mathbf{j_g} = nm_i\left(\frac{\mathbf{g}\times\mathbf{B}}{B^2}\right), \tag{2.10}$$

$$\mathbf{j_d} = -\frac{\nabla p\times\mathbf{B}}{B^2}, \tag{2.11}$$

where $p = nk(T_i + T_e)$ is the plasma pressure, k is the Boltzmann constant, T_i and T_e are the ion and electron temperatures respectively. Therefore, a total current density in the ionosphere can be expressed as the sum of Eqs.(2.5), (2.10), and (2.11).

The gravity-driven current $\mathbf{j_g}$ is the result of the drift perpendicular to both the ambient magnetic and gravity fields of electrons and ions in opposite directions. The negligible mass of the electrons makes the movement of the ions to lead the current. Due to its dependence on plasma density, $\mathbf{j_g}$ is expected to be most active at the crests of the EIA in the F region (Alken et al., 2011). Since the EIA is still active until later hours, the gravity-driven current might play an essential role during the night. The plasma pressure-driven current $\mathbf{j_d}$, also known as diamagnetic current, flows perpendicular to both the ambient magnetic field and the plasma pressure gradient. In a steady-state, the current $\mathbf{j_d}$ arises from the balance between the plasma pressure gradient force and the Lorentz force,

$$\nabla p = \mathbf{j}\times\mathbf{B}, \tag{2.12}$$

where the plasma must also satisfy the Maxwell's equation,

$$\nabla \times \mathbf{B} = \mu_0 \mathbf{j}, \tag{2.13}$$

where μ_0 is the permeability of free space. The combination of Eq.(2.12) and Eq.(2.13) results in,

$$\nabla\left(p + \frac{B^2}{2\mu_0}\right) = \frac{1}{\mu_0}(\mathbf{B}\cdot\nabla)\mathbf{B}, \tag{2.14}$$

which relates the plasma pressure and magnetic pressure forces in the left-hand side, with the magnetic tension due to the curvature of the magnetic field lines in the right-hand side.

2.3 Equatorial plasma depletions

Equatorial plasma depletions are low plasma density structures aligned with the Earth's magnetic field. They appear in the low-latitude ionosphere right after sunset. EPDs are well-known for their adverse effect on the propagation of radio waves. Plasma irregularities associated with EPDs deteriorate the quality of the signals of telecommunication satellites as well as of those of remote sensing, weather, and scientific satellites. They also affect the accuracy of navigation systems generating a loss of the signal (e.g., Jivani et al., 2000; Vesecky et al., 1980; Xiong et al., 2016a).

EPDs correspond to large-scale structures (10-100 km) associated with one specific type of plasma irregularities known as equatorial Spread F or topside F region irregularities. EPDs are observed as largely depleted plasma density channels or plumes that significantly disrupt the ionospheric equilibrium density profiles. Their altitude generally ranges from the bottomside F region up to 2000 km due to strong zonal polarization electric fields (e.g., Chaturvedi and Ossakow, 1977; Perkins et al., 1973). This altitude range is detected with precision by radars which are sensitive to small-scale irregularities associated with ESF (about 3 m, half the wavelength of the radar frequency). Figure 2.6 adapted from Woodman and La Hoz (1976) depicts backscattered echoes related to ESF recorded at Jicamarca. The development of a plume is observed at the bottomside around 23 LT, reaching altitudes of approximately 600 km in less than an hour. Other instruments are sensitive to different scale-sizes of plasma structures associated with ESF. Far ultraviolet sensors like the one onboard the *Global-scale Observations of the Limb and Disk* (GOLD) mission provides OI 135.6 nm nightglow images. They show large-scale airglow depletions (about 100s km) related to ESF (e.g., Eastes et al., 2019). Depleted structures of this kind are also gathered

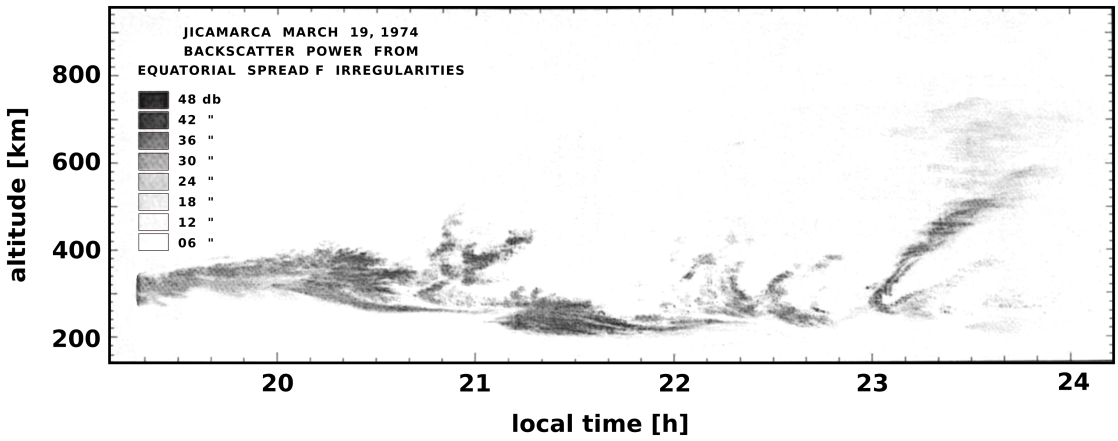

Fig. 2.6 Range-time-intensity of backscattered echoes from equatorial Spread *F* at 75°W. *Adapted from* Woodman and La Hoz (1976).

by OI 630.0 nm nightglow images from all-sky imagers at the ground (e.g., Martinis and Mendillo, 2007). Measurements of plasma density by LEO satellites like *Swarm* usually detect EPDs within the range of tens to hundreds of kilometers (e.g., Rodríguez-Zuluaga and Stolle, 2019; Xiong et al., 2016b).

2.3.1 Driving mechanisms

The physical mechanism responsible for ESF was debated in the 1970s. By then, two likely candidates had strong support, the $\mathbf{E} \times \mathbf{B}$ drift (Martyn, 1959) and *Rayleigh-Taylor* instability (Dungey, 1956). Nevertheless, none of them seemed to explain the broad spectrum or range of altitude of the irregularities depicted by observations (Farley et al., 1970). In an unpublished manuscript, Haerendel (1973) attributed the largest scales of ESF to *Rayleigh-Taylor* instabilities and the smaller scales to drift wave instabilities. To extend the altitude range of the primary instability on top of the *F* region peak, the author included a flux tube integrated formalism in his linear growth rate calculations. However, it was Woodman and La Hoz (1976) that interpreted the high-altitude irregularities as resulting from the nonlinear phase of the *generalized Rayleigh-Taylor* instability (gRTI).

The gRTI is a particular case of the *Rayleigh-Taylor* instability. It takes into account not only the influence of gravity but also of the ambient electric field and neutral winds. The gRTI takes place at the bottomside *F* region (about 200 km) where the plasma density gradient (∇n) is positive upward. The instability can occur because the magnetic field makes the function of a light fluid supporting the plasma against the gravitational force, as shown in Figure 2.7.

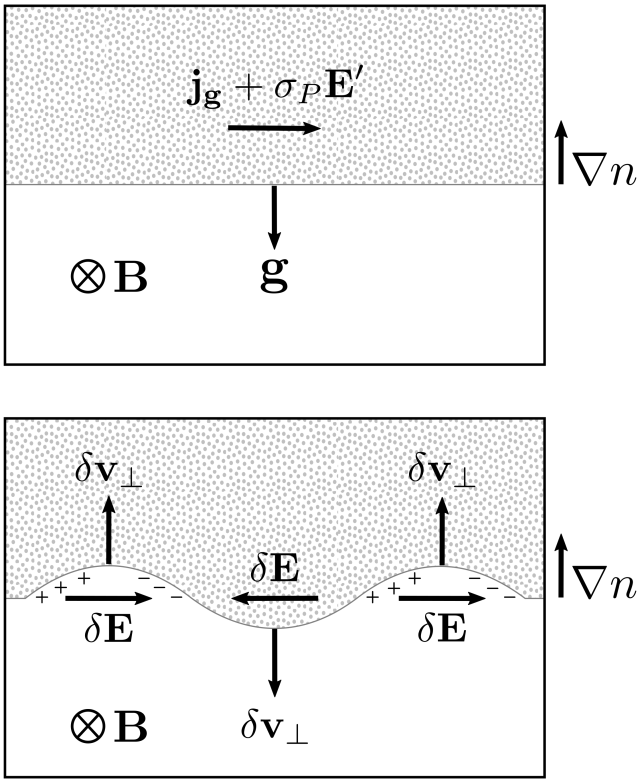

Fig. 2.7 (Top) A plasma in a gravitational field $\mathbf{g}$ supported by a magnetic field $\mathbf{B}$. (Bottom) Development of a perturbation. $\mathbf{j_g} + \sigma_P \mathbf{E}'$ causes charges to accumulate along the boundary, leading to electric fields $\delta \mathbf{E}$ and $\delta \mathbf{v}_\perp$ drifts that amplify the perturbation.

Once a perturbation develops in the boundary as a result of random density fluctuations, the zonal currents $\mathbf{j_g}$ defined in Eq.(2.10) and $\sigma_P \cdot \mathbf{E}'$ (where $\mathbf{E}' = \mathbf{E}_\perp + \mathbf{U} \times \mathbf{B}$) described in the second term of Eq.(2.5), make the perturbation to grow. The two eastward currents lead to an accumulation of positive charges at the boundary. As a result, a polarization electric field $\delta \mathbf{E}$ evolves, generating vertical drifts, $\delta \mathbf{v}_\perp = \delta \mathbf{E} \times \mathbf{B}/B^2$. As depicted in Figure 2.7, upward and downward $\delta \mathbf{v}_\perp$ amplify the initial perturbation. The role of the ambient eastward electric field in the gRTI, is to make the plasma unstable through drift instabilities and to move the plasma vertically upward so that the growth rate (γ) of the gRTI becomes large due to the smaller values of the ion-neutral collision frequency v_i at high altitudes, described by Basu (2002) as,

$$\gamma = \frac{1}{L_n}\left(\frac{g}{v_i} + \frac{E_y}{B} - U_x + \frac{v_i}{\omega_i} U_y\right), \tag{2.15}$$

where $1/L_n = d(\ln n)/dx$ is the inverse density gradient scale length. Here x and y are the components perpendicular to the ambient magnetic field, pointing radially upward and zonally eastward, respectively. The *pre-reversal enhancement* of the zonal electric field, PRE, gives the vertically upward movement of the plasma to trigger the gRTI each evening. Clear evidence of the direct relationship between the PRE and the occurrence of EPDs has been given by Stolle et al. (2008). The authors compare independent climatological data set of the occurrence rate of EPDs obtained from CHAMP with vertical plasma drift velocities obtained from ROCSAT-1 measurements. They show that the longitudinal variation in the magnitude of the PRE correlates with the occurrence rate of EPDs to about 90%.

In the last decades, the presence of *collisional shear* instabilities (CSI) has also been shown to play an essential role in the development of ESF (e.g., Aveiro and Hysell, 2010; Hysell and Kudeki, 2004; Kudeki et al., 2007). It is known that at dusk there is a strong shear in bulk plasma motion in the equatorial F region ionosphere with westward drifts at the bottomside and eastward drifts above (Kudeki et al., 2007, 1981; Tsunoda et al., 1981). Different factors such as vertical currents sourced in the electrojet region, E region dynamo winds and vertical winds are considered to contribute to shear flow, though it is unknown which of them is more critical (Hysell and Kudeki, 2004). At the bottomside, the plasma drifts westward, a kind of irregularities known as *bottom-type* are often observed (see Figure 2.6). They usually appear promptly after sunset, remaining for several hours confined to layers less than 50 km thick without developing vertically (Hysell, 2000). Kudeki and Bhattacharyya (1999) claim that *bottom-type* irregularities are the result of wind-driven gradient drift instabilities in regions where the local plasma velocity and neutral wind are antiparallel. This statement is supported by radar imagery presented by Hysell et al. (2004). Even though different seed mechanisms for waves that produce EPDs have been suggested, *bottom-type* irregularities would seem to be an ever-present source of seed irregularities for EPDs (Hysell, 2000). Numerical simulations of EPDs show that the combination of both the *generalized Rayleigh-Taylor* and *collisional shear* instabilities is more effective than the former alone and can produce growing waveforms with features similar to those observed by satellites, radars and airglow sensors (Aveiro and Hysell, 2010).

2.3.2 Electrostatic characteristics

The presence of depleted plasma density channels in the topside ionosphere changes the electric current configuration of the ambient plasma. Evidence of these are the electric and magnetic field perturbations observed by satellite missions such as the *Atmosphere Explorer*

(AE) (e.g., McClure et al., 1977), *Defense Meteorological Satellite Program* (DMSP) (e.g., Huang et al., 2001), *San Marco D* (e.g., Aggson et al., 1992b), *Communication/Navigation Outage Forecasting System* (C/NOFS) (e.g., Burke et al., 2012), and *Challenging Minisatellite Payload* (CHAMP) (e.g., Stolle et al., 2006). These fields are the result of electric currents associated with the spatial and temporal evolution of EPDs. Such electromagnetic signatures are useful for the detection of EPDs by LEO satellite missions (e.g., Park et al., 2013; Stolle et al., 2006). They are also a fundamental source of information to understand the electromagnetic nature of both the EPDs and the ambient plasma where they are embedded. Nevertheless, the limitation of the observations to capture the full EPD phenomenon makes numerical simulations essential to comprehend the electromagnetic characteristics of a whole EPD at a given time. In this regard, two approximations are generally used to simulate the generation and evolution of EPDs, one under electrostatic conditions (e.g., Aveiro and Hysell, 2010; Huba et al., 2008; Yokoyama et al., 2014) and other based on electromagnetic conditions (e.g., Dao et al., 2013). Simulations of satellites passing through EPDs have shown that numerical models can reproduce magnetic fluctuations related to currents at EPDs with magnitudes similar to the ones measured by satellites (e.g., Aveiro et al., 2011; Yokoyama and Stolle, 2017).

Poynting flux and field-aligned currents

The study of coupling processes between the magnetosphere and ionosphere, and between the ionospheric *F* and *E* regions, is commonly addressed by the analysis of electromagnetic energy flow between the regions. The idea behind is to determine the rate of energy conversion using the principle of conservation of electromagnetic energy (Poynting's theorem). The energy conversion rate $\mathbf{E}\cdot\mathbf{j}$ is related to the rate of both Joule heating of the plasma and momentum transfer between ions and neutrals in the lower ionosphere (Gary et al., 1994). The Poynting flux parallel to the magnetic field lines ($\mathbf{S}_{\parallel}$) is generally described as,

$$\mathbf{S}_{\parallel} = \frac{1}{\mu_0}(\delta\mathbf{E}_{\perp} \times \delta\mathbf{B}_{\perp}). \tag{2.16}$$

The $\mathbf{S}_{\parallel}$, as determined from satellite measurements, was first used by Knudsen et al. (1990) to study the magnetosphere-ionosphere coupling at high-latitudes. The primary assumption to determine the rate of electromagnetic energy conversion by *in situ* measurements is the prevalence of a steady-state.

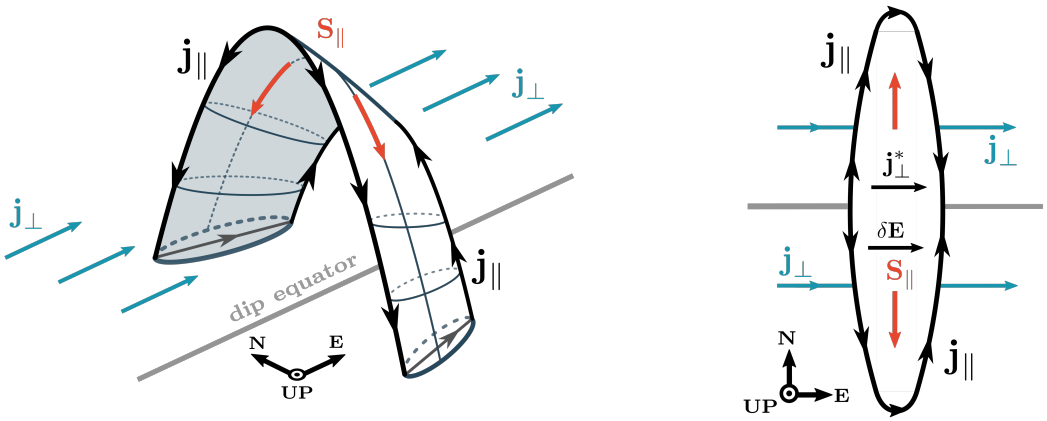

Fig. 2.8 General (left) and top view (right) of an EPD depicted as a depleted magnetic flux tube. It describes field-aligned currents ($\mathbf{j}_{\parallel}$), zonal currents outside ($\mathbf{j}_{\perp}$) and inside ($\mathbf{j}^{*}_{\perp}$) the EPD, polarization electric field ($\delta\mathbf{E}$) and field-aligned Poynting flux ($\mathbf{S}_{\parallel}$). The sketches describe the Poynting flux and electric current configurations as suggested by theoretical studies.

In the case of the Poynting flux associated with EPDs, little is known from observations due to the lack of simultaneous high-resolution measurements of magnetic and electric fields. Figure 2.8 shows a general (left) and a top view (right) of an EPD. It depicts the orientation of $\mathbf{S}_{\parallel}$ and related currents as suggested by theoretical studies (e.g., Aveiro and Hysell, 2012; Bhattacharyya and Burke, 2000; Burke, 1979; Dao et al., 2013; Yokoyama and Stolle, 2017). Outside the EPD, zonal currents ($\mathbf{j}_{\perp}$) are mainly the sum of gravity-driven, Pedersen and inertial currents. Inside the EPD, zonal currents ($\mathbf{j}^{*}_{\perp}$) build to maintain the current continuity through Pedersen and gravity-driven currents. The Poynting flux is directed away from the dip equator, which implies an eastward polarization electric field ($+\delta\mathbf{E}$) and magnetic fluctuations ($\delta\mathbf{B}$) perpendicular to the ambient field with different polarity at each magnetic hemisphere, as Eq.(2.16) suggests. These magnetic fluctuations are the result of field-aligned currents ($\mathbf{j}_{\parallel}$) at the edges of EPDs, as described by Ampère's law,

$$\mathbf{j}_{\parallel} = \frac{1}{\mu_0}\left(\frac{\partial B_y}{\partial x} - \frac{\partial B_x}{\partial y}\right). \tag{2.17}$$

For this particular case, the currents, $\mathbf{j}_{\parallel}$, flow away from the dip equator at the western edge of the EPD and towards the dip equator at the eastern edge (Figure 2.8).

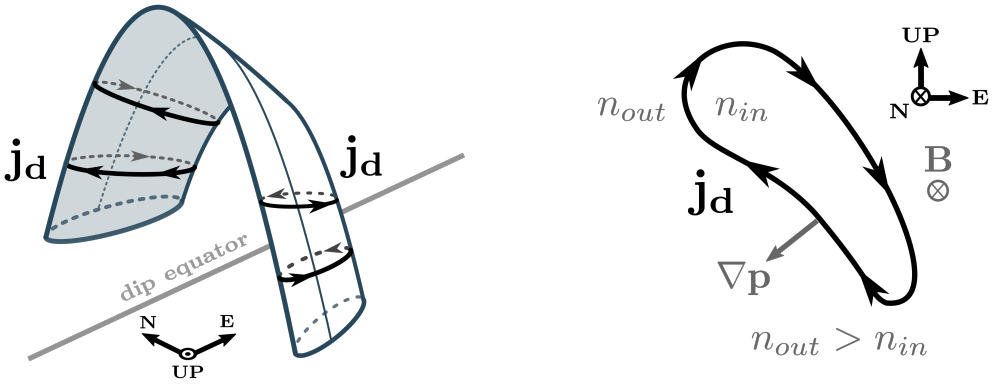

Fig. 2.9 (left) General view of an EPD depicted as a depleted magnetic flux tube and (right) zonal-cross section at the dip equator of the EPD on the left. It shows diamagnetic currents ($\mathbf{j_d}$) and plasma pressure gradient (∇p).

Few studies based on in situ magnetic measurements have dealt with $\mathbf{j}_{\parallel}$ at EPDs (e.g., Park et al., 2009; Stolle et al., 2006). However, they have not gathered conclusive evidence on whether the direction of the Poynting flux is as suggested by theoretical studies.

Diamagnetic currents

In magnetized plasmas such as the ionosphere, plasma pressure gradients ($\nabla p = \nabla(nkT)$) are the source of diamagnetic currents ($\mathbf{j_d}$), as described by Eq.(2.11). In the case of EPDs, the plasma pressure gradient has always been assumed to be positive (i.e., pointing out of the EPD) (e.g., Aveiro et al., 2011; Dao et al., 2013; Stolle et al., 2006). That means, the EPDs generally present low plasma pressure relative to the background, as depicted in Figure 2.9. In this regard, diamagnetic currents must flow in such a way that they increase the magnetic field inside the EPD and decrease it outside (clockwise flow). Assuming a steady-state, isotropic plasma pressure, and ignoring the magnetic tension due to the curvature of the magnetic field lines described in the right-hand side of Eq.(2.14) gives a relation between plasma and magnetic pressure,

$$\nabla\left(\frac{B^2}{2\mu_0}+p\right)=0 \;\Rightarrow\; \nabla B=-\mu_0\frac{\nabla p}{B}, \tag{2.18}$$

such that, under thermodynamic equilibrium where plasma pressure variations are governed by the density,

$$\nabla B = -\mu_0 k(T_i + T_e)\frac{\nabla n}{B}. \tag{2.19}$$

These assumptions stand on the fact that EPDs are much smaller than the bending radius of the ambient magnetic field lines. Lühr et al. (2003) confirm the validity of these assumptions by analyzing the diamagnetic effect associated with the EIA using observations from CHAMP. The authors find magnetic fluctuations of the order of 5 nT consistent with the predicted effect by Eq.(2.19). In the same fashion, this magnetic characteristic allows the detection of EPDs due to its direct relation with plasma density variations. In the first systematic use of this feature, Stolle et al. (2006) present distinct magnetic fluctuations related to $\mathbf{j_d}$ at EPDs. In the absence of high-resolution electron density measurements, the authors use the diamagnetic effect to assess the global occurrence rate of EPDs, finding good agreement with studies based on plasma density measurements (e.g., Gentile et al., 2006). The use of numerical simulations has also reproduced magnetic fluctuation with magnitudes similar to those detected by LEO satellites, all of them assuming EPDs to present lower plasma pressure relative to the background (e.g., Aveiro et al., 2011; Dao et al., 2013; Yokoyama and Stolle, 2017). This assumption implies a near isothermal process across EPDs and suggests that pressure variations are dominated by the plasma density mostly.

Chapter 3

The *Swarm* constellation mission

The use of space-based magnetometers began with *Sputnik 3* in 1958 (Dolginov et al., 1959), followed by *Cosmos* 26 and *Cosmos* 49 satellites in 1964. The first high-precision measurements of the Earth's magnetic field were made by the *OGO-2* satellite in 1965 as part of the *Polar Orbiting Geophysical Observatories* (POGO) satellite series. It measured the intensity of the magnetic field but not its direction. Significant progress was made in 1979 with the first detailed magnetic observations of the Earth's field by the single-satellite mission *Magsat* (Langel et al., 1982), the first global vector survey. Nonetheless, it was not until the launch of *Ørsted* in 1999 (Neubert et al., 2001), approximately twenty years after *Magsat*, that the current era of Earth-space magnetometry started. A couple of months after *Ørsted* two additional satellite missions, CHAMP, and the *Satélite de Aplicaciones Científicas-C* (SAC-C), were launched, together providing data for more than a decade. Further information on satellite geomagnetism can be found in Olsen and Stolle (2012).

The *Swarm* constellation is a satellite mission of the *European Space Agency* (ESA) dedicated to studying the Earth's magnetic field and its temporal evolution (Friis-Christensen et al., 2006). Different payloads onboard provide not only high-precision measurements of the magnetic field, but of the electron density, ion-drift, and electron and ion temperatures. In this chapter, I summarized the mission by briefly addressing the orbits and their spatial and temporal evolution since its launch. To better understand the results of this dissertation, I focused merely on the measurements used, which correspond to the magnetic field, electron density, and ion-drift.

3.1 Orbits

The *Swarm* mission consists of three identical satellites named *Alpha*, *Charlie*, and *Bravo*. They are launched on November 22, 2013, from the Plesetsk Cosmodrome into near-polar, circular orbits (Figure 3.1). During the first two months on orbit, the three satellites followed one another in a *pearls-on-a-string* arrangement. The final constellation is achieved on April 17, 2014, as indicated by the vertical gray line in Figures 3.2 and 3.3. Since then, *Alpha* and *Charlie* fly side-by-side separated by 1.4° in longitude at the equator, at 87.35° inclination angle and an initial altitude of 477 km at the equator. *Bravo* orbits at a higher initial altitude of 524 km and 87.75° inclination angle. For the date of this dissertation, the altitude at the equator of *Alpha* and *Charlie* was about 445 km, and of *Bravo* of about 512 km (Figure 3.2), 32 km and 12 km less since the achievement of the final constellation, respectively. The faster altitudinal decay of *Alpha* and *Charlie* is due primarily to the more substantial air drag at their altitudes compared to *Bravo*'s altitude.

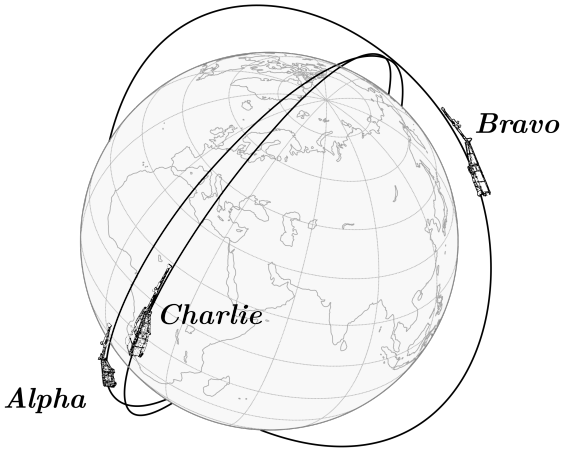

Fig. 3.1 Schematic view of the current *Swarm* constellation.

Consecutive orbits of each satellite are separated by approximately 20° in longitude at the equator. *Alpha* and *Charlie* precess in local time at a rate of about 5.4 min/day and *Bravo* at about 5.1 min/day, resulting in a complete seasonal-local time coverage after five years. That is, the climatology of ionospheric phenomena such as EPDs can be thoroughly studied after five years of continuous measurements of the *Swarm* constellation with a complete local time coverage of each season.

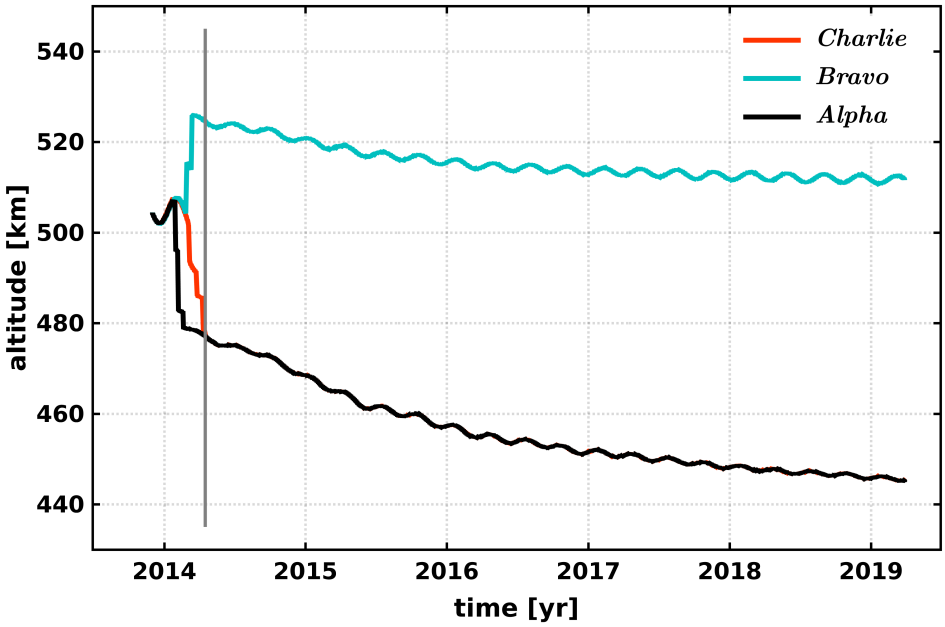

Fig. 3.2 *Swarm* altitude evolution (ascending equator). The vertical gray line indicates April 17, 2014.

The lower pair of satellites *Alpha* and *Charlie* present the same local time evolution throughout the mission (Figure 3.3, top). Due to their constant longitudinal separation of 1.4° at the equator, the two satellites also exhibit a constant difference in local time of about 4.25 min (at the equator). For the higher satellite *Bravo*, its difference in local time at the equator with *Alpha* and *Charlie* increases at a rate of roughly 1.15 hours per year (Figure 3.3, bottom). As of the writing of this dissertation, the local time difference between *Bravo* and both satellites *Alpha* and *Charlie* is of about 5.8 h, which corresponds to almost perpendicular orbits.

3.2 Payloads and measurements

All three satellites comprise the same set of instruments. It consists of an absolute scalar magnetometer (ASM), a vector field magnetometer (VFM), an electric field instrument (EFI), a three-head star tracker (STR), an accelerometer (ACC) and GPS receivers (GPSR). The EFI located at the forward-facing side of each satellite comprises two Langmuir probes (LP) and two thermal-ion imagers (TII) (see Figure 3.4). Since the results of this dissertation are based on measurements of the electron density, magnetic and electric fields, this chapter only addresses observations by the ASM, VFM, LP, and TII payloads.

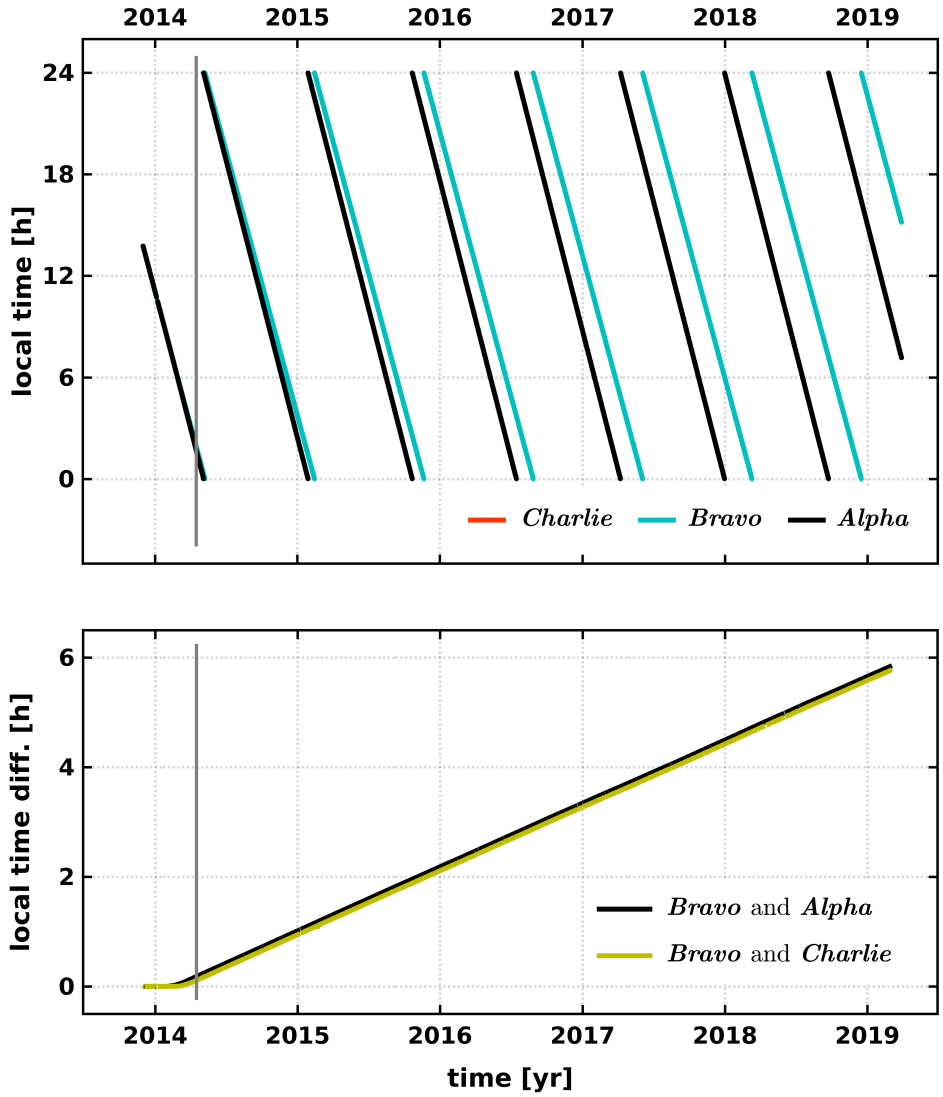

Fig. 3.3 (Top) *Swarm* local time evolution (ascending equator). (Bottom) Local time difference between *Bravo* and both *Alpha* and *Charlie*. The vertical gray line indicates April 17, 2014.

3.2.1 Magnetometers

The absolute scalar magnetometer used on *Swarm* is provided by the French group *Laboratoire d'électronique des technologies de l'information* (CEA-Leti) in partnership with the *Centre national d'études spatiales* (CNES). The required main performance characteristics of the ASM are an absolute accuracy of < 0.3 nT (2σ), a resolution < 0.1 nT within its full-scale range of 15000–65000 nT (Merayo et al., 2008). The ASM is an optically pumped ^{4}He magnetometer based on an electronic, magnetic resonance whose effects are amplified by a laser. The scalar bandwidth can be increased up to 300 Hz, though it has been set to 100 Hz so that vector modulations frequencies can be adjusted over a broader band of frequencies below 50 Hz (Leger et al., 2009). The ASM provides the absolute value of the magnetic field needed to calibrate the high-precision measurements of the magnitude and direction of the field gathered by the vector field magnetometer, VFM. The VFM is the prime instrument of the *Swarm* mission and is designed by the *Technical University of Denmark* (DTU). It is a fluxgate magnetometer based on a compact spherical coil sensor that exhibits high directional

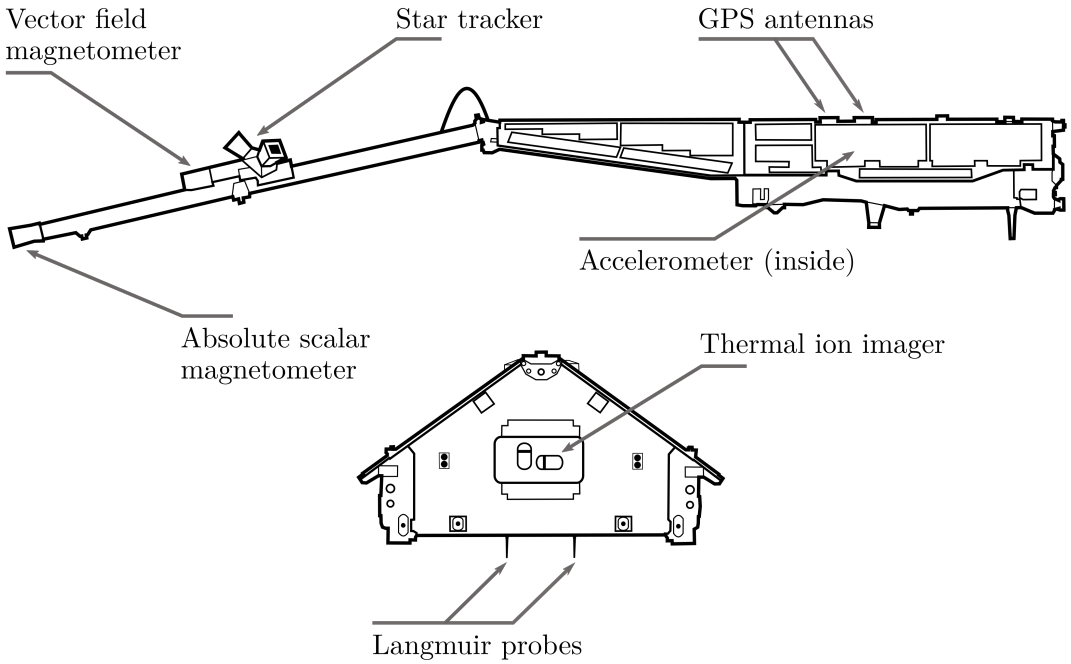

Fig. 3.4 Two views of a *Swarm* satellite and its primary payloads. (Top) It shows the ASM, VFM, STR, ACC, and GPSR. (Bottom) It depicts the TII and LPs. *Adapted from* ESA/ATG Medialab artwork.

linearity as well as thermal stability. The sampling rate is 50 Hz and has an accuracy of < 0.5 nT (Merayo et al., 2008).

The attitude provided by the star tracker assembly, STR, determines the orientation of the field's vector. The STR is also manufactured by DTU and has an accuracy better than one arc-second (0.25°). Both the VFM and STR reside together halfway the satellite's boom (Figure 3.4, top). Detailed information on the calibration and correction of the magnetic vector field measurements are given by Tøffner-Clausen et al. (2016). The magnetic data supplied for scientific purposes are of three types that depend on the sampling rate and instrument. One set contains magnetic vector data at a 50 Hz rate with no interpolation of the data. Another two sets consist of magnetic vector and scalar data at 1 Hz rate. Both VFM and ASM data are interpolated to produce these data. Tøffner-Clausen (2018) provides detailed information on the description of the data products.

3.2.2 Electric field instrument

Each of the *Swarm* satellites is equipped with a set of instruments that provide in situ measurements of plasma parameters. The Canadian company COM DEV developed the electric field instrument. It consists of two Langmuir probes, LPs, from the *Swedish Institute of Space Physics* and two thermal-ion imagers, TIIs, from the *University of Calgary*.

The LP technique involves measuring the current-voltage characteristics of one or two metal collectors to which a DC bias is administered (Abe et al., 2013). Commonly, the bias is incremented or decremented in small steps, namely, sweep. In *Swarm*, however, the LP normal mode alternates between two sub-modes, the classical sweep mode and a higher frequency harmonic mode, from which estimates of the electron density and temperature are obtained (Knudsen et al., 2017). Apart from electron density and temperature, the LP is used to determine the electric potential between the satellite and the plasma, which is essential for the TII to determine arrival angle and kinetic energy per charge of incident ions. The two TII sensors (horizontal and vertical, Figure 3.4, bottom) use an electrostatic focusing system to generate two-dimensional images of ion distribution functions. The images which are recorded by charge-coupled devices are processed to obtain three-dimensional ion velocity at a rate of 2 Hz.

Additionally, uncalibrated two-dimensional ion velocities can be estimated from 16 Hz moments. These higher-rate moments are susceptible to larger systematic errors in the ram component and are not part of the (calibrated) L1b data distribution. On the other hand, the

Knudsen et al. (2017) report a transient, secondary signal to the primary ion-drift signal that appeared after the first weeks of *Swarm* operation, likely due to the presence of water in the sensors. As a result, the operation of the instrument has been limited to one to six orbits per day and estimations of the ion-drift perpendicular to the satellite (cross-track). Cross-track velocity precision has been estimated from flight data to be better than 10 m/s (2 σ) for plasma densities greater than 10^5 cm^{-3} (Knudsen et al., 2017). Detailed information and description of the electron density and temperature data are given by Tøffner-Clausen (2018), and of the ion drift data by Burchill and Knudsen (2017).

Validation and calibration of both electron density and temperature have been performed using measurements from incoherent scatter radars and satellite radio occultation. Lomidze et al. (2018) found that the LPs systematically underestimate plasma frequencies by approximately 10% (0.5-0.6 MHz) and temperatures by 300-400 K and 700 K for high- and low-gain LPs, respectively. However, the correlation coefficients between the LP and the other measurements are sufficiently high to indicate accurate relative variations in the *Swarm* LP data ($\geq$ 0.97 for densities and 0.92-0.97 for temperatures). In an additional study, Lomidze et al. (2019) validate the cross-track ion-drift velocities in the high-latitude ionosphere. Climatological observations were compared to the corresponding climatology obtained from the Weimer 2005 empirical convection electric field model under different interplanetary magnetic field and solar wind conditions. The analysis was performed separately in the northern and southern hemispheres. The authors report that, statistically, the *Swarm* cross-track ion drift climatology agrees reasonably well with the Weimer 2005 model. The two results agree within about 200 m/s (RMS deviation); however, the correlations are higher for southward interplanetary magnetic field and in the northern hemisphere (0.84 and 0.77 for *Alpha* and *Bravo*, respectively). The corresponding magnitudes are about 14% and 33% larger than the model estimates.

Chapter 4

On the direction of the Poynting flux associated with equatorial plasma depletions as derived from *Swarm*

* *This chapter is a transcript of*
Rodríguez-Zuluaga et al. (2017).

4.1 Introduction

Equatorial plasma depletions (EPDs) are macroinstabilities observed as structures of depleted plasma density aligned with the magnetic field in the ionosphere F region. They are known to mainly occur at the nighttime geomagnetic equatorial/low latitudes when the ionosphere is unstable due to the steep density gradient in the bottomside F region. The physical mechanism responsible for the formation of EPDs was first identified by Hudson and Kennel (1975) and their propagation into the topside by Woodman and La Hoz (1976). They were described as the result of both linear and nonlinear growth phases of a plasma boundary instability under the influence of the gravitational field, normally referred as Rayleigh-Taylor or interchange instability (Hysell, 2000; Ossakow, 1981; Woodman, 2009).

Regardless of more than 80 years of efforts understanding the physics behind the occurrence of EPDs and their day-to-day-variability, only a few studies about their electromagnetic features and related Poynting flux from observations have been conducted. This is understood mainly to the lack of simultaneous measurements of both electric and magnetic field at EPDs altitudes of about 150 to 1500 km. However, several satellites have been used to report global

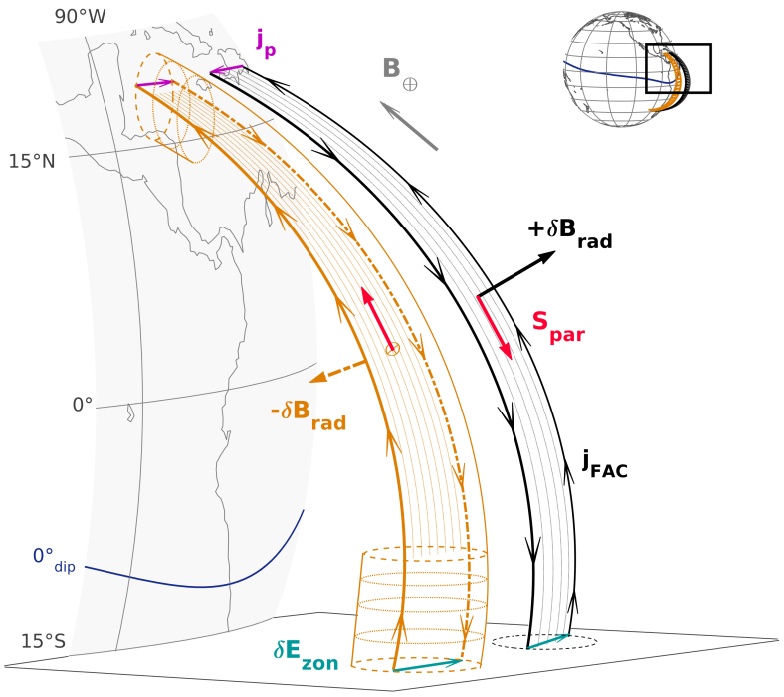

Fig. 4.1 Schematic view of two depleted flux tubes with different FACs ($\mathbf{j}_{FAC}$) configuration. The FACs related magnetic signature $\delta\mathbf{B}_{rad}$, the expected eastward polarization electric field $\delta\mathbf{E}_{zon}$, the Poynting flux $\mathbf{S}_{par}$ and the polarization currents $\mathbf{j}_p$ are depicted.

observations of EPDs, such as the Atmosphere Explorer (e.g., McClure et al., 1977), Defense Meteorological Satellite Program (e.g., Huang et al., 2001), San Marco D (e.g., Aggson et al., 1992b), Communication/Navigation Outage Forecasting System (C/NOFS) (e.g., Burke et al., 2012), and Challenging Minisatellite Payload (CHAMP) (e.g., Stolle et al., 2006) missions.

It is known that EPDs present perturbations in both electric ($\delta\mathbf{E}$) and magnetic ($\delta\mathbf{B}$) fields as a result of currents flowing along and across the depletions. Of great interest are magnetic perturbations observed as field fluctuations caused by two types of currents. The first one is attributed to diamagnetic currents (pressure-driven currents) flowing along iso-density contours across the depletions (e.g., Lühr et al., 2003; Stolle et al., 2006). They are characterized by an enhancement in the magnetic field strength within the EPDs through a balance between the magnetic and plasma pressures. The second type of currents corresponds to field-aligned currents (FACs) flowing within the edges of the depletions (e.g., Park et al., 2009). They generate transverse magnetic field perturbations as the ones depicted in Figure 4.1. By assuming electrostatic conditions, these FACs have been traditionally related to the divergence of mainly gravity-driven current at F region altitudes (e.g., Aveiro and Hysell,

2012; Huba et al., 2008; Yokoyama and Stolle, 2017). A different interpretation stands on dynamic electromagnetic characteristics assuming FACs as signatures of Alfvén waves (e.g., Bhattacharyya and Burke, 2000; Lühr et al., 2014; Pottelette et al., 2007). Despite this discrepancy, it is still assumed in either case that the FACs flow poleward (equatorward) on the external edges of the western (eastern) walls of EPDs, resulting then in a Poynting flux ($\mathbf{S}_{par}$) flowing poleward into the E region (e.g., Dao et al., 2013). Nevertheless, the observations reported in this study appear to indicate a new paradigm, consisting of an interhemispherical Poynting flux presumably flowing into the hemisphere with larger ionospheric conductivity.

By using different satellites, investigations about electromagnetic features of EPDs have been conducted using either electric or magnetic field observations (e.g., Aggson et al., 1992b; Burke et al., 2012; Park et al., 2009). In the present study, the direction of the EPDs related electromagnetic energy flux are reported using simultaneous magnetic and electric field measurements recorded onboard the *Swarm* satellites. Two recent studies by Park et al. (2016) and Park et al. (2017) report observations of the source and Poynting flux direction associated with medium-scale traveling ionospheric disturbances and Alfvén waves at high latitudes, respectively, both by using *Swarm* measurements. So far, there has been no study addressing from observations the Poynting flux related to equatorial plasma depletions.

4.2 Electric and magnetic field data

Swarm is the latest mission of the European Space Agency (ESA) to deeply explore the Earth´s magnetic field and its temporal evolution. It provides in situ simultaneous high-resolution measurements of magnetic and ion drift (electric fields), plasma density, and both electron and ion temperatures. The constellation consists of three satellites (Alpha, Bravo, and Charlie) placed on near-polar (87.5° inclination) orbits and flying with a speed of about 7.5 km/s. At the beginning of the mission after its launch on 22 November 2013, the three satellites orbited together at an altitude of about 500 km. Later on 15 April 2014, the satellites reached their final constellation. So far, Swarm Bravo orbits with a somewhat higher inclination at an altitude of $\sim$ 520 km. Swarm Alpha and Charlie fly side by side with a separation in longitude of $\sim$ 1.5° at a height of $\sim$ 460 km.

The instruments on board *Swarm* are identical for the three satellites. These are an Absolute Scalar Magnetometer (ASM) and a Vector Field Magnetometer (VSM) recording the total magnetic field at 1 Hz and the three magnetic components at 50 Hz, respectively (Tøffner-Clausen et al., 2016). A combination of both the ASM and VSM data results in

highly accurate vector magnetic field data at a rate of 1 Hz. Two Langmuir probes (LP) provide electron density and electron temperature, and a Thermal Ion Imager (TII) provides ion drift velocity (electric field) and ion temperature (Knudsen et al., 2017). The LP and TII data appear completely regular at 2 Hz rate. Because both electron density and electric field are not synchronized with the magnetic field data, the first two are decimated to a rate of 1 Hz. An initial release of *Swarm* electric field data has been made available for the period between April to September 2014 for *Swarm* Alpha and Bravo. Within this period the data coverage is not continuous and is subjected to large offsets. Then, only data with TII quality flag < 30 are considered, following the recommendation of Knudsen et al. (2015). Additionally, few days available in March 2015 are also included.

Finally, since the magnetic and electric field data are given in North-East-Centre (NEC) coordinates, the vectors are rotated into the magnetic field-aligned (MFA) coordinate system. In this frame the parallel (par) component is aligned with the mean ambient magnetic field, the zonal component (zon) is perpendicular to the magnetic meridian pointing eastward, and the radial (rad) component completes the triad pointing outward to higher L-shells.

4.3 EPDs related Poynting flux estimation

The method to detect EPDs is based on electron density $(\mathrm{N_e})$ and magnetic field data, similar to the method implemented by Park et al. (2013). Briefly, the detection is restricted to overpasses of *Swarm* between $\pm 30^\circ$ dip latitude and from 18 to 04 magnetic local time (MLT). As a first step, the electron density data is subjected to a high-pass filter in order to withdraw the background values. The resulting residual $\delta \mathrm{N_e}$ is considered if almost continuous values $\leq -0.3 \times 10^5$ cm^{-3} are present (see Figures 4.2a and 4.2b, second panel). Subsequently, in order to guarantee that such depletions correspond to EPDs, the plasma density must be correlated with the magnetic field strength and transverse components within the depletion. Hereof, the magnetic field contributions from the core, lithosphere and magnetosphere are subtracted from the magnetic field measurements by using the geomagnetic field model CHAOS6 (Finlay et al., 2016). The resulting values are residuals assumed to be of ionospheric origin $(\delta \mathbf{B}_{par}, \delta \mathbf{B}_{zon}, \delta \mathbf{B}_{rad})$.

Accordingly, the EPD events considered in this study are those that present linear correlation between $\delta \mathrm{N_e}$ and both the $\delta \mathbf{B}_{par}$ and $\delta \mathbf{B}_{rad}$ with correlation coefficients (cc) ≤ -0.6 and $|\mathrm{cc}| \geq 0.6$, respectively. These magnetic perturbations are attributed to the diamagnetic and field-aligned currents effect.

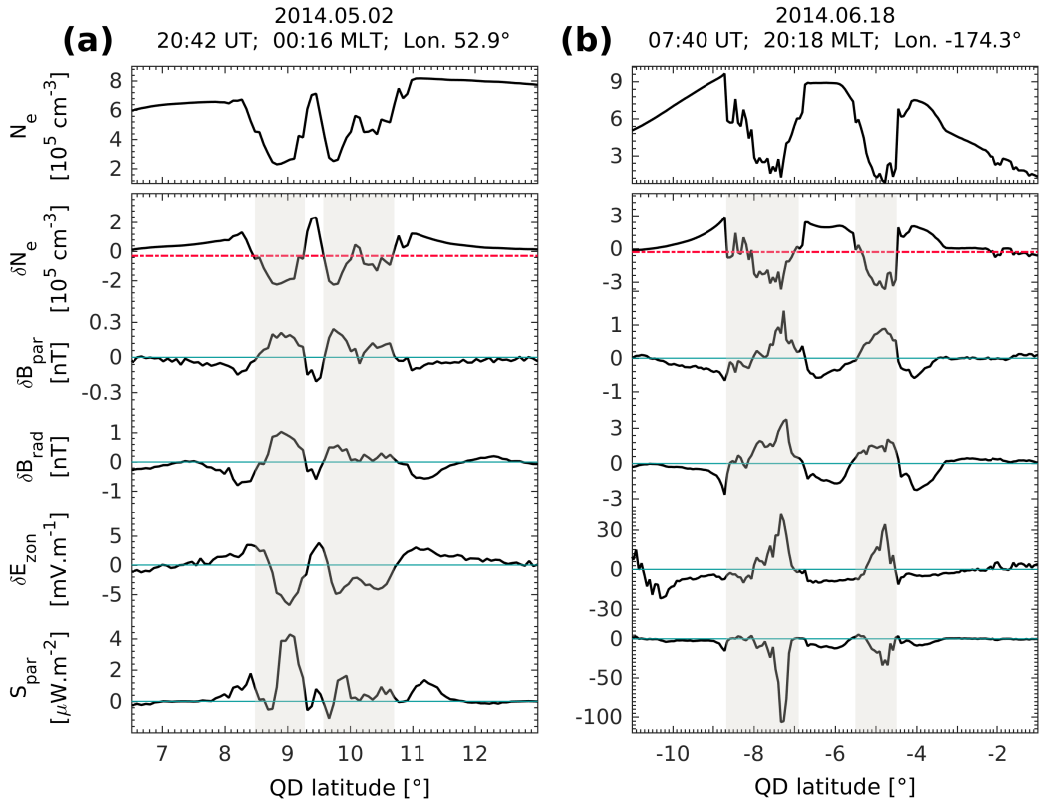

Fig. 4.2 Electromagnetic signatures of EPDs as observed by *Swarm* Alpha. From top to bottom, the electron density (N_e) and its residual (δN_e), the parallel and radial magnetic field components ($\delta \mathbf{B}_{par}, \delta \mathbf{B}_{rad}$), the zonal polarization electric field ($\delta \mathbf{E}_{zon}$) and the Poynting flux ($\mathbf{S}_{par}$). **a.** Pass over the northern magnetic hemisphere. **b.** Pass over the southern magnetic hemisphere. The δN_e threshold (-0.3×10^5 cm^{-3}) is depicted in red.

With respect to the electric field, the background values are removed using a high-pass filter, resulting then in the components $\delta \mathbf{E}_{zon}$ and $\delta \mathbf{E}_{rad}$, corresponding to the electric field fluctuation across the depletion and which direction is relative to the background electric field.

The Poynting flux derived is the one parallel to the main magnetic field,

$$\mathbf{S}_{par} = \frac{\delta \mathbf{E}_{\perp} \times \delta \mathbf{B}_{\perp}}{\mu_0} = \frac{(\delta \mathbf{E}_{rad} + \delta \mathbf{E}_{zon}) \times (\delta \mathbf{B}_{rad} + \delta \mathbf{B}_{zon})}{\mu_0}. \tag{4.1}$$

To compute the $\mathbf{S}_{par}$, the electric and magnetic field components ($\delta \mathbf{E}_{zon}$, $\delta \mathbf{B}_{rad}$ and $\delta \mathbf{E}_{rad}$, $\delta \mathbf{B}_{zon}$) must be well correlated ($|\text{cc}| \geq 0.6$). In order to strengthen the conclusions of this study, and since the set of electric field data is limited and subjected to offsets, the

$\mathbf{S}_{par}$ is computed only with one pair of $\delta\mathbf{E}_{\perp}$ and $\delta\mathbf{B}_{\perp}$ if the other pair of components is not well correlated, otherwise, both pairs are used in the computation. This approach is acceptable since the aim of this study is the analysis of the $\mathbf{S}_{par}$ direction, not its magnitude. Additionally, to avoid non-geophysical signals mainly from the electric field data, a cross-check is done to guarantee agreement between both the electric and magnetic field data. This is done by inferring the tilt of the depletion separately with $\delta\mathbf{E}_{\perp}$ and $\delta\mathbf{B}_{\perp}$, which must result in agreement to be considered in this study. The EPDs tilt can be inferred via the sign of the linear correlation between the two components of either $\delta\mathbf{E}_{\perp}$ or $\delta\mathbf{B}_{\perp}$. This cross-check is carried out only for EPDs that present well correlation between the two pairs of $\delta\mathbf{E}_{\perp}$ and $\delta\mathbf{B}_{\perp}$ components. Finally, to deduce the $\mathbf{S}_{par}$ direction, the mean is calculated over the EPD interval determined by the threshold in $\delta\mathrm{N_e}$ and highlighted with gray bands as shown in Figure 4.2. Thus, a positive value corresponds to a $\mathbf{S}_{par}$ flowing northward.

4.4 Observations and discussion

Figure 4.2 shows two passes of *Swarm* over the northern and southern magnetic hemispheres. They both present EPD events with clear electromagnetic signatures. Of great interest is the westward electric field $\delta\mathbf{E}_{zon}$ registered within the depletions in Figure 4.2a. This westward $\delta\mathbf{E}_{zon}$ measured across EPDs is associated with downward plasma convection and is commonly observed on satellites, such as the San Marco D (e.g., Laakso et al., 1994), AE-E (e.g., Singh et al., 1999), DE-2 (e.g., Palmroth et al., 2000) and C/NOFS (e.g., Burke et al., 2012; Haaser et al., 2000), and by radars (e.g., Fukao et al., 2004; Patra et al., 2014; Rao et al., 1997; Saito et al., 2008). By definition, the zonal polarization electric field within a depletion is expected to be eastward since it is built to keep the continuity of the gravity-driven current $\mathbf{j} = nM(\mathbf{g}\times\mathbf{B})/B^2$, being n and M the local plasma density and the mass of its constituent ion species, respectively. As suggested by Laakso et al. (1994), downward plasma convection associated with westward $\delta\mathbf{E}_{zon}$ across depletions can occur likely by either a change in the background electric field from eastward to westward or by responding to slow or negative vertical neutral winds when the ion-neutral collision frequency is fairly large. Based on the altitude of about 500 km at which *Swarm* records their measurements, it seems improbable to find large ion-neutral collision frequencies at heights above the F-peak. A different explanation based on measurements gathered by C/NOFS is suggested by Burke et al. (2012). The authors propose that such kind of observations corresponds to the local part of the perturbed interface that experiences the downward drift due to the westward $\delta\mathbf{E}_{zon}$ (see their Figure 12), and that in turn, they should not be considered as EPDs. However, not

having a complete picture of the depletion makes the interpretation challenging, since they can also be attributed to fossil bubbles as suggested by different authors (e.g. Aggson et al., 1992b; Krall et al., 2010, and reference therein). Standing on the observations presented in this study, it seems that the change of sign of the background electric field is the most likely cause of westward polarization electric field within EPDs, as it will be shown later in this Section.

The direction of the FACs flowing along the walls of EPDs is determined solely by the direction of $\delta\mathbf{B}_{rad}$ (see Figure 4.1). In Figure 4.3 the detected EPDs are characterized by the direction of FACs and presented for the two equinoxes and solstices. The color of the dots is related to the direction of the FACs as the ones depicted in Figure 4.1. In the bottom of each of the four panels, a histogram shows the quantity of EPD events. Each bin corresponds to 15° in geographic longitude and the color (yellow and grey) is in accordance with the color of the dots. The histograms do not present explicitly the number of EPDs, they are scaled for each panel and are shown to qualitatively highlight the longitudinal variation of the occurrence of EPDs. The data used correspond to measurements of the three *Swarm* satellites during 2014 and 2015. In general, the EPDs are well distributed along the globe and suggest a seasonal-spatial variation in agreement with previous climatological studies (e.g., Xiong et al., 2010, and reference therein). An interesting observation is the general interhemispheric flow of FACs from the local summer to winter during both June and December solstices (see Figure 4.3; c and d). Even more exciting is the sudden change in the FACs direction noticed at about $60°W$ during March and September equinoxes, and December solstice (see Figure 4.3; a,b, and c, vertical red line). This interhemispheric flow of FACs differs from the general assumption of FACs flowing poleward on western walls and equatorward on eastern walls of EPDs.

It is proposed, that a likely cause for such interhemispheric flow could be a dissimilarity in the Pedersen conductivity between both magnetic hemispheres. As it is known, the electric currents flow through all possible paths but more current will flow through the lower resistance path. Thus in a general way, it might be expected for instance, that FACs in the vicinities of the South Atlantic Anomaly where a larger Pedersen conductivity is present, tend to flow mainly into the southern magnetic hemisphere. Furthermore, summer-to-winter transequatorial winds in the thermosphere are expected to enhance conductivity in the winter hemisphere (Maruyama, 1988, Figure 7d and 8d) in agreement with the observations presented during both June and December solstices (see Figure 4.3, c and d). For the case during March and September equinoxes (see Figure 4.3, a and b), the sudden change in the

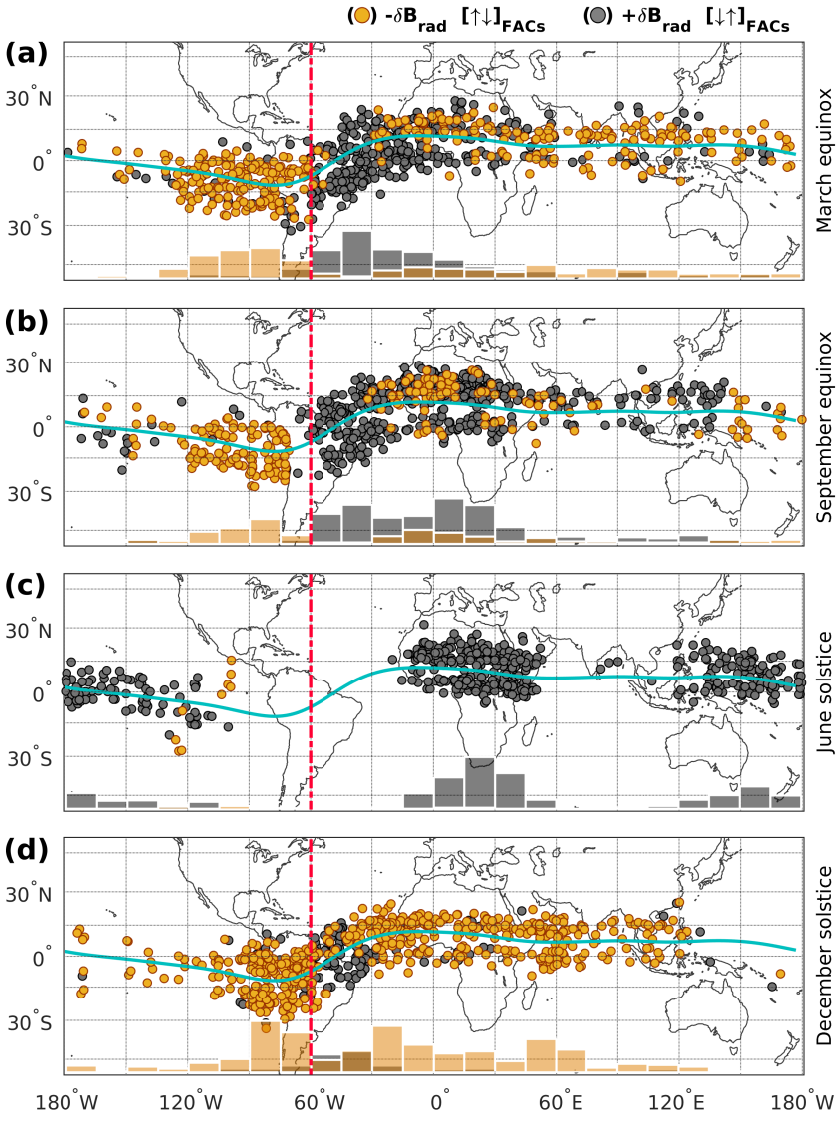

Fig. 4.3 EPD events displayed by season and set by the polarization of the FACs related magnetic signature $\delta\mathbf{B}_{rad}$ (dots). **a.** March equinox, **b.** September equinox, **c.** June solstice, and **d.** December solstice. The sudden change in the FACs direction is indicated by the dashed red line. The longitudinal variation of the occurrence of EPD events is qualitatively shown by histograms at the bottom of each panel.

FACs direction at about $60°W$, and in turn, of the Poynting flux direction is of great interest. This could be interpreted as due to the contribution of zonal winds to the field-aligned wind component in the presence of large magnetic declination angles. Generally, zonal winds in the nighttime thermosphere blow eastward, irrespective of season (e.g., Drob et al., 2015, Figure 4). When combined with the eastward tilt of the geomagnetic field between about $180°W$ and $70°W$, the eastward wind in the geographic frame can contribute to field-aligned plasma transport from the southern to the northern hemisphere. According to Maruyama (1988), the northward transport should lead to enhanced ionospheric conductivity in the northern magnetic hemisphere. Besides, when combined with the westward tilt of the geomagnetic field between about $70°W$ and $20°W$, the eastward wind can contribute to the already larger conductivity in the southern magnetic hemisphere by increasing the plasma transport from the northern to the southern hemisphere.

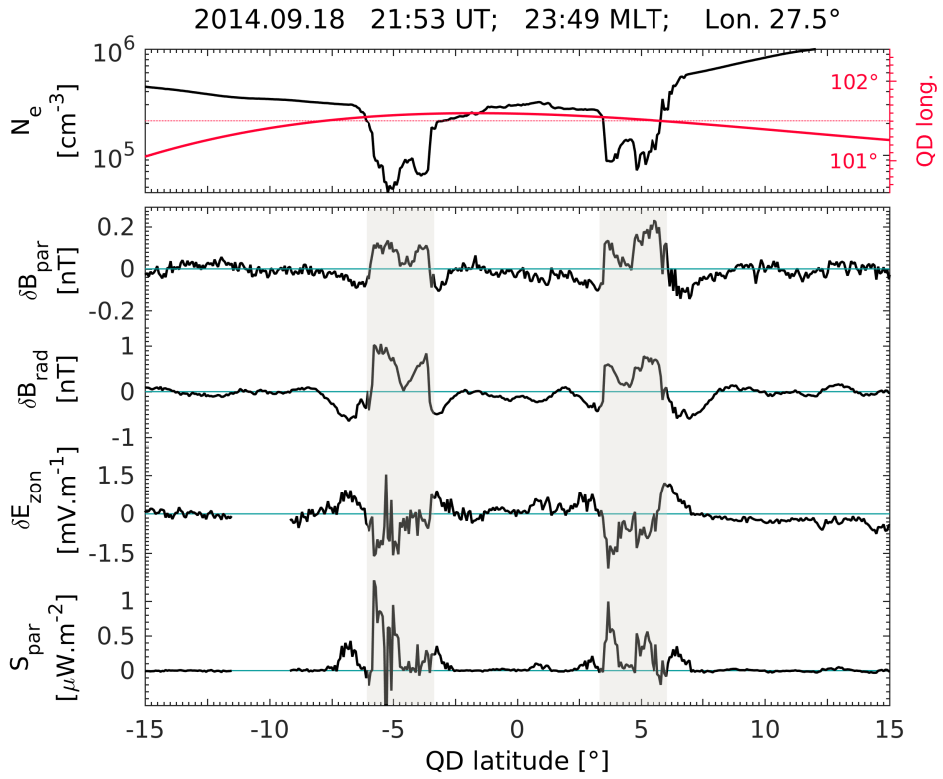

Fig. 4.4 Pass of *Swarm* Alpha. From top to bottom, the electron density (N_e) and the path of the satellite in quasi-dipole longitude (QD long.), the parallel and radial magnetic field components ($\delta\mathbf{B}_{par}, \delta\mathbf{B}_{rad}$), the zonal polarization electric field ($\delta\mathbf{E}_{zon}$) and the Poynting flux ($\mathbf{S}_{par}$).

On the direction of the Poynting flux associated with equatorial plasma depletions as derived from *Swarm*

In order to support the fact that the direction of the FACs is different than expected, Figure 4.4 shows an example of *Swarm* Alpha passing across two depletions $\pm 5^{\circ}$ away from the dip Equator. In the top of the figure (in red) the path of the satellite is depicted in quasi-dipole coordinates together with the electron density. It is noticed that both depletions are roughly in the same magnetic meridian, suggesting the possibility of being the same depleted flux tube. When looking at the $\delta \mathbf{B}_{rad}$ (third panel) both depletions present positive fluctuations, implying then an interhemispheric FACs flow. Likewise, the $\mathbf{S}_{par}$ in the bottom of the figure describes also an interhemispheric Poynting flux. Because of the relevance of these findings, a more detailed analysis on the climatology of FACs is warranted and will be addressed in another study.

In Figure 4.5 the direction of the Poynting flux is shown for some selected EPDs based on the availability of electric field data. The EPDs are displayed in two panels depending on the $\delta \mathbf{E}_{zon}$ polarization, eastward in Figure 4.5a and westward in Figure 4.5b. The direction of the FACs is also depicted with yellow and gray dots as in Figure 4.3. Since most of the $\mathbf{S}_{par}$ observations reported in this study are centered around June, a larger number of EPDs over Africa is noticed. Of the total number of events with $\mathbf{S}_{par}$ computed, 71% correspond to EPDs with eastward $\delta \mathbf{E}_{zon}$ and 29% with westward $\delta \mathbf{E}_{zon}$. In Figure 4.5c, both the EPDs in Figure 4.5 (a and b) are displayed as a function of longitude and magnetic local time. The EPDs with eastward and westward $\delta \mathbf{E}_{zon}$ are in black and color, respectively. In general, it is noticed that the EPDs between about $60^{\circ}W$ to $60^{\circ}E$ mainly occur later in the evening compared to the EPDs in other longitudes. This characteristic was also noticed by Stolle et al. (2008) using data from the CHAMP and ROCSAT-1 satellites. In the study, the authors report high agreement between the vertical plasma drift and the occurrence rate of depletions. In their Figure 6, it is shown that during June solstice the pre-reversal enhancement peak velocity occurs later in the evening between about $45^{\circ}W$ and $45^{\circ}E$, in accordance with other studies (e.g., Fejer et al., 2008, Figure 4).

In particular, it is noticed that the EPDs with westward $\delta \mathbf{E}_{zon}$ occur generally after 22:00 MLT, with the pre-midnight EPDs presenting larger amplitudes than the few post-midnight ones. However, one must be aware of the bias of this distribution by the disrupted and limited set of data. Accordingly, a more intense analysis should be carried out when even more calibrated electric field data are available from the *Swarm* mission. Additionally, westward $\delta \mathbf{E}_{zon}$ across depletions were also observed by Haaser et al. (2000) using measurements gathered by C/NOFS. The authors report depletions of this kind to occur throughout the night, and in some cases to have the same occurrence rate than depletions with eastward

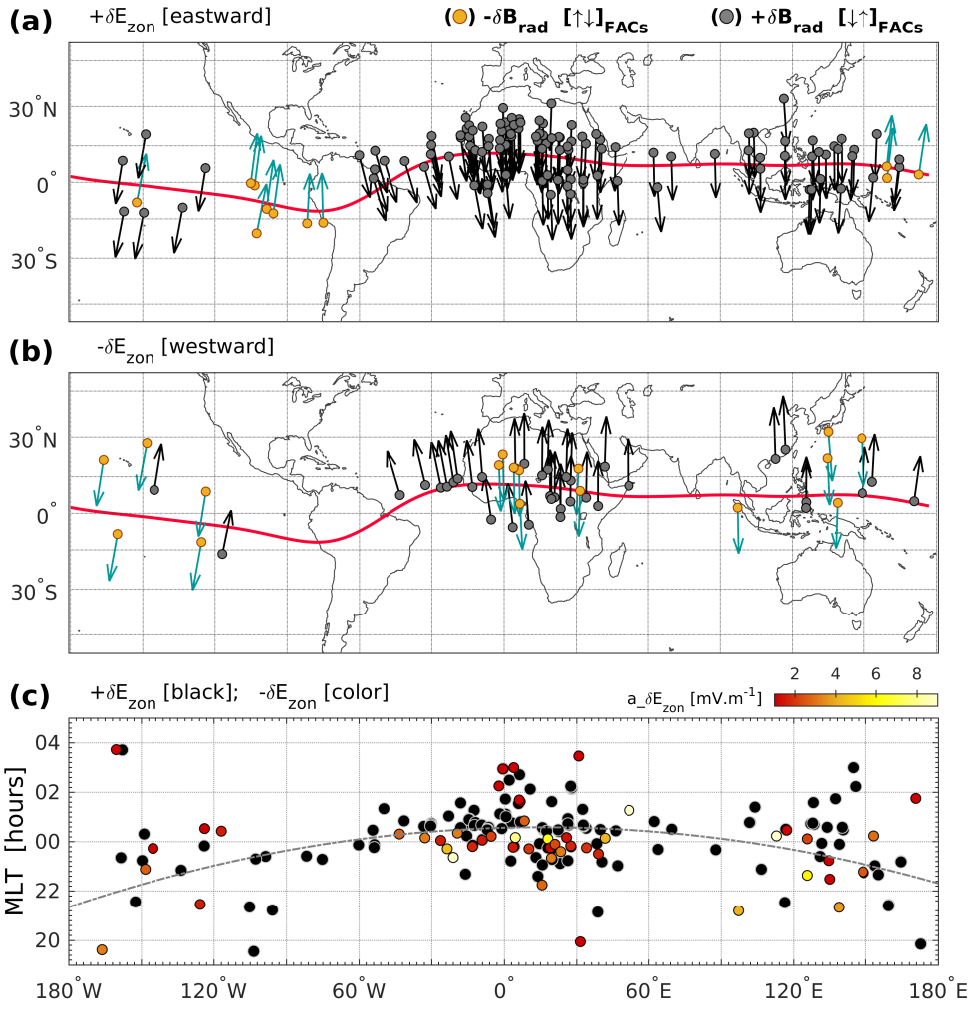

Fig. 4.5 EPDs as observed by the polarization of the FACs related magnetic signature $\delta\mathbf{B}_{rad}$ (dots) and the direction of the Poynting flux $\mathbf{S}_{par}$ (arrows). Set by, **a.** eastward polarization electric field $\delta\mathbf{E}_{zon}$, and **b.** westward polarization electric field $\delta\mathbf{E}_{zon}$. **c.** EPD events in **a.** and **b.** as a function of magnetic local time and longitude.

$\delta\mathbf{E}_{zon}$ (see their Figure 6). Therefore, it can be said that depletions with westward $\delta\mathbf{E}_{zon}$ are commonly observed throughout the night with a higher occurrence rate later in the evening (after ∼22:00 LT) when the ambient electric field has become westward.

4.5 Summary and conclusions

This study reports observations of the Poynting flux direction associated with equatorial plasma depletions as derived from the *Swarm* constellation. By using simultaneous measurements of electric and magnetic fields, the EPDs related Poynting flux is estimated for a limited set of data. Furthermore, the direction of the related FACs is derived by their associated magnetic field perturbations. The main findings and conclusions could be summarized as follows,

1. The EPDs related FACs present interhemispheric flows rather than poleward and equatorward flows at each hemisphere on the western and eastern EPD walls, respectively.

2. In turn, a general interhemispherical Poynting flux is deduced to be mainly from summer to winter during solstice [1]. During equinox, a preference for northward Poynting flux from about $110°W$ to $60°W$ (positive magnetic declination) and southward from $60°W$ to $30°E$ (negative magnetic declination) is observed.

3. The sudden change in the flow of both Poynting flux and FACs at about $60°W$ can be interpreted as the influence of thermospheric zonal winds in the presence of large magnetic declination angles. This occurs by affecting the field-aligned transport of plasma, which in consequence yields to a hemispheric asymmetry of the ionospheric conductivity. Furthermore, the South Atlantic Anomaly may also enhance ionospheric conductivity in the Southern hemisphere to the east of $60°W$.

4. Among the total number of EPDs with Poynting flux reported, 71% present eastward polarization electric field $\delta\mathbf{E}_{zon}$ and 29% westward $\delta\mathbf{E}_{zon}$ across the depletions. To support these observations, a further analysis should be carried out when more calibrated electric field data are available from the *Swarm* mission.

Certainly, an extended data set is warranted in order to investigate further spatial and temporal variations of the EPDs related electromagnetic features. Moreover, comparison

[1] Based on the data used in this study (i.e., from April to September 2014), the statement refers to June solstice only.

with simulations and ground-based measurements are essential for a better understanding of individual features of EPDs, such as the tilt, that is expected to influence the magnitude of magnetic deflections perpendicular to the ambient magnetic field.

Chapter 5

Interhemispheric field-aligned currents at the edges of equatorial plasma depletions

** This chapter is a transcript of*
Rodríguez-Zuluaga and Stolle (2019).

5.1 Introduction

Interchange instabilities operate in the post-sunset equatorial F region ionosphere due to the mutually perpendicular ambient magnetic field, zonal electric currents, and steep upward plasma density gradients. The evolution of the instabilities generates plasma irregularities in a wide range of scale sizes, from centimeters to hundreds of kilometers. This study discusses observations related to large-scale topside irregularities (few tens to hundreds of kilometers), commonly referred to as equatorial plasma depletions (EPD) or plasma bubbles. EPDs are localized field-aligned regions of depleted plasma that convect after sunset from the bottomside to the topside F region, occasionally reaching altitudes of up to 2000 km or higher. For a thorough review of EPDs and associated irregularities see Hysell (2000).

Extensive work has been done to study the nature of EPDs with airglow imager, ionosonde, global navigation satellite systems, radar, and rocket observations (see Woodman, 2009, and reference therein). Nevertheless, the study of electric currents associated with EPDs can only be carried out by using in situ magnetic field measurements gathered by low Earth-orbiting satellites, such as the AE-2 and San Marco-D (Aggson et al., 1992a), CRRES (Koons

et al., 1997), CHAMP (Lühr et al., 2002), DEMETER (Pottelette et al., 2007), and *Swarm* (Rodríguez-Zuluaga et al., 2017). Theoretical and experimental evidence has demonstrated that magnetic perturbations associated with EPDs result from pressure gradient-driven and field-aligned currents mainly (e.g., Basu, 2005; Stolle et al., 2006). By means of numerical models, the field-aligned currents (FACs) flowing at the edges of EPDs have been associated with Alfvén waves (e.g., Basu, 2005; Bhattacharyya and Burke, 2000; Dao et al., 2013) and the divergence of zonal currents (e.g., Aveiro et al., 2011; Burke, 1979; Yokoyama and Stolle, 2017)). By assuming an ideal ionosphere symmetric about the dip equator, the FACs have been described to flow anti-parallel about the dip equator, i.e., flowing poleward and equatorward at the western and eastern edges of the depletion, respectively (see Figure 2 of Burke, 1979).

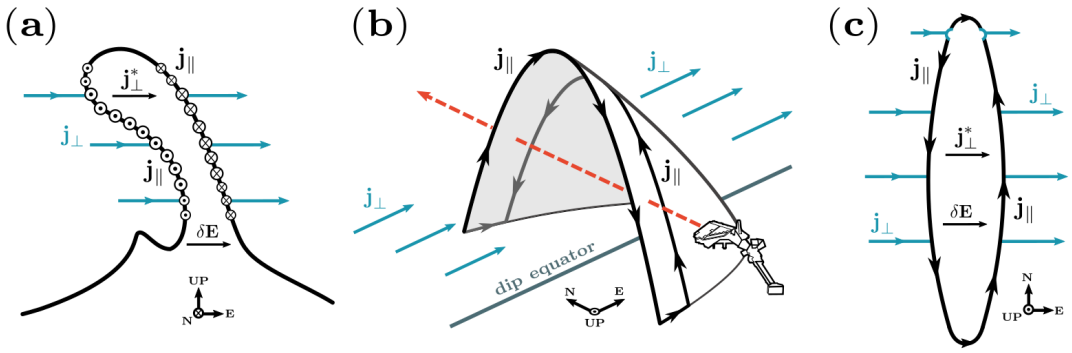

Fig. 5.1 Three views of an EPD wedge-like and its related electric currents. Field-aligned currents ($\mathbf{j}_{\parallel}$), zonal currents outside ($\mathbf{j}_{\perp}$) and inside ($\mathbf{j}^{*}_{\perp}$) the depletion, polarization electric field ($\delta\mathbf{E}$). **(a)** Vertical cut at the dip equator. **(b)** Interception with *Swarm*. **(c)** View from above. The example shows a particular case of $\mathbf{j}_{\parallel}$ closing around the southern foot of the depletion. The coordinates depicted correspond to magnetic coordinates.

Recently, Rodríguez-Zuluaga et al. (2017) investigated the direction of the EPD-related Poynting flux using simultaneous measurements of electric and magnetic field gathered by the Swarm satellite mission for a roughly 6-month period in 2014. The authors found that the orientation of the Poynting flux is interhemispheric rather than anti-parallel about the dip equator. It implies that the orientation of the FACs at the edges of EPDs is also interhemispheric. Figure 5.1 offers a schematic illustration of FACs at the edges of EPDs. It provides three different views of an EPD and its associated electric currents. They refer to a particular case in which the field-aligned currents ($\mathbf{j}_{\parallel}$) close around the southern foot of the EPD. In detail, Figure 5.1a presents a typical EPD profile at the dip equator as seen from the south. Outside the depletion, zonal currents ($\mathbf{j}_{\perp}$) are mainly the sum of gravity-driven,

Pedersen and inertial currents. Inside the depletion, zonal currents $(\mathbf{j}_{\perp}^{*})$ build up to maintain the current continuity through Pedersen and gravity-driven currents. Figure 5.1b depicts an EPD as a wedge-like structure. This representation can be pictured by mapping the EPD in Figure 5.1a to conjugate locations in the northern and southern hemispheres. Figure 5.1c shows the depletion from above. Following back the work by Rodríguez-Zuluaga et al. (2017), the authors suggest that asymmetry in ionospheric conductivity between both magnetic hemispheres might play a significant role in determining the flow direction of the currents. By using measurements gathered by the C/NOFS satellite mission, Burke et al. (2012) also suggest an interhemispheric current configuration where only one magnetic hemisphere gets disturbed at the bottom side, implying a single Alfvénic disturbance. The idea of an off-equator EPD has been supported using a three-dimensional numerical simulation with electromagnetic features that showed electric fields at the dip equator remotely mapped via Alfvén waves Dao et al. (2013).

In this paper, we make use of an extended dataset of the magnetic field and electron density observations from the *Swarm* mission to provide a comprehensive analysis of the spatial and temporal variability of the flow configuration of EPD-related FACs. In comparison with climatological predictions of the background ionosphere, we assess the role of the ionospheric conductivity in determining the observed direction of FACs.

5.2 Dataset and methods

The *Swarm* constellation mission (Friis-Christensen et al., 2006; Olsen et al., 2013) was successfully launched into a near-polar, circular orbit on 22 November 2013. The mission consists of three identical satellites, *Swarm* Alpha, Bravo and Charlie, of which two (Alpha and Charlie) currently fly side-by-side at an altitude of about 450 km separated by 1.4° in longitude at the equator. The third satellite (Bravo) orbits at a higher altitude of roughly 510 km. Consecutive orbits of each satellite are separated by approximately 20° in longitude with a local time precession of about 10.8 min/day for Alpha and Charlie and about 10.2 min/day for Bravo, resulting in a complete local time coverage after five years. The magnetic and plasma measurements and their related payloads on board *Swarm* are comprehensively described in Tøffner-Clausen et al. (2016) and Knudsen et al. (2017), respectively. In this study, we use observations of the magnetic field and electron density (N_e) at a rate of 1 Hz. Thus, the N_e is decimated from its regular sampling rate of 2 Hz to 1 Hz to match the rate of

the magnetic measurements. The study period includes continuous observations of the two parameters from 1 December 2013 to 30 April 2018.

The following statistical analysis is based on a set of EPDs detected by a method similar to the one described in Rodríguez-Zuluaga et al. (2017). Briefly, the background electron density (N_0) is obtained through a low-pass filter. The procedure is performed over individual passes of *Swarm* limited to $\pm 30^\circ$ quasi-dipole latitude and 18-05 magnetic local time (MLT). Then, a preliminary detection results from the residual $\delta N_e = N_e - N_0$. At this point, only depletions are identified as EPDs if the percent change between the background and residual ($\delta N_e / N_0$) is higher than 20%, over a minimum distance of about 23 km (3 s of satellite flight). In this way, we account for decreasing N_0 along the study period due to the currently declining solar cycle. Finally, for the EPDs to enter into the statistics, they must present distinct magnetic signatures related to FACs. In this respect, we calculate residuals of the magnetic field measurements to a high precision empirical model of the core, crustal and magnetospheric field (Finlay et al., 2016) and rotate the components into a magnetic-field-aligned coordinate system using the International Geomagnetic Reference Field (IGRF) (Thébault et al., 2015). In this frame, $\delta \mathbf{B_{par}}$ points northward along the mean ambient magnetic field, $\delta \mathbf{B_{zon}}$ is perpendicularly eastward to the magnetic meridian and $\delta \mathbf{B_{rad}}$ completes the triad pointing vertically outward. Since the EPDs-related FACs have associated only transverse magnetic perturbations, their flow direction is deduced solely by $\delta \mathbf{B_{rad}}$. Thus, for each EPD detected, both $\delta \mathbf{N_e}$ and $\delta \mathbf{B_{rad}}$ across the depletion must present a correlation coefficient (cc) with absolute values larger or equal than 0.6 ($|\mathrm{cc}| \geq 0.6$). This approach guarantees that the considered EPDs have comparable sheets of field-aligned currents flowing in opposite directions at their western and eastern edges. The direction of the FACs is then determined by the sign of (cc) such that for negative values, $\delta \mathbf{B_{rad}}$ is positive and the FACs flow anti-clockwise along the edges of the depleted structure. If (cc) is positive, $\delta \mathbf{B_{rad}}$ is negative, and the FACs flow clockwise. Samples for these two cases are provided in Figure 5.2 and explained later on.

5.3 Results and discussion

Figure 5.2 presents two passes of *Swarm*, each showing N_e and $\delta \mathbf{B_{rad}}$ as a function of quasi-dipole latitude, magnetic local time and altitude. The two examples reflect typical observations of postsunset EPDs as detected by *Swarm* (Rodríguez-Zuluaga et al., 2017). Since EPDs evolve in time to describe a band-shell wedge-like (Kil et al., 2009) polar-orbiting satellites such as *Swarm* intersect an EPD in both magnetic hemispheres while observing the

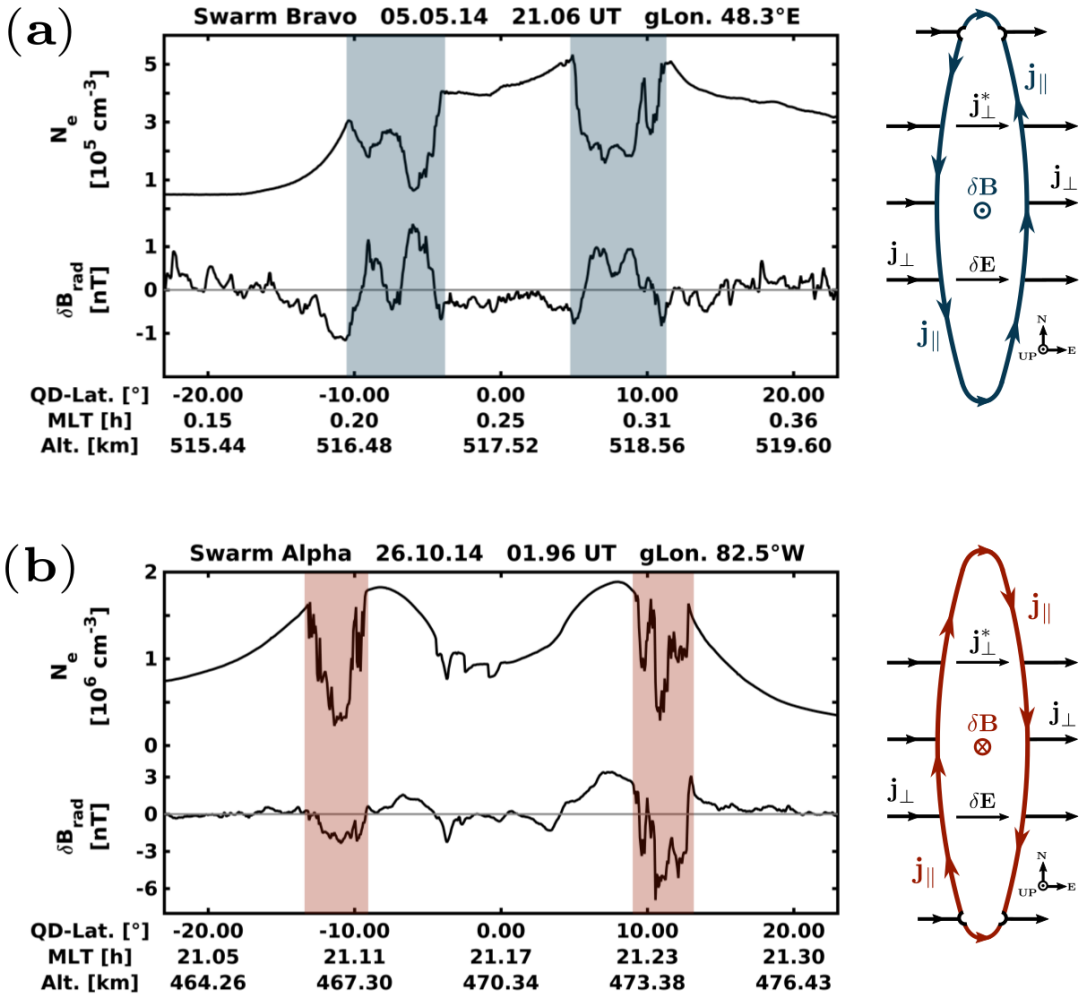

Fig. 5.2 Two passes of *Swarm* showing two different configurations of interhemispheric FACs. Each panel from top to bottom presents electron density (N_e) and radial magnetic field component $\delta\mathbf{B_{rad}}$. To the right, sketch of an EPD see from above describing the corresponding configuration of FACs.

background ionosphere in between (see Figure 5.1b). In each of the two panels, the EPDs present negative (-0.91 and -0.82) and positive (+0.84 and +0.82) correlation coefficients between $\delta\mathbf{N_e}$ and $\delta\mathbf{B_{rad}}$, respectively. Since the MLT is not changing considerably along the satellite pass, it is likely that the depletions at each magnetic hemisphere correspond to the same depleted wedge or flux tube. To the right of each panel, a sketch of an EPD seen from above depicts the corresponding configuration of currents. It describes an EPD moving upward with respect to the background plasma, as suggested by the depicted eastward polarization electric field ($\delta\mathbf{E}$). Outside the depletion the zonal currents ($\mathbf{j}_\perp$) are the sum of gravity-driven, Pedersen and inertial currents mainly. These different current sources vary with altitude, such as the first is more dominant at the peak of the F region, and the other two at the bottom side and topside, respectively. The field-aligned currents ($\mathbf{j}_\parallel$) close anticlockwise around the southern foot (Figure 5.2a) or clockwise around the northern foot (Figure 5.2b) of the EPD. In each case, at lower altitudes, a small part of the currents must divert around the conjugate foot to maintain the continuity of the current. Finally, both sketches show the perturbed magnetic field $\delta\mathbf{B_{rad}}$ associated with $\mathbf{j}_\parallel$.

To distinguished between the two configuration of currents throughout the paper, hereafter, the FACs are also refer to as blue and red FACs, corresponding to EPDs with a current system as the one shown in Figure 5.2a and Figure 5.2b, respectively.

5.3.1 Spatial characteristics

Figure 5.3 shows the spatial distribution of EPDs as detected by the three *Swarm* satellites from December 2013 to April 2018. The contour plots represent the occurrence rate within a grid of $10^\circ \times 5^\circ$ in longitude and latitude. The results are further distinguished by the direction of the FACs (left and right panels), and season i.e. March equinox (February, March, and April), June solstice (May, June, and July), September equinox (August, September, and October) and December solstice (November, December, and January). In general, EPDs with FACs closing southward (in blue) occur more frequently than those closing northward (in red).

The longitudinal distribution of EPDs shows a distinct pattern among the different seasons already known from earlier studies. Concerning the FACs direction, the two equinoxes display similar patterns for each current configuration. The blue FACs present a maximum occurrence at about 40°W that decreases toward the African sector. For the red FACs, the occurrence maximizes over the Pacific at about 90°W and over Africa at about 0° longitudes. The red FACs do not overlap with the blue FACs over the American sector but do overlap

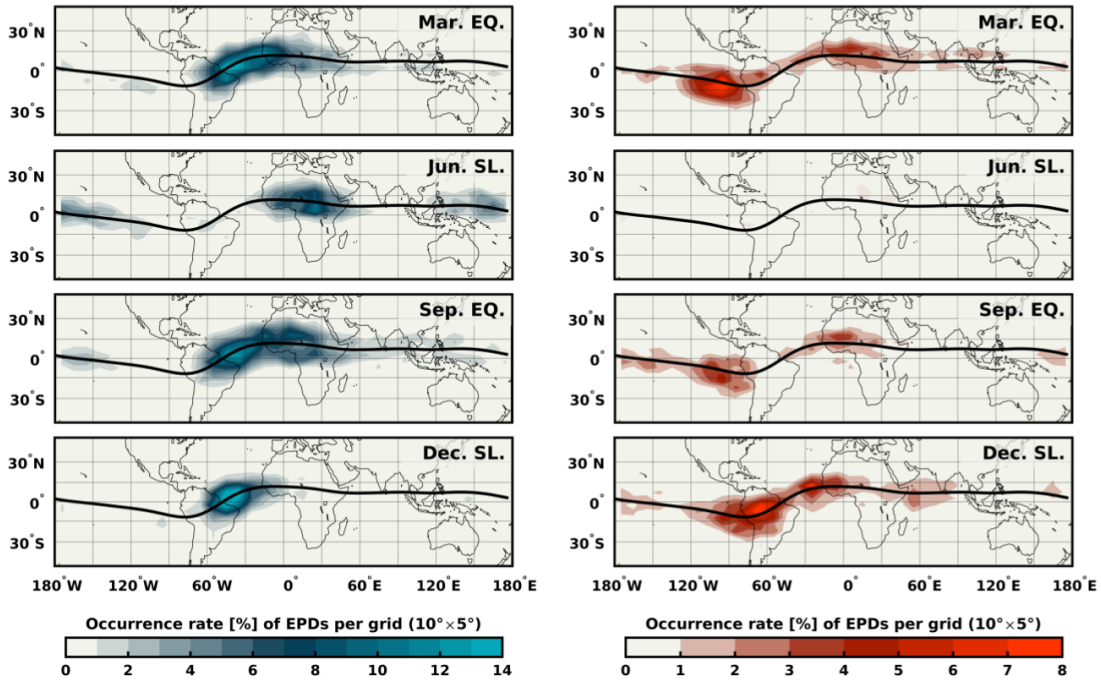

Fig. 5.3 Global and seasonal distribution of EPDs as characterized by their related FACs orientation. Left: EPDs with FACs closing southward (Blue). Right: EPDs with FACs closing northward (Red). Black solid lines indicate the location of the dip equator.

over the African continent. On the contrary, for the two solstice periods, the FACs present very different patterns. Interestingly, during June solstice all of the EPDs present blue FACs. Differently, December solstice exhibits EPDs with red FACs peaking at about 70°W and 30°W. EPDs with blue FACs instead, maximize around 40°W where the red FACs show a local minimum.

5.3.2 Temporal characteristics

Besides their particular spatial allocation, the EPDs-related FACs also present a longitudinal dependent local time distribution. Figure 5.4 shows EPDs divided by their related FACs direction as a function of season, magnetic local time (MLT) and longitude. The contours represent the occurrence rate of EPDs within a grid of $10^\circ \times 1$h in longitude and MLT. EPDs with blue FACs appear to be persistent throughout the night between 20 and 04 MLT during both equinoxes and December solstice seasons. In June solstice, the EPDs are mainly pre-midnight and decay until 02 MLT. The EPDs with red FACs present a preference for pre-midnight hours, however, there is a lower number of post-midnight EPDs over the

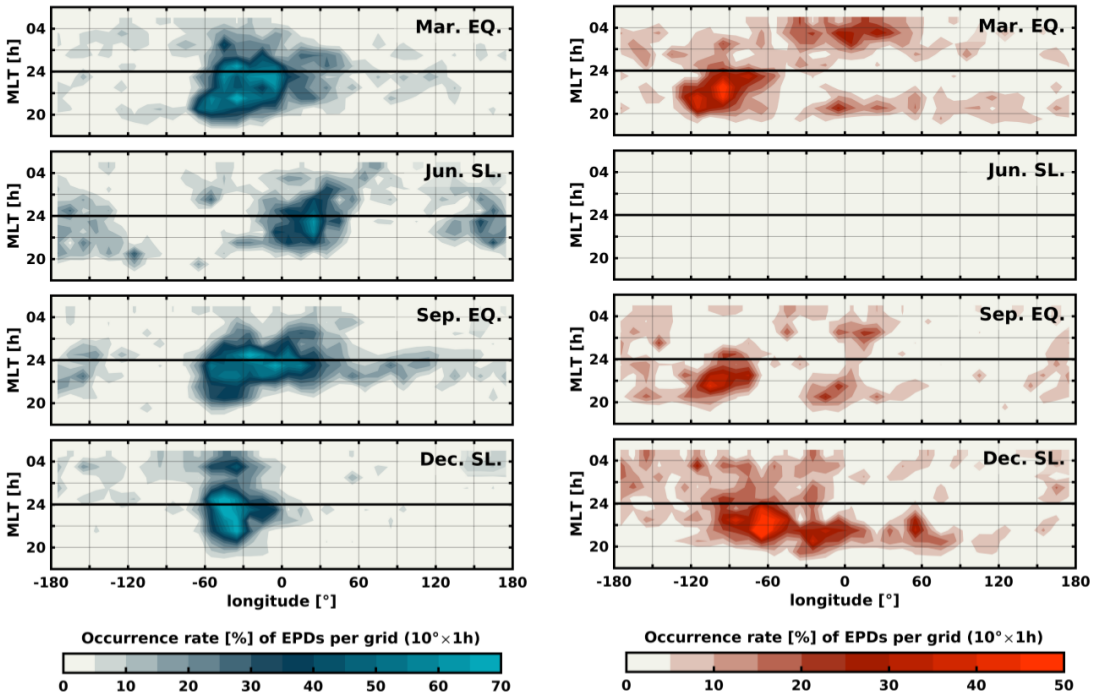

Fig. 5.4 EPDs by season characterized by their related FACs orientation as a function of longitude and magnetic local time. Left: EPDs with FACs closing southward. Right: EPDs with FACs closing northward.

Atlantic/African sector during equinoctial months. It is interesting to notice that EPDs between about 30°W and 0° present FACs that tend to change direction twice. Before 22 MLT the FACs close northward (red FACs), then they switch to close southward (blue FACs) until 02 MLT when they turn northward again.

5.3.3 Role of the Pedersen conductance

Previously in this paper, it was mentioned that both the divergence of zonal currents and Alfvén waves are associated with the field-aligned currents at the edges of plasma depletions. Although it implies that the nature of EPDs is a hybrid between electrostatic and electromagnetic modes, it is acceptable to assume that EPDs are predominantly electrostatic in nature (e.g., Basu, 2005; Dao et al., 2013). For the waves, the propagation of the disturbance must be in the direction of the fastest phase velocity i.e., from low to high plasma density. In other words, the waves would propagate towards the hemisphere with the lowest resistivity, reaching an electrostatic state after a few seconds (Dao et al., 2013). For the zonal currents,

the hemisphere with the highest horizontal conductivity (mainly Pedersen) is where the currents will diverge.

To assess the effect of the conductivity in the preference of the FACs to close around the southern or northern foot of a depletion, we compute the height-integrated Pedersen conductivity (Σ_P) as,

$$\Sigma_P = \int_{h_1}^{h_2} \sigma_P \, dh, \tag{5.1}$$

integrating from h_1 to h_2 (80 km and 300 km of altitude, respectively). σ_P is the Pedersen conductivity as given by the conventional formula,

$$\sigma_P = \frac{eN_e}{B}\left[\frac{\omega_e \upsilon_{en}}{\omega_e^2 + \upsilon_{en}^2} + \frac{\omega_i \upsilon_{in}}{\omega_i^2 + \upsilon_{in}^2}\right] \tag{5.2}$$

where the subscripts n, e, and i represent neutral, electron and ion, respectively. ω is the gyrofrequency, υ the collision frequency and e the electron charge. Here we use the three most abundant ion species along the altitude of integration, i.e., atomic oxygen (O^+), nitric oxygen (NO^+) and molecular oxygen (O_2^+). The neutral species considered are also the most abundant in that height range, i.e., O_2, O, and N_2. The collision frequencies υ_{en} and υ_{in} are calculated as in Schunk and Nagy (2009). The magnetic field is obtained from the IGRF model, the temperatures and densities of the neutrals from the NRLMSISE-00 model (Picone et al., 2002) and of the electrons and ions from the IRI model (Bilitza et al., 2017).

Figure 5.5 shows global maps of Σ_P for one typical day of each season at 22 LT i.e. 21st March, June, September and December of 2015, respectively. In the two equinoctial seasons, the conductance shows similar distributions with larger values at the South Atlantic geomagnetic anomaly (SAA), where the background geomagnetic field intensity drops to about 20.000 nT (compared to about 30.000 nT over the Pacific). At June solstice season, the conductance maximizes in the southern magnetic hemisphere at all longitudes. Conversely, the conductance is more significant in the northern magnetic hemisphere during the December solstice season. Such a distinct feature in the conductance distribution during solstice periods is likely the effect of meridional thermospheric winds blowing from local summer to winter (e.g., Rishbeth et al., 2000). Explicitly, the winds transport the plasma along the field lines pushing the ionosphere upward in the summer hemisphere and downward in the winter

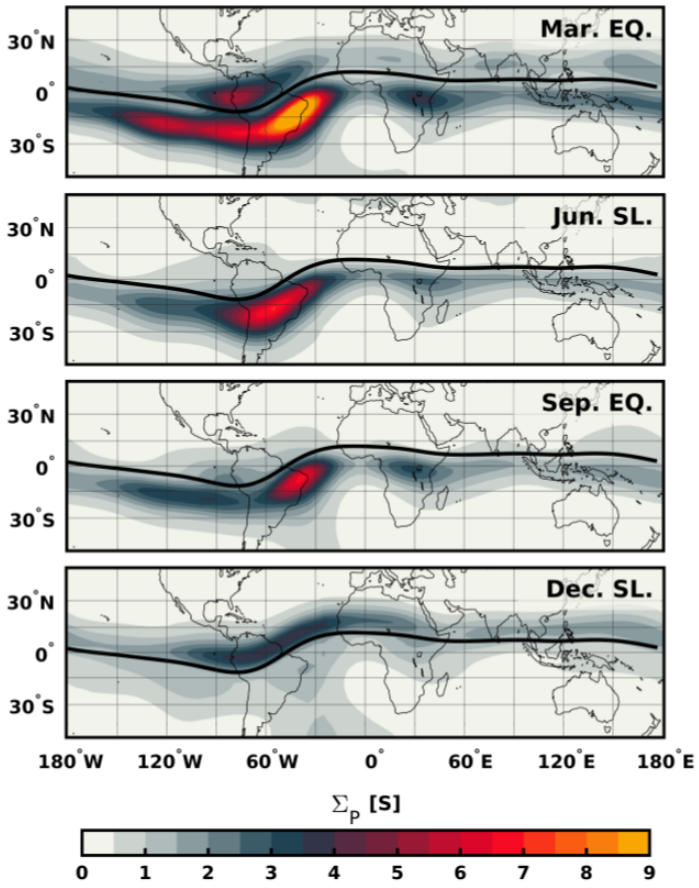

Fig. 5.5 Global maps of the Pedersen conductance derived from IRI and NRLMSISE-00 models for one representative day per season. The integrated altitude ranges from 80 to 300 km. The local time corresponds to 22 hours. Black solid lines indicate the location of the dip equator.

hemisphere. Since the relation between the ion-neutral collision frequency and the ion gyrofrequency increases with decreasing altitude, the conductivity turns out to be higher in the winter hemisphere (e.g., Krall et al., 2009; Maruyama, 1988).

By comparing Figure 5.5 with Figure 5.3, we find good agreement between the hemispherical asymmetry of Σ_P and the direction to which the FACs close. (1) In both equinoctial seasons, the majority of EPDs detected over the Atlantic ($60°\text{W} - 0°$) present FACs closing to the southern magnetic hemisphere where Σ_P is most significant, e.g., collocated with the SAA. (2) In June solstice, all the identified EPDs exhibit FACs closing southward where Σ_P is the highest at all longitudes. (3) During December solstice, Σ_P is higher in the northern than in the southern magnetic hemisphere, so most of the EPDs present FACs closing northward,

except over the SAA where the FACs close southward. Nevertheless, there are other regions where the agreement between the hemispherical distribution of Σ_P and the orientation of the FACs is less evident. In the two equinoctial seasons, the FACs close northward around 90°W though Σ_P does not appear to dominate in the northern magnetic hemisphere at that longitude. We suggest that this might be an effect of zonal thermospheric winds that cannot properly be accounted for through empirical models. During nighttime, eastward winds contribute to the field-aligned transport of plasma in regions with significant magnetic declination. Around the dip equator, the magnetic declination turns positive to the west of 75°W allowing the winds to push down the ionosphere and increase the conductivity in the northern magnetic hemisphere. Another challenging region also in equinox is the one around 0° of longitude. Figure 5.4 shows that around this longitude the orientation of the FACs switches direction twice, at 22 and 02 MLT. By looking in detail at the variability of Σ_P during those specific local times (not shown), no change is noticed that can explain such behavior, perhaps because of the temporal-scale of the variations which empirical models cannot adequately capture.

5.4 Summary and conclusions

In this study, we use simultaneous measurements of the magnetic field and electron density from the *Swarm* mission to assess the spatial and temporal characteristics of the field-aligned currents associated with equatorial plasma depletions. Based on the results reported by Rodríguez-Zuluaga et al. (2017) about the interhemispheric preference of the Poynting flux related to EPDs, two configurations of FACs are possible (see Figure 5.2). In general, the FACs are suggested to close around the southern or northern foot of an EPD at the magnetic hemisphere with the highest conductivity. To investigate where, when and which of the two configurations of FACs dominates, we use a continuous dataset starting from December 2013 until April 2018. To evaluate under what conditions one of the two configurations prevails, we compute the Pedersen conductance using empirical models. The main findings and conclusions are summarized as follows.

1. The EPDs-related FACs present a distinct longitudinal pattern among the different seasons. During both equinoxes, the occurrence of EPDs with FACs closing to the southern magnetic hemisphere maximizes about 40°W and decreases toward the African sector. The occurrence of FACs closing northward shows maxima at about 90°W and 0°. Distinctly, the solstice seasons presents contrasting patterns. On June solstice all the EPDs present FACs closing to the southern magnetic hemisphere.

During December solstice, the FACs close northward at about 70°W and 30°W mainly and southward at about 40°W where the occurrence of FACs closing northward presents a minimum.

2. The orientation of the FACs exhibits an apparent longitudinal dependent local time distribution. Generally, the EPDs with FACs closing around their southern foot persist throughout the night, while the FACs closing northward present a preference for pre-midnight hours except over the Atlantic/African sector where few of them occur after midnight. An interesting feature is noticed during equinox periods where the EPDs between about 30°W and 0° show FACs switching orientation twice. Before 22 MLT the FACs close northward, then they change southward until 02 MLT when they turn back northward.

3. The Pedersen conductance presents similar spatial distribution in the two equinoxes and opposite in the solstices (see Figure 5.5). By comparing with the orientation of the FACs, we found good agreement between the hemispherical asymmetry of Σ_P and the direction to which the FACs close. During both equinoctial periods, the majority of the EPDs detected between about 60°W and 0° exhibit FACs closing southward where Σ_P is more significant (collocated with the SAA). In June solstice, all the EPDs present FACs closing at the southern magnetic hemisphere where Σ_P is the highest at all longitudes. In December solstice, Σ_P maximizes in the northern magnetic hemisphere where most of the FACs close, except over the SAA where the FACs close southward.

4. There are some other regions where the agreement between the distribution of Σ_P and the direction of the FACs is less evident, especially at about 90°W during both equinoctial periods. In such region, the FACs close mostly northward though Σ_P is not more significant than in the southern hemisphere. This observation might be explained by an effect of zonal thermospheric winds that cannot be adequately detected by empirical models.

The interhemispheric FACs reported in this study suggest an electrostatic regime highly determined by a hemispherical asymmetry of the ionospheric conductivity. The FACs are presumed to close at lower ionospheric altitudes through Pedersen currents in the magnetic hemisphere with the highest conductivity. A detailed investigation is appropriate based on numerical simulations with both electrostatic and electromagnetic characteristics under hemispherical asymmetries of different parameters (e.g., conductivity, plasma density, magnetic field).

Chapter 6

On the balance between plasma and magnetic pressure across equatorial plasma depletions

* *This chapter is a transcript of*
Rodríguez-Zuluaga et al. (2019).

6.1 Introduction

In the Earth's low-latitude ionosphere, large-scale electric currents develop during daytime at the E- and F-region through dynamo processes (e.g., Forbes and Garrett, 1979; Rishbeth, 2000). Different than these currents, other currents do not depend on conductivity but upon the interaction of the plasma with the Earth's gravitational and magnetic fields. This characteristic makes currents such as those driven by gravity and by plasma pressure gradients relevant in the nighttime ionosphere (e.g., Alken et al., 2017). The latter, also known as diamagnetic currents ($\mathbf{j_d}$) are essential to understanding the balance between magnetic and plasma pressure. Although these currents have not been extensively studied, the known theoretical and experimental evidence provides valuable information. Lühr et al. (2002) reported the first magnetic field observations related to $\mathbf{j_d}$ at the equatorial ionospheric anomaly (EIA). The EIA presents significant meridional gradients of plasma pressure due to its regular plasma density enhancements at 10° to 15° south and north to the dip equator. The authors use magnetic field measurements gathered by the CHAMP satellite to validate the expected magnetic effect associated with $\mathbf{j_d}$. Further studies have shown evidence that

suggests there is a good balance between magnetic and plasma pressures (e.g., Park et al., 2008b; Stolle et al., 2006), especially when the neutral gas is taken into account (e.g., Park et al., 2016). In particular, Stolle et al. (2006) analyze magnetic field fluctuations associated with equatorial plasma depletions (EPD) and their global distribution by using CHAMP data. In their study, the authors present distinct magnetic fluctuations related to $\mathbf{j_d}$ at EPDs. In the absence of high-resolution electron density measurements, they use such magnetic signatures to assess the global occurrence rate of EPDs, finding good agreement with previous studies based on plasma density measurements. By using numerical simulations, additional studies have also obtained magnetic field fluctuations related to $\mathbf{j_d}$ at EPDs with magnitudes similar to those detected by magnetometers onboard satellites (e.g., Aveiro et al., 2011; Dao et al., 2013; Yokoyama and Stolle, 2017). The EPDs correspond to the large-scale structure (few tens to hundreds of kilometers) of topside Spread-F. They are characterized by steep plasma density gradients that strongly affect radio wave propagation, causing outages and degradation of satellite signals (see, Woodman, 1960).

In this study, we concentrate on the balance between magnetic and plasma pressure across strong plasma density gradients in the equatorial ionosphere. Specifically, we analyze EPDs using simultaneous measurements of the magnetic field and electron density from the ESA's Swarm constellation mission. Apart from a spatial and temporal assessment of about five years of events, this paper presents the first observational evidence of high plasma pressure in regions of reduced plasma density in the ionosphere.

6.2 Background

Equatorial plasma depletions (EPDs) occur in the post-sunset ionosphere as depleted wedge-like structures or depleted flux tubes aligned with the ambient magnetic field (see Figure 6.1a). The EPDs are believed to extend in latitude between magnetic conjugate points in the northern and southern hemispheres and altitude from the bottom side F-region up to about 2000 km (see, Hysell and Kudeki, 2004). The EPD-related current system comprises ambipolar, diamagnetic and field-aligned currents closing through zonal currents (e.g., Aveiro et al., 2011; Bhattacharyya and Burke, 2000; Dao et al., 2013). Both field-aligned and diamagnetic currents are regularly detected by high-precision magnetometers onboard LEO satellites such as CHAMP and Swarm (e.g., Lühr et al., 2003; Rodríguez-Zuluaga et al., 2017; Stolle et al., 2006).

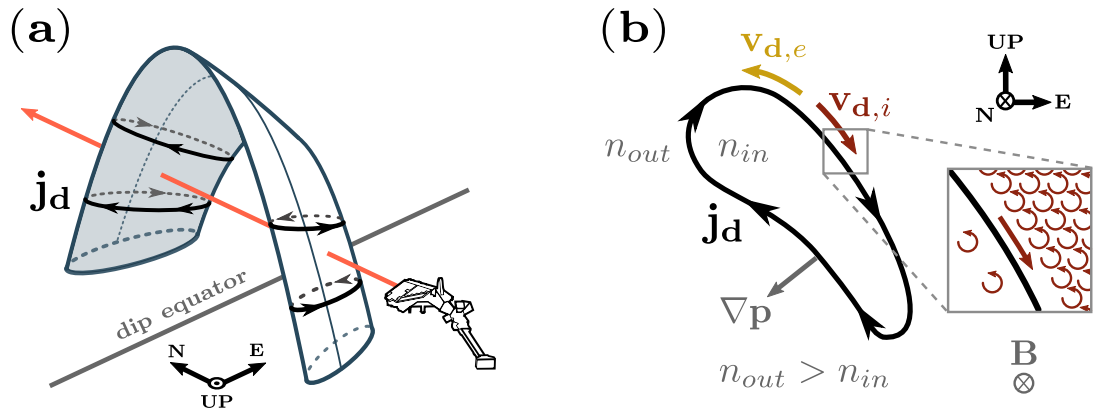

Fig. 6.1 (a) Description of a wedge-like EPD, its associated diamagnetic current ($\mathbf{j_d}$) and the path of a Swarm satellite going through the EPD. (b) A zonal-cross section at the dip equator of the EPD in (a). It shows both the diamagnetic drifts of ions and electrons ($\mathbf{V_{d,i}}$,$\mathbf{V_{d,e}}$), the plasma pressure gradient (∇p) and the diamagnetic current ($\mathbf{j_d}$). The box to the right is a zoom in to the ions gyrating in the magnetic field at the edge of the EPD.

In the ionosphere, as in all magnetized plasmas, there is a drift exclusively related to plasma pressure gradients. This drift is commonly referred to as diamagnetic drift ($\mathbf{V_d}$) and is perpendicular to both the ambient magnetic field and the plasma pressure gradient, as described by

$$\mathbf{V_{d},}_j = -\frac{\nabla p_j \times \mathbf{B}}{q_j n_j B^2}. \tag{6.1}$$

where $p_j = n_j k T_j$ is the partial plasma pressure, n is the number density, k is the Boltzmann constant, T is the temperature, $\mathbf{B}$ is the ambient magnetic field and q is the charge of the particle. The subscript j refers to either electrons e or ions i. Figure 6.1a shows a wedge-like EPD and a Swarm satellite crossing through. Figure 6.1b depicts a zonal-cross section at the dip equator of the EPD in Figure 6.1a, as seen from the southern hemisphere. The box on the right shows a zoom in to the ions gyrating in the magnetic field. This particular example considers an isothermal condition, meaning the gyration radii of the particles inside and outside the EPD are the same. As illustrated in the diagram, the higher density region rules the direction of the total net drift at the edges of the EPD.

Since electrons and ions drift in opposite directions, as denoted by q in equation (1), a current $\mathbf{j_d}$ is built up as shown in Figures 6.1a and 6.1b (thick black lines) and described by

$$\mathbf{j_d} = q_e(n_i\mathbf{V_{d},}_i - n_e\mathbf{V_{d},}_e) = -\frac{\nabla p \times \mathbf{B}}{B^2}; \quad p = p_i + p_e. \tag{6.2}$$

The current $\mathbf{j_d}$ is generally known as diamagnetic current since its associated magnetic field opposes the ambient magnetic field in the region where the plasma pressure enhances. Since $\mathbf{j_d}$ is perpendicular to both $\mathbf{B}$ and ∇p, its related magnetic perturbation is parallel to the ambient field ($\delta\mathbf{B}_{\parallel}$, positive northward). A relation for such magnetic effect is described by Lühr et al. (2002) for a steady-state plasma as,

$$\delta\mathbf{B}_{\parallel} = -\delta n_e k(T_e + T_i)\frac{\mu_0}{B}. \tag{6.3}$$

Here, μ_0 is the permeability of free space, and δn_e is the difference between the electron density outside and inside the EPD ($\delta n_e = n_{out} - n_{in}$). The negative sign indicates the decrease of the ambient magnetic field when the plasma pressure increases. In this relation, the balance between magnetic and plasma pressure occurs under isothermal conditions and when the plasma pressure gradient is positive (pointing outside the EPD). The neglect of the magnetic tension due to the curvature of the magnetic field lines is justified for structures much smaller than the bending radius of the ambient field lines.

6.3 Observations

The Swarm mission consists of three satellites (Alpha, Charlie, and Bravo) flying in near-polar circular orbits. The first two satellites fly side-by-side at an altitude of about 450 km separated by 1.4° in longitude at the equator, while Bravo orbits at a higher elevation of about 510 km. This study uses Swarm magnetic field and electron density measurements at a rate of 1 Hz and 2 Hz, respectively. The latter are decimated to 1 Hz to match the former. A detailed description of the payloads on board Swarm is given by Knudsen et al. (2017) and Tøffner-Clausen et al. (2016).

The method for detection of EPDs is described by Rodríguez-Zuluaga et al. (2017). To assess the balance between the plasma and magnetic pressure, we only consider EPDs with a good linear correlation between $\delta\mathbf{B}_{\parallel}$ and δn_e. That is, the absolute value of the correlation coefficients ($|cc|$) must be greater than or equal to 0.6. Figure 6.2 presents two typical cases of detected EPDs. In the first case (top-left panel), a pass of Swarm Charlie shows EPDs with $\delta\mathbf{B}_{\parallel}$ in anti-phase with δn_e. In the second case (bottom-left panel), a crossing of Swarm Alpha shows EPDs with $\delta\mathbf{B}_{\parallel}$ in-phase with δn_e. From the sign of $\delta\mathbf{B}_{\parallel}$ (positive in the

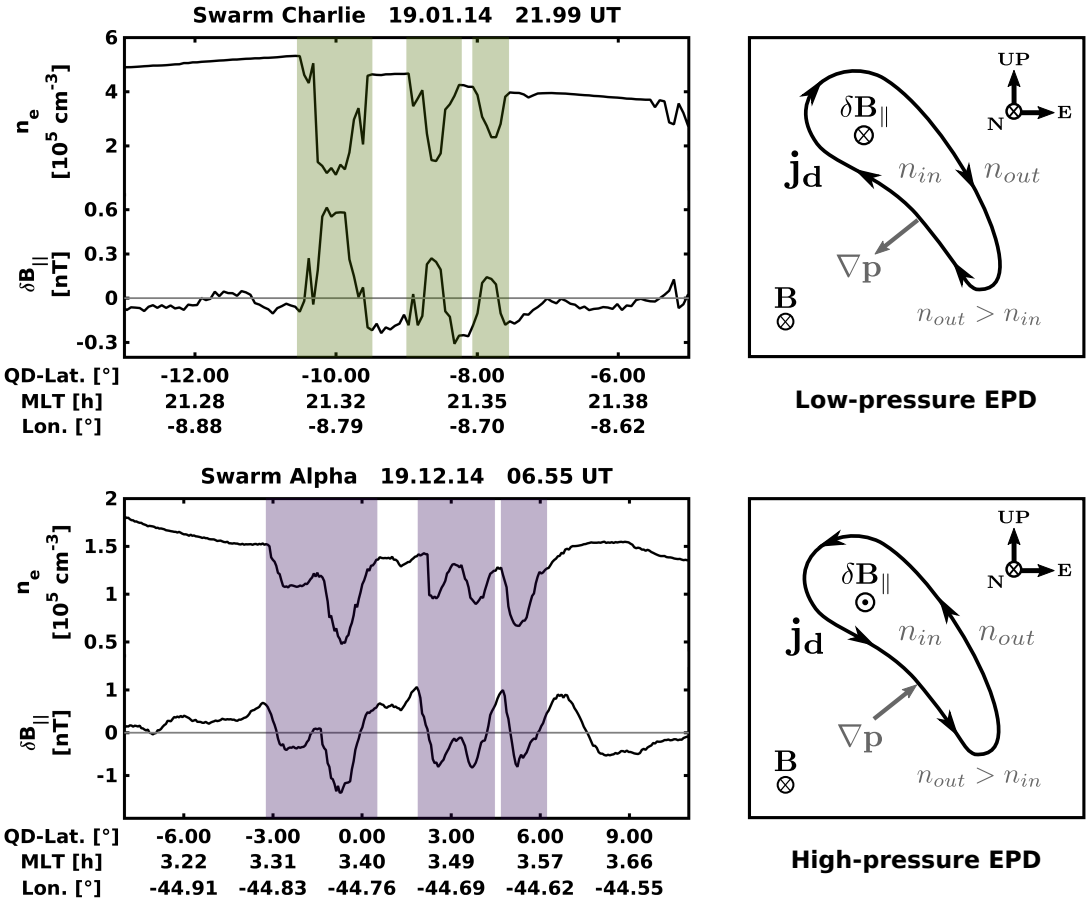

Fig. 6.2 (Left) Passes of Swarm Charlie (top) and Alpha (bottom) at equatorial latitudes showing electron density n_e and $\delta \mathbf{B}_{||}$ as a function of quasi-dipole latitude, magnetic local time and longitude. (Right) Diagrams describe the plasma pressure gradient ∇p, the current $\mathbf{j_d}$ and its related magnetic field $\delta \mathbf{B}_{||}$ for each observation.

direction of **B**), we can infer the orientation of both $\mathbf{j_d}$ and ∇p as equation (2) suggests. The two current and pressure configurations are depicted on the right panels of Figure 6.2 using the diagram described in Figure 6.1b. For the EPDs on the left-top panel, the graph on the right-top shows a positive $\delta\mathbf{B}_{\parallel}$ related to a clockwise $\mathbf{j_d}$ and a positive ∇p (pointing outside the EPD). For the EPDs on the left-bottom panel, the graph on the right-bottom shows a negative $\delta\mathbf{B}_{\parallel}$ related to an anti-clockwise $\mathbf{j_d}$ and a negative ∇p (pointing inside the EPD). Based on the plasma pressure gradient suggested by the configuration of the diamagnetic currents, these two types of EPDs are referred to as low- and high-pressure EPDs, respectively.

The forthcoming statistical analysis uses simultaneous observations of the magnetic field and electron density obtained from the three Swarm satellites, starting in December 2013 until April 2018. Among the total number of EPDs detected, 81.7% correspond to low-pressure EPDs while 18.3% to high-pressure EPDs. Figure 6.3 shows the occurrence rate of both types of EPDs. The occurrence rate considers the total number of passes of each

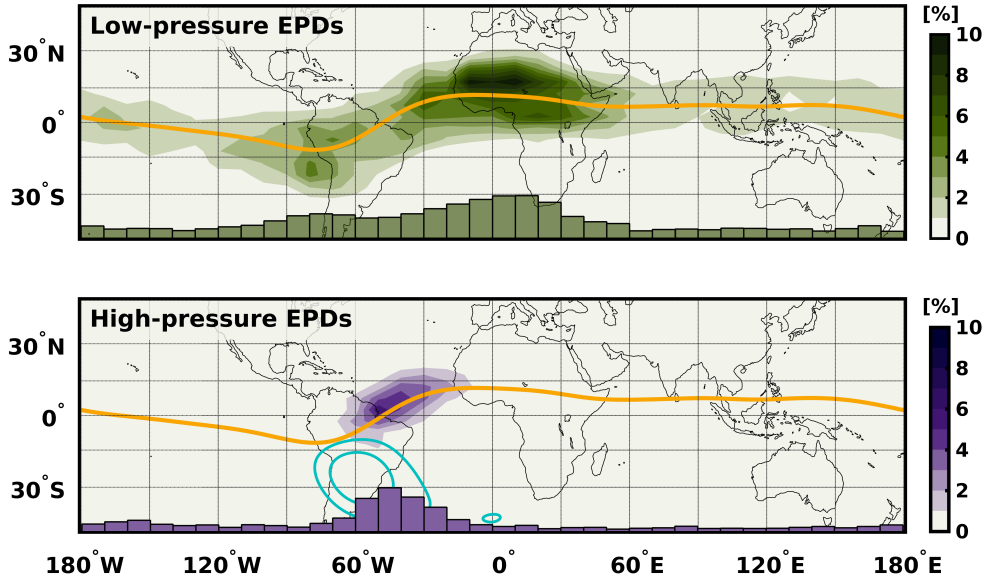

Fig. 6.3 Occurrence rate of low-pressure EPDs (top) and high-pressure EPDs (bottom) in a grid of $10^\circ \times 5^\circ$ in longitude and latitude, respectively. The longitudinal variation of the occurrence rate is depicted qualitatively by histograms at the bottom of each panel (10° bin). The highest value of events in each histogram is 665 (green) and 305 (purple). The yellow line represents the dip equator. The blue lines in the bottom panel depict the intensity of the magnetic field at the SAA. The inner and outer contours correspond to 23000 and 24000 nT, respectively.

satellite between 18 and 6 LT. It shows that low-pressure EPDs occur at all longitudes while high-pressure EPDs concentrate mainly over the South American/Atlantic region, between about 70°W and 10°W (54% of the total number of high-pressure EPDs). The histogram at the bottom of each map is meant to describe the longitudinal variability of the occurrence of EPDs only. The values are scaled for each panel with maxima of 665 and 305 for low- and high-pressure EPDs, respectively. Among the total number of EPDs detected between 70°W and 10°W, 67.1% correspond to low-pressure EPDs and 32.9% to high-pressure EPDs. It is interesting to note that low-pressure EPDs are detected mainly 'off' the equator (by about 10° in latitude) while high-pressure EPDs are detected near the equator. It may result from the fact that high-pressure EPDs mostly occur in a region of lower apex height, as it is shown later in the paper.

Figure 6.4 shows two columns of four panels each. From left to right, the columns correspond to low- and high-pressure EPDs. Each panel depicts the occurrence rate as a function of magnetic local time (MLT) and longitude for March equinox (February, March, April), June solstice (May, June, July), September equinox (August, September, October), and December solstice (November, December, January). Overall, low-pressure EPDs occur at all local times, except during December solstice where they have a preference for pre-midnight hours. High-pressure EPDs dominate around midnight and post-midnight hours with an earlier occurrence during December solstice. In general, the seasonal distribution of both low- and high-pressure EPDs agrees with the occurrence rate of EPDs known from earlier studies (e.g., Xiong et al., 2010, and references therein). It is interesting to note that the longitudinal distribution of the low-pressure EPDs varies with the seasons but not that of the high-pressure EPDs, which mostly occur between about 70°W and 10°W.

6.4 Discussion

As previously mentioned, the current driven by a plasma pressure gradient flows in such a way that it decreases/enhances the magnetic field in the region of highest/lowest plasma pressure (see Figure 6.2). In this study, the criterion to define EPDs as low- or high-pressure EPDs (i.e., plasma pressure) depends on the orientation of the magnetic perturbation $\delta\mathbf{B}_{\parallel}$ related to the diamagnetic current. As already specified, all the events in this study correspond to EPDs with good correlation between $\delta\mathbf{B}_{\parallel}$ and δn_e (i.e., $|cc| \geq 0.6$).

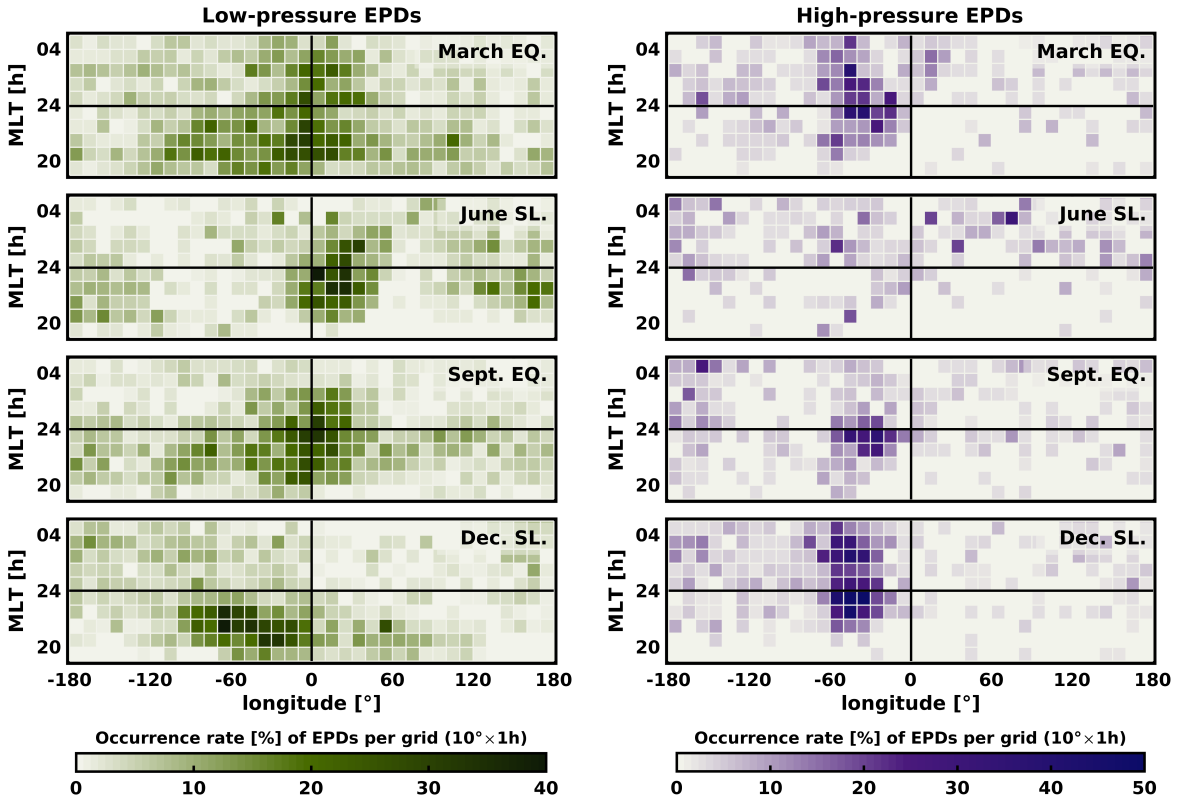

Fig. 6.4 Occurrence rate of low-pressure EPDs (Left) and high-pressure EPDs (Right) as a function of magnetic local time and longitude. Each panel from top to bottom corresponds to March equinox, June solstice, September equinox and December solstice.

By assuming a pressure balance between an EPD and the ambient plasma, we can estimate the mean temperature, i.e., $(T_{in}+T_{out})/2$, from the correlation between $\delta\mathbf{B}_{\parallel}B/\mu_0$ and $\delta n_e k$ as equation (3) suggests. Figure 6.5 presents such linear regression for both low-pressure EPDs (green dots) and high-pressure EPDs (purple dots). It shows that high-pressure EPDs have mostly low values of $\delta n_e k$ ($< 2\ m^{-3}J/K$) which implies they are shallow EPDs. The different distribution for the two types of EPDs in the regression is expected. It indicates, as is also observed in Figure 6.2, that $\delta\mathbf{B}_{\parallel}$ and δn_e are inversely and directly proportional across low- and high-pressure EPDs, respectively. At first sight, the values of $\delta\mathbf{B}_{\parallel}B/\mu_0$ and $\delta n_e k$ for both types of EPDs seem to follow a linear trend among the events. The better correlation for low-pressure EPDs (-0.61) might suggest that the balance between magnetic and plasma pressure comes mainly from variations of the plasma density. In other words, changes in the temperature across low-pressure EPDs appear not to play a significant role in the pressure balance. Another possible evidence of this stands on the mean temperature deduced from the slope of the linear regression. The value of 2200 K is quite close to the expected ambient plasma temperature of about 2000 K during pre-midnight hours (e.g., Lühr et al., 2002) and could confirm on average the assumption of isothermal conditions across of low-pressure EPDs. In the case of high-pressure EPDs, the low value of the correlation (0.44) might suggest that an additional parameter to plasma density, probably the temperature, plays a significant role in the pressure balance. A reasonable indication of this could be the value of the mean temperature (2900 K) deduced from the slope of the regression. It implies that high-pressure EPDs exhibit on average higher temperatures relative to the ambient plasma temperature, if the latter is assumed to be about 2000 K, as previously mentioned.

By defining the plasma pressure gradient as,

$$\nabla p = \nabla(nkT) = k\,(T\nabla n + n\nabla T)\,, \tag{6.4}$$

we can infer the magnitude of the temperature necessary for EPDs to present low- or high-plasma pressure. For low-pressure EPDs ($\nabla p > 0$, pointing outside the EPD), there are three cases. 1. The temperature inside an EPD is the same as outside ($T_{in} = T_{out}$, isothermal). 2. The temperature inside an EPD is lower than outside ($T_{in} < T_{out}$). 3. The temperature inside an EPD is higher than outside ($T_{in} > T_{out}$) and $|T\nabla n| > |n\nabla T|$. On the other side, high-pressure EPDs ($\nabla p < 0$, pointing inside the EPD) can only occur when the temperature inside an EPD is higher than outside and $|T\nabla n| < |n\nabla T|$. An estimation for the temperature inside a high-pressure EPD with respect to the temperature of the ambient plasma comes from equation (4) as,

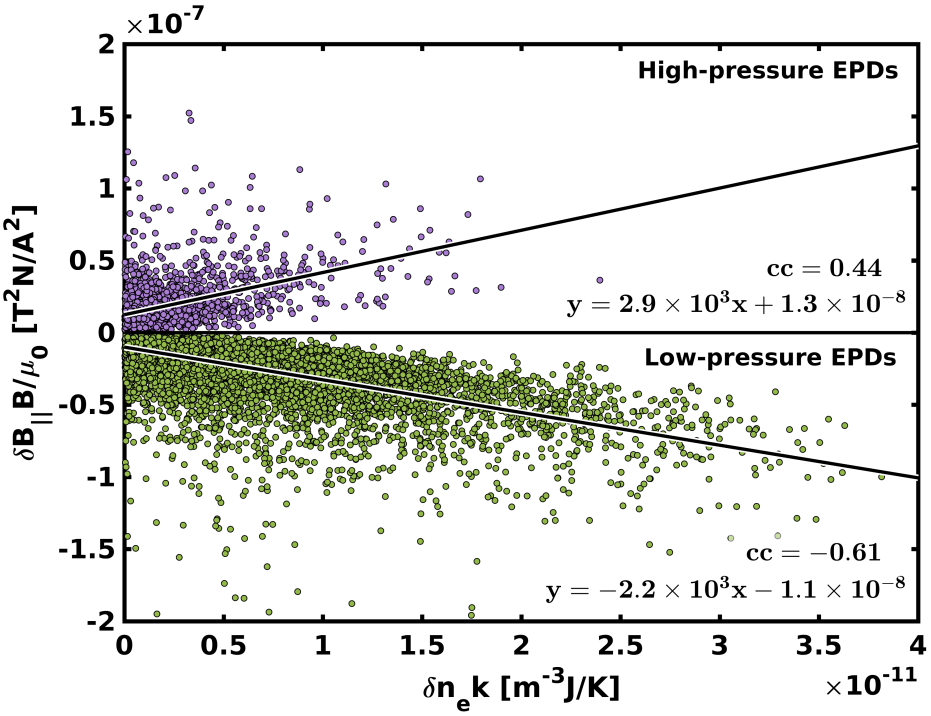

Fig. 6.5 Linear regression between the magnetic pressure and electron density variations for all the EPDs detected. Green dots represent low-pressure EPDs and purple dots high-pressure EPDs. In black, regression lines, related equations and correlation coefficients.

$$T_{in} > \frac{n_{out}}{n_{in}} T_{out}. \tag{6.5}$$

By taking measurements of the background density (n_{out}) and minimum density inside the depletions (n_{in}), we calculate the ratio n_{out}/n_{in} for each high-pressure EPD. The result shows a median of 1.96 (95% bootstrap confidence interval of $1.92-2.00$) which suggests that for an EPD to present high-plasma pressure, T_{in} must be roughly twice T_{out} or higher.

It is known from numerical simulations and observations that the plasma temperature within EPDs can be lower or higher than the background. Using the SAMI3/ESF code Huba et al. (2008) show that EPDs undergo both cooling and heating during their evolution. The authors suggest that the cooling is due to the increase of the EPD volume while rising, and the heating to the compression of ions when streaming down to the EPD feet, where magnetic field lines converge. Such a heating process has also been suggested by Park et al. (2008a) using observations from the ROCSAT-1, KOMPSAT-1, and DMSP missions. The authors describe that EPDs with enhanced temperatures are mainly related to fast poleward

field-aligned flows relative to the ambient plasma (about 260 $m.s^{-1}$). In another study, Oyama et al. (1988) propose two additional heating sources of EPDs, one by photoelectrons and another by particle precipitation. These two cases are based on electron temperature measurements across EPDs from the Japanese satellite Hinotori. In the first case, the authors found EPDs with temperatures as high as twice the background temperature between 4 and 9 LT. Due to the early hours, they associate the heating to the interaction with photoelectrons. In the second case, the authors found EPDs with enhanced temperatures of about 300 K relative to the background between 22 and 4 LT and located mainly over the South Atlantic magnetic anomaly (SAA). Because of the specific location, they relate the heating to particle precipitation.

The Swarm mission provides electron temperature measurements gathered by the Langmuir probes. Lomidze et al. (2018) validated the temperature with measurements of ground-based radars. The authors found that temperatures measured by Swarm usually overestimate by 300-400 K those measured by radars. However, the comparison between the two measurements presents high correlations (0.92-0.97) against the validation data. Even so, by looking at the temperature measurements, we note that suspicious fluctuations appear in regions of strong plasma density gradients, such as across EPDs. The electron temperatures from the Langmuir probes are derived assuming that the electrons have a Maxwellian velocity distribution in a coordinate system fixed with respect to the probe (Abe et al., 2013). In the case of a high-energy population associated with high-pressure EPDs, the temperature measurements could be inaccurate since particle distribution significantly deviates from a Maxwellian. Consequently, we prefer not to present any electron temperature measurement in this study.

The characteristics of the magnetic field at equatorial magnetic latitudes can also be of great importance to understand our observations. Figure 6.6 presents three panels. The first two panels show the occurrence rate of all detected low- and high-pressure EPDs as a function of magnetic local time (MLT) and longitude. From top to bottom, the third panel depicts the intensity (F) and declination (D) of the magnetic field at the dip equator, and the apex height (Apx), as well as their first derivatives as a function of longitude. The apex height is for magnetic field lines within $\pm 40^{\circ}$ of inclination [1]. This interval corresponds to a rough estimation of the region where EPDs generally occur. Based on LEO satellite data earlier studies have shown that the occurrence rate of EPDs takes place within about $\pm 30^{\circ}$ of magnetic latitude, with the highest occurrence at about $\pm 10^{\circ}$ (e.g., Stolle et al., 2006;

[1] i.e., magnetic field lines that present $\pm 40^{\circ}$ of dip at 0 km altitude, as given by IGRF.

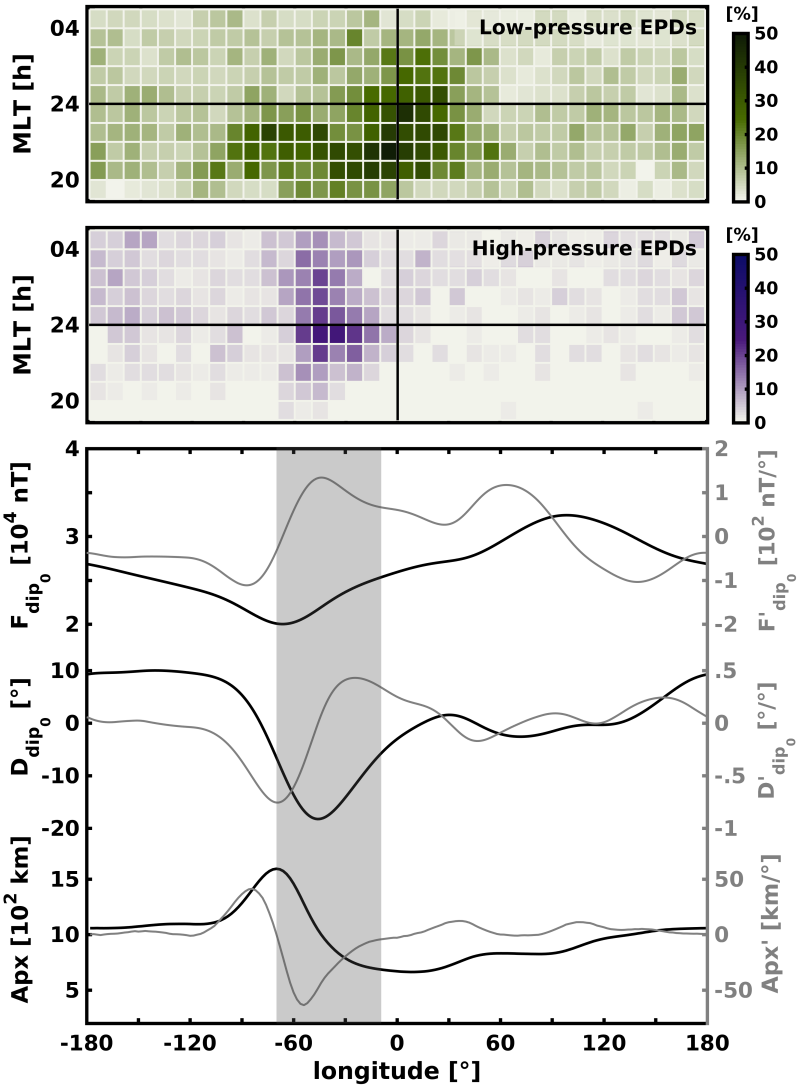

Fig. 6.6 Top panels: occurrence rate of all low-pressure EPDs (green) and high-pressure EPDs (purple) as a function of magnetic local time and longitude. Bottom panel: from top to bottom, magnetic field intensity (F) and declination (D) at the dip equator, and magnetic field apex height (Apx) for field-lines within $\pm 40^{\circ}$ of magnetic inclination. Gray lines show the first derivative of each parameter as a function of longitude.

Xiong et al., 2010). The region shaded in gray in the third panel of Figure 6.6 highlights the interval with the highest variations of the ambient magnetic field (see gray lines). In this region, the magnetic field intensity at the dip equator increases eastward from its minimum at about 70°W. Due to such increase of F, a sharp decrease of the apex height occurs from its maximum of about 1700 km at 70°W to a minimum of about 700 km at 10°W. Another exciting feature is the highest magnetic declination of about $-20°$ at 45°W.

The particular magnetic configuration of this region might influence different processes in the ionosphere that affect the evolution of EPDs. For example, what can happen to EPDs that grow and drift zonally to a region of higher magnetic intensity (lower apex height)? This is the case for EPDs in the region where high-pressure EPDs are mostly detected (see Figure 6.6, 70°W − 10°W). If we assume an EPD originates around $70°W$ at about 18 MLT, and drifts zonally eastward at 150 $m.s^{-1}$ (e.g., Makela et al., 2005), it should reach $45°W$ at about 23 MLT. This latter longitude and MLT agree with those of the highest occurrence rate of high-pressure EPDs. At first glance, we might expect these EPDs undergo compression while drifting as the magnetic pressure increases with longitude. In that regard, we can roughly estimate the rise in temperature by calculating the volume change of a magnetic flux tube from $70°W$ to $45°W$. Assuming an isotropic ionosphere, the temperature rises by only 8.6%, corresponding to a decrease of the magnetic flux tube volume by 11.8%. If indeed heating by adiabatic compression may contribute to the rise of temperature within EPDs in this region, it would not be sufficient for reaching temperatures as high as twice the ambient plasma temperature, as the result from equation (5) suggests.

On the other side, there is an additional phenomenon that might help in raising the temperature within EPDs. Due also to the characteristics of the ambient magnetic field in this region and its vicinities (i.e., the SAA), particle precipitation could be a more effective heating mechanism within EPDs, as proposed by Oyama et al. (1988). In their study, the authors conclude that in such a case, the heating of plasma inside EPDs can only occur by the interaction of thermal electrons with fast electrons (soft-electrons) flowing along magnetic field lines. Since most of the high-pressure EPDs are shallow (see Figure 6.5, $\delta n_e k < 2\ m^{-3} J/K$), the heating process should not require that much energy to achieve temperatures within EPDs as high as the double of the background. Therefore, it is likely that low-pressure EPDs generated at $70°W$ get heated while crossing SAA longitudes and reach the temperature necessary to become high-pressure EPDs at about $45°W$ (see Figure 6.3, lower panel). Certainly, this suggestion must be tested in a further study by using measurements of electron fluxes and if possible of electron temperatures across EPDs. In this paper,

we consider only magnetic and plasma pressures and neglect other contributions to the pressure balance, such as plasma inertia and ion/neutral friction. In this respect, the use of measurements of the electric field across EPDs might also help us to better understand the pressure balance mechanism, especially in the case of high-pressure EPDs.

6.5 Summary and Conclusions

In this study, we report the first observational evidence of high plasma pressure in depleted density regions in the ionosphere. The detected structures correspond to large-scale equatorial plasma depletions (EPDs) with a decrease of the magnetic field within the EPD. To assess the balance between magnetic and plasma pressures across both low- and high-pressure EPDs, continuous magnetic field and electron density measurements from the Swarm constellation mission are used from December 2013 to April 2018. The criterion to define an EPD as of low- or high-pressure (plasma pressure) is the orientation of its related diamagnetic current. The main results and conclusions of this study are as follows:

1. For low-pressure EPDs, the plasma pressure gradient is mostly dominated by variations of the plasma density. Changes in the plasma temperature are not expected to play a significant role. On the contrary, variations of the plasma temperature are significant for high-pressure EPDs.

2. Among all the EPDs detected, 18.3% correspond to high-pressure EPDs and 81.7% to low-pressure EPDs.

3. High-pressure EPDs occur at the American/Atlantic sector mainly, between about 70°W and 10°W, corresponding to 54% of the total number of high-pressure EPDs detected. A preference in magnetic local time is found around midnight and post-midnight hours.

4. High-pressure EPDs are apparently characterized by temperatures as high as twice the ambient plasma temperature.

5. Based on the location of the highest occurrence rate of high-pressure EPDs (i.e., near the SAA), we suggest the main heating mechanism to be due to particle precipitation from the radiation belts.

Chapter 7

Conclusions and outlook

The adverse effect of EPDs and associated irregularities on the propagation of transionospheric radio waves makes imminent their study. The three-dimensional nature of the phenomena requires numerical modeling to appreciate their variability fully. In this process, the measurement of ionospheric parameters such as electric and magnetic fields, ion and electron temperatures, plasma and neutral mass densities and neutral winds are fundamental to validate and shed new light on the dynamics of the phenomena itself and the ambient ionosphere. The investigation in this dissertation contributed to solving specific issues in the current knowledge of EPDs. Its results represent a step forward in the current understanding of the electrodynamics of EPDs. Specifically, this study contributed to answering *what is the direction of propagation of the electromagnetic energy associated with EPDs?*, *what are the variations in space and time of the electric currents related to EPDs i.e., seasonal/geographical and local time dependencies?*, and *under what conditions does the balance between magnetic and plasma pressure associated with EPDs occur?*. These questions have represented a challenge in the simulation of EPDs (e.g., Aveiro et al., 2011; Bhattacharyya and Burke, 2000; Burke, 1979; Dao et al., 2013; Yokoyama et al., 2014) and only a few studies have addressed these issues using observations (e.g., Aggson et al., 1992a; Lühr et al., 2014; Park et al., 2009; Pottelette et al., 2007; Stolle et al., 2006). The lack of extended data sets and simultaneous high-resolution measurements of different parameters had not allowed conclusive results in this regard. By using the unique set of measurements of *Swarm* I provided the first observational evidence of interhemispheric electromagnetic energy flux and field-aligned currents, the first spatial and temporal characterization of EPDs based on their associated field-aligned and diamagnetic currents, and the first evidence of high plasma pressure in regions of depleted plasma density in the ionosphere.

In the following sections, I summarize the key findings of the corresponding investigations and end up with an outlook to future work.

7.1 Conclusions

Chapter 4 corresponds to Rodríguez-Zuluaga et al. (2017), which focused on the orientation of the EPDs-related Poynting flux parallel to the ambient magnetic field. In that study, in situ measurements of electron density were used to detect EPDs and static electric and magnetic fields to compute the orientation of the energy flux. It was concluded that the Poynting flux has a preference to be directed towards one magnetic hemisphere. That is, the EPDs-related electromagnetic energy flows from one magnetic hemisphere to the other with a longitudinal and seasonal dependence. Taking into account that studies standing on numerical models have suggested that the energy associated with EPDs must flow away from the dip equator (e.g., Bhattacharyya and Burke, 2000; Dao et al., 2013; Yokoyama et al., 2014), the observations of an interhemispheric Poynting flux represent a step forward in our current understanding of the evolution of EPDs. Even though the lack of an extended set of electric field data did not allow a climatological analysis of the Poynting flux itself, the continuous magnetic field measurements were used to derive the orientation of field-aligned currents at the edges of EPDs. These data proved to be a valuable source of information to understand the direction of propagation of the energy.

Chapters 5 addressed the magnetic field-aligned currents, one of the most prominent electric currents associated with EPDs. In Rodríguez-Zuluaga and Stolle (2019), we used electron density and magnetic field data to characterize EPDs based on the orientation of the field-aligned currents. Previous studies based on numerical models suggest that the field-aligned currents must close around both feet of the EPD. That is, the currents must flow away from the dip equator at the western wall of the depletion and towards the dip equator at the eastern wall (e.g., Aveiro et al., 2011; Burke, 1979; Dao et al., 2013; Yokoyama and Stolle, 2017). In contrast, this study concluded that the field-aligned currents are mainly interhemispheric. The closure of the currents around a particular EPDs-foot presents a distinct longitudinal/seasonal dependence. By computing the ionospheric conductivity from empirical models, it was observed that the preference of the currents to close in one particular hemisphere generally coincides with the hemisphere with the highest Pedersen conductance. Such hemispherical preference presents a seasonal/longitudinal dependence.

Chapter 6 corresponds to Rodríguez-Zuluaga et al. (2019), which considered the orientation of the diamagnetic currents associated with EPDs to study the pressure balance across these regions. In that investigation, we used electron density and magnetic field measurements to assess the pressure balance from a climatological point of view. Studies about the diamagnetic effect in the ionosphere have shown that variations in the plasma pressure gradient are dominated by the plasma density mainly (e.g., Laundal et al., 2019; Lühr et al., 2003). In that regard, the plasma pressure within EPDs must be lower than the ambient plasma pressure. This investigation concluded that EPDs could present plasma pressure either higher or lower than the ambient. Of particular concern are EPDs with higher plasma pressure than the ambient. By using electron density measurements, it was deduced that high plasma pressure inside EPDs occur when their temperature is approximately twice of the ambient. Due to their most frequent occurrence near the *South Atlantic magnetic anomaly*, we suggest that interaction of thermal electrons with fast electrons coming from the ring current and radiation belts can be the source of those high temperatures. Heating electrons is more efficient than heating ions, especially in regions of low plasma density taking into account that the cooling rates are directly proportional to the square of the plasma density (Stolle et al., 2011). This finding sheds new light on the current knowledge of EPDs by providing information about the effect of parameters such as the ambient magnetic field and ambient plasma on the evolution of EPDs.

7.2 Outlook

Energy source and dissipation

In Chapter 4, it was concluded that the EPDs-related energy flux parallel to the ambient magnetic field generally goes from one magnetic hemisphere to the other. Considering that this conclusion is valid only above the altitude of the *Swarm* satellites (about 470 km), the precise location of the energy source or generator remains unknown. Since EPDs are gravitational instabilities, it is expected that the background plasma plays an essential role in determining the location of the generator. Nevertheless, in Chapter 5, it was shown that by assuming a growing EPD (e.g., eastward polarization electric field) the energy seems to dissipate into the hemisphere with the highest conductivity. Thus, it is unclear whether a stronger gravitational perturbation or a more significant conductivity in one of the magnetic hemispheres is what determines the direction of the energy flux. Both observations and simulation studies are needed to answer any of the questions above. A more extensive data

set of simultaneous measurements of electric and magnetic fields are required to thoroughly assess the spatial and temporal characteristics of the Poynting flux. A three-dimensional model with realistic parameters such as background plasma density, conductivity, and neutral winds is also currently lacking. The well-known asymmetries of these parameters between hemispheres might shed new light on the direction of the EPDs-related energy flow.

Electric current system

The diamagnetic currents have proved to be a valuable source of information to comprehend the large-scale dynamics of the plasma in the ionosphere. Variations in the magnetic field associated with these currents are known to follow reasonably well the variations of the plasma density at different latitudes and scale-sizes (e.g., Laundal et al., 2019; Lühr et al., 2003; Rodríguez-Zuluaga et al., 2019). High-resolution measurements of the magnetic field gathered by the *Swarm* constellation mission can shed light on the small-scale structures in the ionosphere. Particularly in the study of EPDs, the 50 Hz magnetic field measurements from *Swarm* can be used to analyze the plasma density dynamics of structures in the range of hundreds of meters. This high resolution is a compelling advantage due to the lower resolution (up to 16 Hz) of the plasma density measurements that most of the other satellite missions gather. Additionally, the assessment of smaller density structures associated with EPDs might give relevant hints about their precise effect on radio wave propagation that result in the outages and loss of signal of *global navigation satellite systems*.

The closure of field-aligned currents associated with EPDs presents a seasonal, longitudinal, and local time dependence. The investigation in this dissertation focused only on EPDs with symmetric currents at both sides of the EPDs (western and eastern edges). Due to the importance of these currents to comprehend the dissipation of energy and evolution of EPDs, it is crucial to also understand under what conditions EPDs present asymmetries or absence of field-aligned currents. This issue can be addressed by systematically assessing their spatial and temporal characteristics using measurements from the *Swarm* mission. Additionally, valuable information might come from numerical simulations using a three-dimensional electrostatic potential. Simulations based on the equipotential field line approach can not adequately describe the three-dimensional structure of the currents. This approach which is commonly used underestimates the vertical current flowing through the equatorial *F* region (Aveiro and Hysell, 2012).

Pressure balance

One of the most exciting findings in this dissertation is the presence of high plasma pressure in regions of depleted plasma density. We argued based on plasma density measurements across EPDs that such characteristic can occur if the temperature inside the depletion is approximate twice the ambient. We suggested that such high temperatures are due to the heating of thermal electrons by interaction with soft electrons from the ring current and radiation belts. This statement must be validated in future studies by using additional measurements and considering additional terms neglected in the present study (Rodríguez-Zuluaga et al., 2019). In more detail, it is necessary to first determine the connection between the precipitation of particles and the occurrence of high-pressure EPDs. It can be done by looking at measurements of electron fluxes from missions such as POES and comparing them with variations in the occurrence rate of EPDs. It is also interesting to estimate the energy needed to reach such temperatures. Furthermore, it is crucial to analyze in situ electron temperature measurements. Although observations from *Swarm* did not show the expected magnitudes, the fact that temperatures derived from Langmuir probes are limited to a Maxwellian distribution of the particle velocities opens the possibility of an internal smoothing of the temperatures across EPDs. Furthermore, in Rodríguez-Zuluaga et al. (2019), different terms were neglected, such as magnetic tension, the collision of ions with neutrals and inertial terms. Their theoretical consideration might lead to a better understanding of the phenomena by considering wave activity within EPDs.

References

Abe, T., Oyama, K.-I., et al. (2013). Langmuir probe. *An Introduction to Space Instrumentation, Edited by K.-I. Oyama and C.Z. Cheng, pp. 63-75. Online at http://www.terrapub.co.jp/onlineproceedings/ste/aisi/index.html), p. 63*, pages 63–75.

Aggson, T. L., Burke, W. J., Maynard, N. C., Hanson, W. B., Anderson, P. C., Slavin, J. A., Hoegy, W. R., and Saba, J. L. (1992a). Equatorial bubbles updrafting at supersonic speeds. *Journal of Geophysical Research: Space Physics*, 97(A6):8581–8590.

Aggson, T. L., Maynard, N. C., Hanson, W. B., and Saba, J. L. (1992b). Electric field observations of equatorial bubbles. *Journal of Geophysical Research: Space Physics*, 97(A3):2997–3009.

Alken, P., Maus, S., Richmond, A., and Maute, A. (2011). The ionospheric gravity and diamagnetic current systems. *Journal of Geophysical Research: Space Physics*, 116(A12).

Alken, P., Maute, A., and Richmond, A. (2017). The F-region gravity and pressure gradient current systems: A review. *Space Science Reviews*, 206(1-4):451–469.

Appleton, E. V. (1932). Wireless studies of the ionosphere. *Institution of Electrical Engineers-Proceedings of the Wireless Section of the Institution*, 7(21):257–265.

Appleton, E. V. (1946). Two anomalies in the ionosphere. *Nature*, 157(3995):691.

Aubert, J. and Finlay, C. C. (2019). Geomagnetic jerks and rapid hydromagnetic waves focusing at Earth's core surface. *Nature Geoscience*, 12(5):393.

Aveiro, H. and Hysell, D. (2010). Three-dimensional numerical simulation of equatorial F region plasma irregularities with bottomside shear flow. *Journal of Geophysical Research: Space Physics*, 115(A11).

Aveiro, H., Hysell, D., Park, J., and Lühr, H. (2011). Equatorial spread F-related currents: Three-dimensional simulations and observations. *Geophysical Research Letters*, 38(21).

Aveiro, H. C. and Hysell, D. L. (2012). Implications of the equipotential field line approximation for equatorial spread F analysis. *Geophysical Research Letters*, 39(11).

Basu, B. (2002). On the linear theory of equatorial plasma instability: Comparison of different descriptions. *Journal of Geophysical Research: Space Physics*, 107(A8).

Basu, B. (2005). Characteristics of electromagnetic rayleigh-taylor modes in nighttime equatorial plasma. *Journal of Geophysical Research: Space Physics*, 110(A2).

References

Bhattacharyya, A. and Burke, W. J. (2000). A transmission line analogy for the development of equatorial ionospheric bubbles. *Journal of Geophysical Research: Space Physics*, 105(A11):24941–24950.

Bilitza, D., Altadill, D., Truhlik, V., Shubin, V., Galkin, I., Reinisch, B., and Huang, X. (2017). International Reference Ionosphere 2016: From ionospheric climate to real-time weather predictions. *Space Weather*, 15(2):418–429.

Booker, H. and Wells, H. (1938). Scattering of radio waves by the F-region of the ionosphere. *Terrestrial Magnetism and Atmospheric Electricity*, 43(3):249–256.

Buchert, S., Zangerl, F., Sust, M., André, M., Eriksson, A., Wahlund, J.-E., and Opgenoorth, H. (2015). Swarm observations of equatorial electron densities and topside GPS track losses. *Geophysical Research Letters*, 42(7):2088–2092.

Burchill, J. and Knudsen, D. (2017). EFI TII cross-track flow data release notes. Technical Report SW-RN-UoC-GS-004, Data, Innovation, and Science Cluster.

Burke, W. I. (1979). Plasma bubbles near the dawn terminator in the topside ionosphere. *Planetary and Space Science*, 27(9):1187–1193.

Burke, W. J., Gentile, L. C., Shomo, S. R., Roddy, P. A., and Pfaff, R. F. (2012). Images of bottomside irregularities observed at topside altitudes. *Journal of Geophysical Research: Space Physics*, 117(A3).

Calvert, W. and Schmid, C. W. (1964). Spread-F observations by the Alouette topside sounder satellite. *Journal of Geophysical Research*, 69(9):1839–1852.

Chartier, A. T., Mitchell, C. N., and Miller, E. S. (2018). Annual occurrence rates of ionospheric polar cap patches observed using Swarm. *Journal of Geophysical Research: Space Physics*, 123(3):2327–2335.

Chaturvedi, P. and Ossakow, S. (1977). Nonlinear theory of the collisional Rayleigh-Taylor instability in equatorial spread F. *Geophysical Research Letters*, 4(12):558–560.

Cohen, R. and Bowles, K. L. (1963). Ionospheric VHF scattering near the magnetic equator during the International Geophysical Year. *J. Res. Natl. Bur. Stand. US, Sect. D*, 67:459–480.

Dao, E., Seyler, C., and Kelley, M. (2013). Three-dimensional modeling of the electromagnetic characteristics of equatorial plasma depletions. *Journal of Geophysical Research: Space Physics*, 118(6):3505–3514.

Dolginov, S. S., Zhuzgov, L., and Pushkov, N. (1959). Preliminary report on geomagnetic measurements carried out from the Third Soviet Artificial Earth Satellite. *Artificial Earth Satellites*, 2:63–67.

Drob, D. P., Emmert, J. T., Meriwether, J. W., Makela, J. J., Doornbos, E., Conde, M., Hernandez, G., Noto, J., Zawdie, K. A., McDonald, S. E., Huba, J. D., and Klenzing, J. H. (2015). An update to the Horizontal Wind Model (HWM): The quiet time thermosphere. *Earth and Space Science*, 2(7):301–319.

Dungey, J. (1956). Convective diffusion in the equatorial F region. *Journal of Atmospheric and Terrestrial Physics*, 9(5-6):304–310.

Eastes, R., Solomon, S., Daniell, R., Anderson, D., Burns, A., England, S., Martinis, C., and McClintock, W. (2019). Global-scale observations of the equatorial ionization anomaly. *Geophysical Research Letters*, 46.

Eccles, J. V. (1998). Modeling investigation of the evening prereversal enhancement of the zonal electric field in the equatorial ionosphere. *Journal of Geophysical Research: Space Physics*, 103(A11):26709–26719.

Farley, D., Balsey, B., Woodman, R., and McClure, J. (1970). Equatorial spread F: Implications of VHF radar observations. *Journal of Geophysical Research*, 75(34):7199–7216.

Farley, D., Bonelli, E., Fejer, B. G., and Larsen, M. (1986). The prereversal enhancement of the zonal electric field in the equatorial ionosphere. *Journal of Geophysical Research: Space Physics*, 91(A12):13723–13728.

Fejer, B. G., Jensen, J. W., and Su, S.-Y. (2008). Quiet time equatorial F region vertical plasma drift model derived from ROCSAT-1 observations. *Journal of Geophysical Research: Space Physics*, 113(A5).

Fejer, B. G. and Kelley, M. (1980). Ionospheric irregularities. *Reviews of Geophysics*, 18(2):401–454.

Finlay, C. C., Olsen, N., Kotsiaros, S., Gillet, N., and Tøffner-Clausen, L. (2016). Recent geomagnetic secular variation from Swarm and ground observatories as estimated in the CHAOS-6 geomagnetic field model. *Earth, Planets and Space*, 68(1):112.

Forbes, J. M. and Garrett, H. B. (1979). Solar tidal wind structures and the E-region dynamo. *Journal of geomagnetism and geoelectricity*, 31(3):173–182.

Friis-Christensen, E., Lühr, H., and Hulot, G. (2006). Swarm: A constellation to study the Earth's magnetic field. *Earth, planets and space*, 58(4):351–358.

Fukao, S., Ozawa, Y., Yokoyama, T., Yamamoto, M., and Tsunoda, R. T. (2004). First observations of the spatial structure of f region 3-m-scale field-aligned irregularities with the equatorial atmosphere radar in indonesia. *Journal of Geophysical Research: Space Physics*, 109(A2).

Gary, J., Heelis, R., Hanson, W., and Slavin, J. (1994). Field-aligned Poynting flux observations in the high-latitude ionosphere. *Journal of Geophysical Research: Space Physics*, 99(A6):11417–11427.

Gentile, L., Burke, W., and Rich, F. (2006). A climatology of equatorial plasma bubbles from DMSP 1989–2004. *Radio Science*, 41(5).

Goodwin, L., Iserhienrhien, B., Miles, D. M., Patra, S., van der Meeren, C., Buchert, S. C., Burchill, J., Clausen, L. B. N., Knudsen, D. J., McWilliams, K. A., et al. (2015). Swarm in situ observations of F region polar cap patches created by cusp precipitation. *Geophysical Research Letters*, 42(4):996–1003.

References

Haaser, R. A., Earle, G. D., Heelis, R. A., Klenzing, J., Stoneback, R., Coley, W. R., and Burrell, A. G. (2000). Characteristics of low-latitude ionospheric depletions and enhancements during solar minimum. *Journal of Geophysical Research: Space Physics*, 117(A10).

Haerendel, G. (1973). Theory of equatorial spread F. *Max-Plank Inst. für Phys. and Astrophys. preprint*.

Hanson, W. B. and Sanatani, S. (1971). Relationship between Fe+ ions and equatorial spread F. *Journal of Geophysical Research*, 76(31):7761–7768.

Heelis, R. (2004). Electrodynamics in the low and middle latitude ionosphere: A tutorial. *Journal of Atmospheric and Solar-Terrestrial Physics*, 66(10):825–838.

Huang, C., Burke, W., Machuzak, J., Gentile, L., and Sultan, P. (2001). DMSP observations of equatorial plasma bubbles in the topside ionosphere near solar maximum. *Journal of Geophysical Research: Space Physics*, 106(A5):8131–8142.

Huba, J., Joyce, G., and Krall, J. (2008). Three-dimensional equatorial spread F modeling. *Geophysical Research Letters*, 35(10).

Hudson, M. K. and Kennel, C. F. (1975). Linear theory of equatorial spread F. *Journal of Geophysical Research*, 80(34):4581–4590.

Hysell, D. (2000). An overview and synthesis of plasma irregularities in equatorial spread F. *Journal of Atmospheric and Solar-Terrestrial Physics*, 62(12):1037–1056.

Hysell, D., Chun, J., and Chau, J. (2004). Bottom-type scattering layers and equatorial spread F. *Annales Geophysicae*, 22(12):4061–4069.

Hysell, D. and Kudeki, E. (2004). Collisional shear instability in the equatorial F region ionosphere. *Journal of Geophysical Research: Space Physics*, 109(A11).

Iyemori, T., Nakanishi, K., Aoyama, T., Yokoyama, Y., Koyama, Y., and Lühr, H. (2015). Confirmation of existence of the small-scale field-aligned currents in middle and low latitudes and an estimate of time scale of their temporal variation. *Geophysical Research Letters*, 42(1):22–28.

Jivani, M., Joshi, H., Pathak, K., Mathew, B., and Iyer, K. (2000). Effect of ionospheric plasma irregularities on communication system parameters. *IETE Technical Review*, 17(1-2):43–50.

Kelley, M. and Hysell, D. (1991). Equatorial spread-F and neutral atmospheric turbulence: a review and a comparative anatomy. *Journal of Atmospheric and Terrestrial Physics*, 53(8):695–708.

Kelley, M., Ilma, R., and Crowley, G. (2009). On the origin of pre-reversal enhancement of the zonal equatorial electric field. *Ann. Geophys*, 27(5):2053–2056.

Kelley, M. C. (2009). *The Earth's ionosphere: Plasma physics and electrodynamics*, volume 96. Academic press.

Kelley, M. C., Makela, J. J., de La Beaujardière, O., and Retterer, J. (2011). Convective ionospheric storms: A review. *Reviews of Geophysics*, 49(2).

Kil, H., Heelis, R. A., Paxton, L. J., and Oh, S.-J. (2009). Formation of a plasma depletion shell in the equatorial ionosphere. *Journal of Geophysical Research: Space Physics*, 114(A11).

Kil, H. and Paxton, L. J. (2017). Global distribution of nighttime medium-scale traveling ionospheric disturbances seen by Swarm satellites. *Geophysical Research Letters*, 44(18):9176–9182.

Kim, H., Hwang, J., Park, J., Bortnik, J., and Lee, J. (2018). Global characteristics of electromagnetic ion cyclotron waves deduced from Swarm satellites. *Journal of Geophysical Research: Space Physics*, 123(2):1325–1336.

Knudsen, D., Burchill, J., Buchert, S., Coco, I., Tøffner-Clausen, L., and Olsen, H. P. (2015). Swarm preliminary plasma dataset user note. Technical Report SWAM-GSEG-EOPG-TN-15-0003, European Space Agency.

Knudsen, D., Burchill, J., Buchert, S., Eriksson, A., Gill, R., Wahlund, J.-E., Åhlen, L., Smith, M., and Moffat, B. (2017). Thermal ion imagers and Langmuir probes in the Swarm electric field instruments. *Journal of Geophysical Research: Space Physics*, 122(2):2655–2673.

Knudsen, D., Kelley, M., Earle, G., Vickrey, J., and Boehm, M. (1990). Distinguishing Alfvén waves from quasi-static field structures associated with the discrete aurora: Sounding rocket and HILAT satellite measurements. *Geophysical Research Letters*, 17(7):921–924.

Koons, H., Roeder, J., and Rodriguez, P. (1997). Plasma waves observed inside plasma bubbles in the equatorial F region. *Journal of Geophysical Research: Space Physics*, 102(A3):4577–4583.

Krall, J., Huba, J., Joyce, G., and Zalesak, S. (2009). Three-dimensional simulation of equatorial spread-F with meridional wind effects. *Ann. Geophys*, 27(5):1821–1830.

Krall, J., Huba, J. D., Ossakow, S. L., and Joyce, G. (2010). Why do equatorial ionospheric bubbles stop rising? *Geophysical Research Letters*, 37(9).

Kudeki, E., Akgiray, A., Milla, M., Chau, J. L., and Hysell, D. L. (2007). Equatorial spread-F initiation: Post-sunset vortex, thermospheric winds, gravity waves. *Journal of Atmospheric and Solar-Terrestrial Physics*, 69(17-18):2416–2427.

Kudeki, E. and Bhattacharyya, S. (1999). Postsunset vortex in equatorial F-region plasma drifts and implications for bottomside spread-F. *Journal of Geophysical Research: Space Physics*, 104(A12):28163–28170.

Kudeki, E., Fejer, B. G., Farley, D., and Ierkic, H. (1981). Interferometer studies of equatorial F region irregularities and drifts. *Geophysical Research Letters*, 8(4):377–380.

Laakso, H., Aggson, T. L., Pfaff, R. F., and Hanson, W. B. (1994). Downdrafting plasma flow in equatorial bubbles. *Journal of Geophysical Research: Space Physics*, 99(A6):11507–11515.

Langel, R., Ousley, G., Berbert, J., Murphy, J., and Settle, M. (1982). The magsat mission. *Geophysical Research Letters*, 9(4):243–245.

Laundal, K. M., Finlay, C. C., and Olsen, N. (2016). Sunlight effects on the 3D polar current system determined from low earth orbit measurements. *Earth, Planets and Space*, 68(1):142.

Laundal, K. M., Hatch, S., and Moretto, T. (2019). Magnetic effects of plasma pressure gradients in the upper F region. *Geophysical Research Letters*, 46(5):2355–2363.

Leger, J.-M., Bertrand, F., Jager, T., Le Prado, M., Fratter, I., and Lalaurie, J.-C. (2009). Swarm absolute scalar and vector magnetometer based on helium 4 optical pumping. *Procedia Chemistry*, 1(1):634–637.

Livermore, P. W., Hollerbach, R., and Finlay, C. C. (2017). An accelerating high-latitude jet in Earth's core. *Nature Geoscience*, 10(1):62.

Lomidze, L., Burchill, J., Knudsen, D. J., Kouznetsov, A., and Weimer, D. R. (2019). Validity study of the Swarm horizontal cross-track ion drift velocities in the high-latitude ionosphere. *Earth and Space Science*.

Lomidze, L., Knudsen, D. J., Burchill, J., Kouznetsov, A., and Buchert, S. C. (2018). Calibration and validation of Swarm plasma densities and electron temperatures using ground-based radars and satellite radio occultation measurements. *Radio Science*, 53(1):15–36.

Lühr, H., Kervalishvili, G., Michaelis, I., Rauberg, J., Ritter, P., Park, J., Merayo, J. M., and Brauer, P. (2015a). The interhemispheric and F region dynamo currents revisited with the Swarm constellation. *Geophysical Research Letters*, 42(9):3069–3075.

Lühr, H., Maus, S., Rother, M., and Cooke, D. (2002). First in-situ observation of night-time F region currents with the CHAMP satellite. *Geophysical research letters*, 29(10).

Lühr, H., Park, J., Gjerloev, J. W., Rauberg, J., Michaelis, I., Merayo, J. M., and Brauer, P. (2015b). Field-aligned currents' scale analysis performed with the Swarm constellation. *Geophysical Research Letters*, 42(1):1–8.

Lühr, H., Park, J., Xiong, C., and Rauberg, J. (2014). Alfvén wave characteristics of equatorial plasma irregularities in the ionosphere derived from CHAMP observations. *Frontiers in Physics*, 2:47.

Lühr, H., Rother, M., Maus, S., Mai, W., and Cooke, D. (2003). The diamagnetic effect of the equatorial appleton anomaly: Its characteristics and impact on geomagnetic field modeling. *Geophysical Research Letters*, 30(17).

Makela, J., Kelley, M., and Su, S.-Y. (2005). Simultaneous observations of convective ionospheric storms: ROCSAT-1 and ground-based imagers. *Space Weather*, 3(12).

Martinis, C. and Mendillo, M. (2007). Equatorial spread F-related airglow depletions at Arecibo and conjugate observations. *Journal of Geophysical Research: Space Physics*, 112(A10).

Martyn, D. (1959). The normal F region of the ionosphere. *Proceedings of the IRE*, 47(2):147–155.

Maruyama, T. (1988). A diagnostic model for equatorial spread F, 1, model description and application to electric field and neutral wind effects. *Journal of Geophysical Research: Space Physics*, 93(A12):14611–14622.

McClure, J., Hanson, W., and Hoffman, J. (1977). Plasma bubbles and irregularities in the equatorial ionosphere. *Journal of Geophysical Research*, 82(19):2650–2656.

McGranaghan, R. M., Mannucci, A. J., and Forsyth, C. (2017). A comprehensive analysis of multiscale field-aligned currents: Characteristics, controlling parameters, and relationships. *Journal of Geophysical Research: Space Physics*, 122(12):11–931.

Merayo, J. M. G., Jørgensen, J. L., Friis-Christensen, E., Brauer, P., Primdahl, F., Jørgensen, P. S., Allin, T. H., and Denver, T. (2008). *The Swarm Magnetometry Package*, pages 143–151. Springer Netherlands, Dordrecht.

Morse, F., Edgar, B., Koons, H., Rice, C., Heikkila, W., Hoffman, J., Tinsley, B., Winningham, J., Christensen, A., Woodman, R., and Pomalaza, J. (1977). Equion, an equatorial ionospheric irregularity experiment. *Journal of Geophysical Research*, 82(4):578–592.

Neubert, T., Mandea, M., Hulot, G., Frese, R., Primdahl, F., Jørgensen, J. L., Friis-Christensen, E., Stauning, P., Olsen, N., and Risbo, T. (2001). Ørsted satellite captures high-precision geomagnetic field data. *Eos, Transactions American Geophysical Union*, 82(7):81–88.

Neufeld, M. J. (2018). *Spaceflight: A Concise History*. MIT Press.

Olsen, N. (1997). Ionospheric F region currents at middle and low latitudes estimated from Magsat data. *Journal of Geophysical Research: Space Physics*, 102(A3):4563–4576.

Olsen, N., Friis-Christensen, E., Floberghagen, R., Alken, P., Beggan, C. D., Chulliat, A., Doornbos, E., Da Encarnação, J. T., Hamilton, B., Hulot, G., et al. (2013). The Swarm satellite constellation application and research facility (SCARF) and Swarm data products. *Earth, Planets and Space*, 65(11):1.

Olsen, N. and Stolle, C. (2012). Satellite geomagnetism. *Annual Review of Earth and Planetary Sciences*, 40:441–465.

Ossakow, S. L. (1981). Spread-F theories-A review. *Journal of Atmospheric and Terrestrial Physics*, 43(5-6):437–452.

Oyama, K.-I., Schlegel, K., and Watanabe, S. (1988). Temperature structure of plasma bubbles in the low latitude ionosphere around 600 km altitude. *Planetary and space science*, 36(6):553–567.

Pakhotin, I., Mann, I., Lysak, R., Knudsen, D., Gjerloev, J., Rae, I., Forsyth, C., Murphy, K., Miles, D., Ozeke, L., et al. (2018). Diagnosing the role of alfvén waves in magnetosphere-ionosphere coupling: Swarm observations of large amplitude nonstationary magnetic perturbations during an interval of northward imf. *Journal of Geophysical Research: Space Physics*, 123(1):326–340.

Palmroth, M., Laakso, H., Fejer, B. G., and Pfaff Jr., R. F. (2000). DE 2 observations of morningside and eveningside plasma density depletions in the equatorial ionosphere. *Journal of Geophysical Research: Space Physics*, 105(A8):18429–18442.

Park, J., Lühr, H., Knudsen, D. J., Burchill, J. K., and Kwak, Y.-S. (2017). Alfvén waves in the auroral region, their Poynting flux, and reflection coefficient as estimated from Swarm observations. *Journal of Geophysical Research: Space Physics*, 122(2):2345–2360.

Park, J., Luhr, H., and Min, K. (2011). Climatology of the inter-hemispheric field-aligned current system in the equatorial ionosphere as observed by CHAMP. *Annales Geophysicae*, 29(3):573–582.

Park, J., Lühr, H., Stolle, C., Rodríguez-Zuluaga, J., Knudsen, D. J., Burchill, J. K., and Kwak, Y.-S. (2016). Statistical survey of nighttime midlatitude magnetic fluctuations: Their source location and Poynting flux as derived from the Swarm constellation. *Journal of Geophysical Research: Space Physics*, 121(11):11,235–11,248.

Park, J., Lühr, H., Stolle, C., Rother, M., Min, K., and Michaelis, I. (2009). The characteristics of field-aligned currents associated with equatorial plasma bubbles as observed by the CHAMP satellite. *Ann. Geophys*, 27:2685–2697.

Park, J., Min, K. W., Kim, V. P., Kil, H., Su, S.-Y., Chao, C. K., and Lee, J.-J. (2008a). Equatorial plasma bubbles with enhanced ion and electron temperatures. *Journal of Geophysical Research: Space Physics*, 113(A9).

Park, J., Noja, M., Stolle, C., and Lühr, H. (2013). The ionospheric bubble index deduced from magnetic field and plasma observations onboard Swarm. *Earth, Planets and Space*, 65(11):13.

Park, J., Stolle, C., Lühr, H., Rother, M., Su, S.-Y., Min, K. W., and Lee, J.-J. (2008b). Magnetic signatures and conjugate features of low-latitude plasma blobs as observed by the champ satellite. *Journal of Geophysical Research: Space Physics*, 113(A9).

Patra, A. K., Srinivasulu, P., Chaitanya, P. P., Rao, M. D., and Jayaraman, A. (2014). First results on low-latitude E and F region irregularities obtained using the Gadanki Ionospheric Radar Interferometer. *Journal of Geophysical Research: Space Physics*, 119(12):10,276–10,293.

Perkins, F., Zabusky, N., and Doles III, J. (1973). Deformation and striation of plasma clouds in the ionosphere: 1. *Journal of Geophysical Research*, 78(4):697–709.

Pfaff, R. F. (2012). The near-Earth plasma environment. *Space science reviews*, 168(1-4):23–112.

Picone, J., Hedin, A., Drob, D. P., and Aikin, A. (2002). NRLMSISE-00 empirical model of the atmosphere: Statistical comparisons and scientific issues. *Journal of Geophysical Research: Space Physics*, 107(A12).

Pottelette, R., Malingre, M., Berthelier, J.-J., Seran, E., and Parrot, M. (2007). Filamentary Alfvénic structures excited at the edges of equatorial plasma bubbles. *Annales Geophysicae*, 25(10):2159–2165.

Rao, P. B., Patra, A. K., Chandrasekhar Sarma, T. V., Krishna Murthy, B. V., Subba Rao, K. S. V., and Hari, S. S. (1997). Radar observations of updrafting and downdrafting plasma depletions associated with the equatorial spread F. *Radio Science*, 32(3):1215–1227.

Rastogi, R. (1978). On the equatorial spread F. *Proceedings of the Indian Academy of Sciences-Section A, Earth and Planetary Sciences*, 87(7):115–131.

Reigber, C., Schwintzer, P., and Lühr, H. (1999). The CHAMP geopotential mission. *Boll. Geof. Teor. Appl*, 40:285–289.

Richmond, A. and Fang, T.-W. (2015). Electrodynamics of the equatorial evening ionosphere: 2. conductivity influences on convection, current, and electrodynamic energy flow. *Journal of Geophysical Research: Space Physics*, 120(3):2133–2147.

Richmond, A., Fang, T.-W., and Maute, A. (2015). Electrodynamics of the equatorial evening ionosphere: 1. importance of winds in different regions. *Journal of Geophysical Research: Space Physics*, 120(3):2118–2132.

Richmond, A. D. (1995). Ionospheric electrodynamics. In *Handbook of Atmospheric Electrodynamics*, pages 249–290. CRC Press.

Rishbeth, H. (1971). Polarization fields produced by winds in the equatorial F-region. *Planetary and Space Science*, 19(3):357–369.

Rishbeth, H. (2000). The equatorial F-layer: progress and puzzles. *Annales Geophysicae*, 18(7):730–739.

Rishbeth, H., Müller-Wodarg, I., Zou, L., Fuller-Rowell, T., Millward, G., Moffett, R., Idenden, D., and Aylward, A. (2000). Annual and semiannual variations in the ionospheric F2-layer: II. Physical discussion. *Annales Geophysicae*, 18(8):945–956.

Rodríguez-Zuluaga, J. and Stolle, C. (2019). Interhemispheric field-aligned currents at the edges of equatorial plasma depletions. *Scientific Reports*, 9(1):1233.

Rodríguez-Zuluaga, J., Stolle, C., and Park, J. (2017). On the direction of the Poynting flux associated with equatorial plasma depletions as derived from Swarm. *Geophysical Research Letters*, 44(12):5884–5891.

Rodríguez-Zuluaga, J., Stolle, C., Yamazaki, Y., Lühr, H., Park, J., Scherliess, L., and Chau, J. (2019). On the balance between plasma and magnetic pressure across equatorial plasma depletions. *Journal of Geophysical Research: Space Physics*.

Röttger, J. (1973). Wave-like structures of large-scale equatorial Spread-F irregularities. *Journal of Atmospheric and Terrestrial Physics*, 35(6):1195–1206.

Sabaka, T. J., Tyler, R. H., and Olsen, N. (2016). Extracting ocean-generated tidal magnetic signals from swarm data through satellite gradiometry. *Geophysical Research Letters*, 43(7):3237–3245.

Saito, S., Fukao, S., Yamamoto, M., Otsuka, Y., and Maruyama, T. (2008). Decay of 3-m-scale ionospheric irregularities associated with a plasma bubble observed with the Equatorial Atmosphere Radar. *Journal of Geophysical Research: Space Physics*, 113(A11).

Saynisch, J., Petereit, J., Irrgang, C., Kuvshinov, A., and Thomas, M. (2016). Impact of climate variability on the tidal oceanic magnetic signal - a model-based sensitivity study. *Journal of Geophysical Research: Oceans*, 121(8):5931–5941.

Scherliess, L. and Fejer, B. G. (1999). Radar and satellite global equatorial F region vertical drift model. *Journal of Geophysical Research: Space Physics*, 104(A4):6829–6842.

Schunk, R. and Nagy, A. (2009). *Ionospheres: physics, plasma physics, and chemistry*. Cambridge university press.

Singh, S., Johnson, F., and Heelis, R. (1999). Singular plasma disturbances in the low-latitude F region. *Journal of Geophysical Research: Space Physics*, 104(A3):4337–4350.

Stolle, C., Liu, H., Truhlík, V., Lühr, H., and Richards, P. (2011). Solar flux variation of the electron temperature morning overshoot in the equatorial F region. *Journal of Geophysical Research: Space Physics*, 116(A4).

Stolle, C., Lühr, H., and Fejer, B. G. (2008). Relation between the occurrence rate of ESF and the equatorial vertical plasma drift velocity at sunset derived from global observations. *Annales Geophysicae*, 26(12):3979–3988.

Stolle, C., Lühr, H., Rother, M., and Balasis, G. (2006). Magnetic signatures of equatorial spread F as observed by the CHAMP satellite. *Journal of Geophysical Research: Space Physics*, 111(A2).

Thébault, E., Finlay, C. C., Beggan, C. D., Alken, P., Aubert, J., Barrois, O., Bertrand, F., Bondar, T., Boness, A., Brocco, L., et al. (2015). International Geomagnetic Reference Field: the 12th generation. *Earth, Planets and Space*, 67(1):79.

Thébault, E., Vigneron, P., Langlais, B., and Hulot, G. (2016). A Swarm lithospheric magnetic field model to SH degree 80. *Earth, Planets and Space*, 68(1):126.

Tøffner-Clausen, L. (2018). Swarm level 1b product definition. Technical Report SW-RS-DSC-SY-0007, Issue 5.22, National Space Institute, Technical University of Denmark.

Tøffner-Clausen, L., Lesur, V., Olsen, N., and Finlay, C. C. (2016). In-flight scalar calibration and characterisation of the Swarm magnetometry package. *Earth, Planets and Space*, 68(1):129.

Tsunoda, R., Livingston, R., and Rino, C. (1981). Evidence of a velocity shear in bulk plasma motion associated with the post-sunset rise of the equatorial F-layer. *Geophysical Research Letters*, 8(7):807–810.

Vesecky, J., Chamberlain, J., Cornwall, J., Hammer, D., and Perkins, F. (1980). Irregularities in ionospheric plasma clouds: Their evolution and effect on radio communication. Technical report, SRI INTERNATIONAL ARLINGTON VA.

Wan, X., Xiong, C., Rodríguez-Zuluaga, J., Kervalishvili, G. N., Stolle, C., and Wang, H. (2018). Climatology of the occurrence rate and amplitudes of local time distinguished equatorial plasma depletions observed by Swarm satellite. *Journal of Geophysical Research: Space Physics*, 123(4):3014–3026.

Woodman, R. (1960). Irregular refraction of artificial satellite signals observed at Ancon, Peru. *Advances in Space Research*, Proceedings of the 1st Inter-American Symposium on Space Research, Buenos Aires, Argentina.

Woodman, R. (2009). Spread F–an old equatorial aeronomy problem finally resolved? *Annales Geophysicae*, 27(5):1915–1934.

Woodman, R. F. and La Hoz, C. (1976). Radar observations of F region equatorial irregularities. *Journal of Geophysical Research*, 81(31):5447–5466.

Xiong, C., Park, J., Lühr, H., Stolle, C., and Ma, S. Y. (2010). Comparing plasma bubble occurrence rates at CHAMP and GRACE altitudes during high and low solar activity. *Annales Geophysicae*, 28(9):1647–1658.

Xiong, C., Stolle, C., and Lühr, H. (2016a). The Swarm satellite loss of GPS signal and its relation to ionospheric plasma irregularities. *Space Weather*, 14(8):563–577.

Xiong, C., Stolle, C., Lühr, H., Park, J., Fejer, B. G., and Kervalishvili, G. N. (2016b). Scale analysis of equatorial plasma irregularities derived from Swarm constellation. *Earth, Planets and Space*, 68(1):121.

Xiong, C., Xu, J., Wu, K., and Yuan, W. (2018). Longitudinal thin structure of equatorial plasma depletions coincidently observed by Swarm constellation and all-sky imager. *Journal of Geophysical Research: Space Physics*, 123(2):1593–1602.

Yamazaki, Y. and Maute, A. (2017). Sq and EEJ—A review on the daily variation of the geomagnetic field caused by ionospheric dynamo currents. *Space Science Reviews*, 206(1-4):299–405.

Yamazaki, Y., Stolle, C., Matzka, J., and Alken, P. (2018). Quasi-6-day wave modulation of the Equatorial Electrojet. *Journal of Geophysical Research: Space Physics*, 123(5):4094–4109.

Yokoyama, T., Shinagawa, H., and Jin, H. (2014). Nonlinear growth, bifurcation, and pinching of equatorial plasma bubble simulated by three-dimensional high-resolution bubble model. *Journal of Geophysical Research: Space Physics*, 119(12):10–474.

Yokoyama, T. and Stolle, C. (2017). Low and midlatitude ionospheric plasma density irregularities and their effects on geomagnetic field. *Space Science Reviews*, 206(1-4):495–519.